Improved Continuous-Time Higher Harmonic Control Using $\mathcal{H}_\infty$ Methods

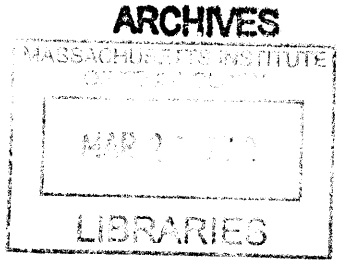

by

Frank H. Fan

B.S., University of California, San Diego (1996)
M.S., University of California, San Diego (2006)

Submitted to the Department of Aeronautics and Astronautics
in partial fulfillment of the requirements for the degree of
Doctor of Philosophy in Aeronautics and Astronautics
at the
MASSACHUSETTS INSTITUTE OF TECHNOLOGY
February 2013

Author .....
Department of Aeronautics and Astronautics
November 9, 2012

Certified by .....
Steven R. Hall
Professor of Aeronautics and Astronautics
Thesis Supervisor

Certified by .....
Emilio Frazzoli
Professor of Aeronautics and Astronautics

Certified by .....
Jonathan P. How
Professor of Aeronautics and Astronautics

Accepted by .....
Eytan H. Modiano
Professor of Aeronautics and Astronautics
Chair, Graduate Program Committee

Improved Continuous-Time Higher Harmonic Control Using $\mathcal{H}_\infty$ Methods

by

Frank H. Fan

Submitted to the Department of Aeronautics and Astronautics
on November 9, 2012, in partial fulfillment of the
requirements for the degree of
Doctor of Philosophy in Aeronautics and Astronautics

Abstract

The helicopter is a versatile aircraft that can take-off and land vertically, hover efficiently, and maneuver in confined space. This versatility is enabled by the main rotor, which also causes undesired harmonic vibration during operation. This unwanted vibration has a negative impact on the practicality of the helicopter and also increases its operational cost.

Passive control techniques have been applied to helicopter vibration suppression, but these methods are generally heavy and are not robust to changes in operating conditions. Feedback control offers the advantages of robustness and potentially higher performance over passive control techniques, and amongst the various feedback schemes, Shaw's higher harmonic control algorithm has been shown to be an effective method for attenuating harmonic disturbance in helicopters. In this thesis, the higher harmonic disturbance algorithm is further developed to achieve improved performance.

One goal in this thesis is to determine the importance of periodicity in the helicopter rotor dynamics for control synthesis. Based on the analysis of wind tunnel data and simulation results, we conclude the helicopter rotor can be modeled reasonably well as linear and time-invariant for control design purposes. Modeling the helicopter rotor as linear time-invariant allows us to apply linear control theory concepts to the higher harmonic control problem. Another goal in this thesis is to find the limits of performance in harmonic disturbance rejection. To achieve this goal, we first define the metrics to measure the performance of the controller in terms of response speed and robustness to changes in the plant dynamics. The performance metrics are incorporated into an $\mathcal{H}_\infty$ control problem. For a given plant, the resulting $\mathcal{H}_\infty$ controller achieves the maximum performance, thus allowing us to identify the performance limitation in harmonic disturbance rejection. However, the $\mathcal{H}_\infty$ controllers are of high order, and may have unstable poles, leading us to develop a design method to generate stable, fixed-order, and high performance controllers. Both the $\mathcal{H}_\infty$ and the fixed-order controllers are designed for constant flight conditions. A gain-scheduled control law is used to reduce the vibration throughout the flight envelope. The gain-scheduling is accomplished by blending the outputs from fixed-order controllers designed for different flight conditions. The structure of the fixed-order controller allows the usage of a previously developed anti-windup scheme, and the blending function results

in a bumpless full flight envelope control law.

Thesis Supervisor: Steven R. Hall
Title: Professor of Aeronautics and Astronautics

Acknowledgments

This research was funded by the Office of Naval Research, grant number N00014-09-1-0902, with Dr. Judah Milgram serving as the technical monitor. The views expressed in this thesis are not necessarily the official views of, or endorsed by, the Office of Naval Research. The Boeing Company provided the CAMRAD simulations essential to this thesis. In particular, Dr. Friedrich Straub worked tirelessly and patiently to ensure we obtained the right results. During my stay at MIT, I also received financial support from the Gelb Fellowship.

I am grateful to have Prof. Steven R. Hall as my advisor, the guidance and mentoring he provided over the course of my study at MIT was invaluable. I am also grateful to have Prof. Emilio Frazzoli and Prof. Jonathan How on my thesis committee. Additionally, I thank Prof. How for the opportunity to be a TA for 16.31. I would also like to thank my thesis readers, Dr. Friedrich Straub and Prof. Norman Wereley, for their insightful feedback, and to Kathryn Fischer and Quentin Alexander for all the help they provided.

To my friends at MIT, Jim McGrew, Brett Bethke, Frant Sobolic, Karl Kulling, Dan Levine, Buddy Michini, Sameera Ponda, Andy Whitten, Josh Redding, Cam Fraser, Spencer Ahrens, Luca Bertuccelli, Vishnu Desaraju, Travis Wolf, Fabio Fachin, Aditya Undurti, Tuna Toksoz, and Ian Sugel, I learned much from all of you, and thank you for shaping the fond memories I will take away with me. To Frank and Grace Brockmeyer, Eric and Michelle Dauler, Tim and Shirley De Chant, Brianne Howe, Kate Hudec and Brian Nelson, the friends I would never have met had I not gone back to school, thank you for your friendship and the diversions from an otherwise all-consuming endeavor.

Finally, I thank my brothers Andy and Paul, and sister-in-law Annette for their unwavering support. I thank my dad for his patience and words of encouragement. Most importantly, I want to express my utmost gratitude to my wife Myra, whose devotion and kindness made everything I've done possible.

This thesis is dedicated to the memory of my mom.

Contents

List of Figures

List of Tables

Chapter 1

Introduction

Most helicopters experience significant levels of vibration during flight. Excessive vibration is problematic since it leads to passenger discomfort, reduced crew effectiveness, and increased maintenance costs due to fatigue of structural and nonstructural components. As a result, vibration reduction is an important area of helicopter research.

Helicopter researchers and engineers have developed a control framework called higher harmonic control (HHC) to address the problem of excessive vibration. The framework consists of actuators that can produce the necessary changes in lift in each rotor blade, sensors to measure the vibration, and a controller that implements the HHC algorithm to compute the required actions of the actuators, based on the measurement, to cancel the vibration. HHC has been shown to be effective in wind tunnel tests [48, 87] as well as actual flight tests [105]. The goal of this thesis is to develop a methodology for designing higher harmonic controllers with improved performance over current design methods.

In this chapter, we first formulate the helicopter vibration control problem, and describe the approach we take in this thesis to solve the problem. Then we present a literature review that covers the historical development of vibration reduction in the helicopter up the current state, as well as other literature that are relevant in solving the helicopter vibration reduction problem. A summary of important conclusions and an outline of the thesis are provided to conclude the chapter.

1.1 Helicopter Vibration Problem

The main cause of the vibration in a helicopter is the periodic variation in the aerodynamic loads as the rotor blades move around the rotor azimuth. Since the rotor spins at a near constant speed, the resulting vibration occur at multiples of the blade passage frequency. For a helicopter rotor with N blades, and a rotor angular speed of Ω, the blade passage frequency is $N\Omega$. In addition, imbalance and manufacturing variations in the individual rotor blades cause vibration with frequency equal to Ω. The frequency of vibration is often normalized by the rotor angular speed Ω, thus the fundamental harmonic is at 1 per rev, and the blade passage frequency at N per rev is the Nth harmonic. To effectively reduce vibration levels in a helicopter, the harmonic vibrations from the rotor must be attenuated.

The objective of this thesis is to address the helicopter vibration reduction problem from the perspective of control theory. To achieve this objective, we will first analyze existing wind tunnel test data of a full scale rotor to quantify the importance of periodic dynamics in the helicopter rotor. Then the appropriate control design plant models will be obtained by applying system identification techniques to the wind tunnel test data and nonlinear simulation data. The plant models, which are at different constant flight conditions, will be used in the development of the control design methods for helicopter vibration reduction. We will examine the limits of performance, in terms of appropriately defined metrics, that can be achieved. We will also take into consideration the practical aspects of a controller in the development of the control methods. Finally, we will extend the controller to work in varying flight conditions, since the helicopter operates within a flight envelope instead of a constant flight condition.

1.1.1 Research Approach

Our approach to reduce the vibration is to use feedback control. The vibration reduction problem is formulated as an output disturbance rejection problem, which is shown as a block diagram in Figure 1-1. In the block diagram, the harmonic vibration generated by the main rotor is represented by the disturbance d, thus the frequency content of d is known, but its amplitude and phase are unknown. The plant block in Figure 1-1 represents the he-

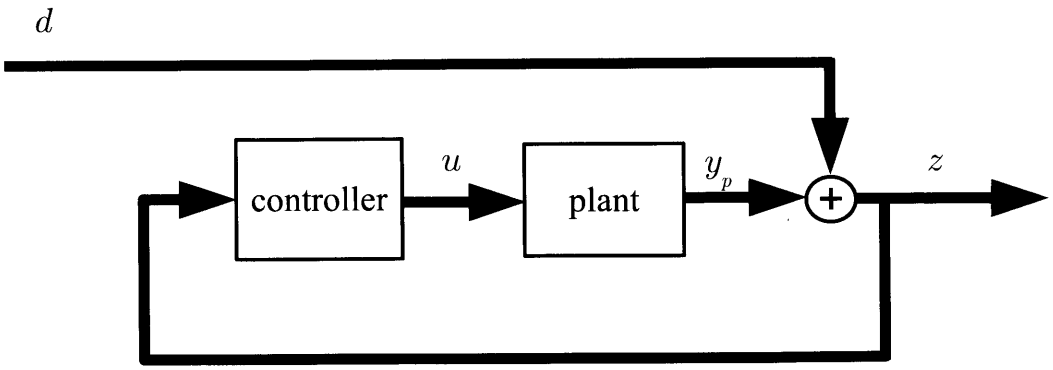

Figure 1-1: Block diagram of the feedback control system for harmonic disturbance rejection

licopter rotor, the periodic dynamics that produces the harmonic vibrations are excluded, since they are considered as the output disturbance. Note that treating the harmonic vibrations as an output disturbance does not imply that the plant dynamics is no longer periodic. The controller is the focus of our research, and our main goal is to develop a methodology to design effective feedback controllers for harmonic disturbance rejection in the measured output z.

In order to determine the dynamics relevant for the design of effective controllers, we will examine the behavior of the helicopter rotor using frequency domain techniques developed for linear time-periodic systems. Specifically, we will determine the extent of periodicity in the helicopter rotor at different values of advance ratio μ, since it is known that the dynamics of the rotor is dependent on μ [56]. The advance ratio μ is the dimensionless forward speed of the helicopter rotor, given by

$$\mu = \frac{V \cos \alpha}{\Omega R} \tag{1.1}$$

where V is the helicopter velocity, α is the rotor shaft angle (rotor disk plane angle of attack), Ω is the rotor angular speed, and R is the radius of the rotor. In addition, the wind tunnel test data allows us to quantify the harmonic disturbance, which is useful information in the controller design process.

The plant models to be used for control design will have structures dictated by the dynamics of the helicopter rotor. Optimization based system identification methods, with

appropriate cost function and weighting, will be used to extract parametric models from wind tunnel test data. Since we only have limited wind tunnel test data, we will also apply our system identification method to simulation data to obtain additional models at different flight conditions. The simulation data span most of the flight envelope in terms of the rotor shaft angle α, the advance ratio μ, and the blade loading coefficient C_T/σ. The blade loading coefficient is defined as the ratio between the thrust coefficient C_T and the rotor solidity σ. The variations in plant dynamics at different flight conditions will enable us to determine the important flight parameters that we must account for in designing the full flight envelope harmonic disturbance rejection control law.

We will define metrics that capture the performance and robustness of the harmonic disturbance rejection controller, and then explore design methods that will produce controllers with maximum performance. Since performance and robustness are generally conflicting objectives, a Pareto frontier may be generated to indicate the limit of achievable performance. If the maximum performing controller is not practical for implementation purpose, *i.e.*, the controller is unstable or of high order, then we will develop a method to design practical controllers that achieve improved performance compared to the currently available methods. Finally, based on the variation of the plant dynamics at different flight conditions, we will develop a control law that can be used in the entire flight envelope to reduce vibration.

1.2 Literature Review

The primary source of literature is from the helicopter research community, where the harmonic vibration reduction problem has been extensively studied. Since our approach is to use feedback control, we also examined controls literature, in particular, we are interested in using a stable and robust controller to achieve our goal. The helicopter vibration reduction problem is fundamentally similar to the narrowband disturbance rejection problem in control theory, so we also present some relevant literature from different application fields to illustrate the similarity.

1.2.1 Helicopter Vibration Reduction

Helicopter vibration reduction methods can be generalized into one of two groups, active control or passive control [4, 70]. Passive vibration control techniques include pendulum absorbers [49], anti-resonance devices [13], and modification to the rotor transmission/fuselage mounting system [80, 70]. Although they can be effective, passive vibration control methods may be mechanically complicated, especially in cases where multiple forces and moments at different harmonics require attenuation. Passive vibration controllers may also be heavy, reducing the available payload of the helicopter, and cannot remain in tune for all flight conditions [80].

Active control has the potential to significantly reduce higher harmonic vibrations with less weight than passive methods. Friedmann [34] identified four approaches to active vibration control in helicopters, including higher harmonic control, individual blade control (IBC), vibration reduction using an actively controlled trailing-edge flap located on the blade, and active control of structural response (ACSR). The four approaches are distinguished by the mode of actuation. From a control theoretic perspective, however, all four approaches are similar in that the controller all implement the HHC algorithm [77].

The idea behind ACSR is to minimize the vibration at the desired locations in the fuselage using the principle of superposition. Actuators are mounted to the fuselage to counteract the vibration generated by the main rotor. Performance analysis of ACSR using a coupled rotor and flexible fuselage model was carried out by Cribbs, Friedmann, and Chiu [19], which showed ACSR has low power demand. Since no modification to the rotor is required, ACSR also may have potentially fewer airworthiness issues than HHC [94, 78].

Individual blade control (IBC) refers to the actuation of each rotor blade independently with a broadband actuator [46]. As such, IBC may refer to individually actuated pitch-links, trailing-edge flaps, active blade twist, or other types of actuation with the actuators in the rotating frame [104, 72, 54, 79, 82, 83, 59]. In addition to the application for vibration reduction, IBC with HHC algorithm may also be used to reduce noise [15, 93] and improve the overall performance of a helicopter [63, 47, 68]. In a higher harmonic control survey paper, Kessler [60] defined HHC to refer to the control actuation where the actuators are

in the fixed frame. However, Shaw [85] intended for HHC to imply the control theoretic idea for harmonic disturbance rejection, with control actuation either in the fixed frame or the rotating frame. In this thesis, we refer to the active helicopter vibration control algorithms collectively as the higher harmonic control algorithm, without regard to the type of actuation employed.

As originally conceived by McHugh and Shaw [73], Shaw [85], and Shaw and Albion [86], HHC is a discrete-time algorithm based on a linear quasisteady model of the helicopter rotor (the so called $\mathbf{T}$ matrix), and the actuation is achieved through the swashplate, actuators on the pitch links, or on-blade actuation such as actively controlled trailing-edge flaps on the rotor blades. The linear quasisteady rotor model can be obtained either *a priori* based on a combination of testing and modeling, or identified in real-time onboard the helicopter. Using the $\mathbf{T}$ matrix obtained from real-time online identification in the control loop is referred to as the adaptive HHC. The main reason to use adaptive HHC is to account for uncertainties in the plant dynamics [57], although it has also been applied successfully to address the variations in the plant dynamics at different flight conditions [48, 74]. Patt *et al.* [77] summarized the development of various discrete-time HHC algorithms, including a relaxed version of HHC, and provided convergence and robustness analysis of both the HHC algorithm and the relaxed HHC algorithm. An advantage of the quasisteady discrete-time approach is that the $\mathbf{T}$ matrix can faithfully model the (quasisteady) effects of periodicity on the dynamic response of the rotor. On the other hand, the quasisteady assumption and discrete-time nature of the controller make it difficult to apply results from control theory to the problem.

Gupta, Du Val and Gregory [40, 41, 28] applied the linear quadratic (LQ) optimal control method [67, 2] to the helicopter vibration problem. In their approach, the dynamics are modeled using a linear time-invariant (LTI) state-space model of the helicopter. The standard linear quadratic regulator (LQR) approach is extended to include frequency domain weighting filters in the quadratic cost functional. In particular, the filters were selected to place infinite weighting at the selected harmonic frequencies, resulting in controllers that completely reject the disturbance at the selected harmonic frequencies. Bittanti and Moiraghi also modeled the helicopter dynamics as LTI, and applied the pole assignment

technique to design controllers for harmonic disturbance rejection [9]. Bittanti, Lorito and Strada [7, 8] considered observer based controllers for helicopter vibration reduction. They replaced the output harmonic disturbance by an equivalent input disturbance, and then designed controllers using the linear quadratic Gaussian (LQG) approach.

Hall and Wereley [44] developed a framework based on classical control theory to analyze Shaw's HHC algorithm. They showed that Shaw's discrete-time HHC algorithm is similar to a continuous-time controller that employs an oscillator at the disturbance frequency in the feedback. (This result is really just the an instance of the internal model principle [31].) Further, they showed that the continuous-time controller generally results in greater stability margins and better performance than the discrete-time HHC algorithm.

One potential limitation of the continuous-time higher harmonic control (CTHHC) approach is that it relies on an LTI model of the helicopter dynamics. Theoretically, both the disturbance and the dynamics of a helicopter rotor in forward flight should be periodic. For small control inputs, linearizing the dynamics leads naturally to a linear time-periodic (LTP) model [56]. Wereley and Hall [102] developed the harmonic transfer function (HTF) approach to describe LTP systems in the frequency domain, and showed how classical control analysis tools for LTI systems, such as the Nyquist diagram, can be extended to LTP systems. The HTF was used by Arcara, Bittanti and Lovera [3] to construct an input equivalent disturbance, which allows the vibration control problem for LTP systems to be formulated in a periodic optimal control framework [6]. Numerical simulations show, however, that the optimal periodic control law does not achieve satisfactory performance if the flight condition varies, which led Bittanti and Cuzzola [5] to develop a gain-scheduled $\mathcal{H}_\infty$ approach for the parameter varying LTP system. It was found that for the values of advance ratio ranging from 0 to 0.3, a total of 60 controllers were required for gain-scheduling to achieve good performance.

However, experimental data suggests that the effects of periodicity on helicopter rotor dynamics (but not the disturbance) are often insignificant, and that the dynamics of rotors often may be treated as time-invariant, at least for a fixed flight condition. For example, wind tunnel experiments conducted by Shin, Cesnik, and Hall [88] on the four-bladed NASA/Army/MIT Active Twist Rotor showed that the periodic parts of the harmonic trans-

fer function for that rotor are much smaller than the time-invariant part of the transfer function, implying that the helicopter rotor in forward flight may be well modeled as an LTI system.

The effectiveness of the LTI model based CTHHC approach was demonstrated by Hall *et al.* [42] on the Smart Material Active Rotor Technology (SMART) rotor in 2008. The SMART rotor is a full-scale, five-bladed rotor based on the MD-900 helicopter rotor. Traditionally, HHC algorithms control vibration at multiples of the N per rev harmonic only, where N is the number of rotor blades. However, wind tunnel data for the SMART rotor showed that significant vibration exists at most integral harmonics of the rotor frequency within the frequency range from 0 per rev to 12 per rev. Using CTHHC controllers, Hall *et al.* were able to achieve a 95% decrease in the normal force vibratory load simultaneously for the first five harmonics.

1.2.2 Helicopter Rotor Model for Control Design

Helicopter rotor model can be obtained using the theory of aeroelasticity [33], detailed description of the interactions between the elastic and aerodynamic forces in the rotor given by Johnson [56] and Stepniewski and Keys [96] are useful for the design and analysis of the helicopter. For control design purpose, a simpler model is preferred since the controllers obtained using modern control techniques have the same order as the plant model. Model reduction procedures such as balanced truncation and Hankel norm approximation can be used to obtain plant models that capture enough details while keeping the order of the model tractable in control synthesis [38, 39]. The reduction procedure can also be applied to the controller, thus allowing the full order model to be used in the design process.

An alternative approach is to use system identification techniques to infer the model from experimental data. Models obtained using system identification techniques are often used for control design purpose [37], and can be specialized for robust control design as in [81]. Linear time-invariant models obtained using system identification techniques range from the empirical transfer function, which can be used in classical frequency domain control design method, to parametric models that are suitable for modern state-space

control design method [69]. Procedures for identifying linear time-periodic systems were developed by Siddiqi [89] and Allen [1]. The procedure developed by Allen identifies the time-varying state transition matrix of an LTP system. Siddiqi developed an experimental method to obtain the harmonic transfer function, which was introduced by Wereley and Hall [102] to represent an LTP system in frequency domain.

1.2.3 Performance limitations

The knowledge of performance limitation for a given plant and control architecture allows the determination of whether the performance specification is feasible before the control synthesis step is carried out. In the case that the performance specification is not feasible, a change in control architecture, *i.e.*, the types and locations of sensors and actuators, may be required. The seminal work on limits of performance in control system was done by Bode [12]. For minimum phase systems, Bode established the relationship between the system gain and phase, as well as the sensitivity integral bearing his name. Further extension of Bode's sensitivity integral to cover unstable and nonminimum phase systems were established by Horowitz [52] and Freudenberg and Looze [32].

1.2.4 Stable Stabilization

Modern control techniques such as $\mathcal{H}_2$ and $\mathcal{H}_\infty$ do not explicitly incorporate the pole locations of the controller in problem formulation, so the resulting controllers may have poles in the open right-half plane. In contrast, by using the internal model principle to achieve harmonic disturbance rejection, the continuous-time HHC has all the poles on the $j\omega$-axis, hence is marginally stable. The term stable stabilization (also called strong stabilization) refers to finding stable controllers that achieves internal stability for a given plant [24]. For a single-input/single-output plant, the necessary and sufficient condition for the existence of a stable controller is known as the parity interlacing property (PIP), which requires an even number of real poles between every pair of real zeros in the right-half plane [107].

Construction of the stable controller has been examined by numerous authors, and can in general be grouped into two main categories, the interpolation approach [99, 36], and the

modified algebraic Riccati equation (ARE) approach [55, 110, 111]. The interpolation approach of stable controller construction by Vidyasagar [99] is based on the parametrization of all controllers by Youla, Bongiorno, and Jabr [106, 108], and consists of finding a unit in the set of all proper stable rational functions that satisfies the interpolation constraints imposed by the plant. For plants with the parity interlacing property, this method will yield a stable controller, but the order of the controller could be arbitrarily high [92, 110]. Ito, Ohmori, and Sano [53] extended the interpolation approach to incorporate $\mathcal{H}_\infty$ performance specifications in the problem formulation.

The modified ARE approach is based on a state-space framework similar to that of $\mathcal{H}_2$ and $\mathcal{H}_\infty$ control. The general approach is to fix the controller structure, and then appropriately modify the ARE to ensure stability of the controller [100, 110]. The order of the controller is fixed, and it may be possible to find reduced order stable controller directly [101]. $\mathcal{H}_2$ and $\mathcal{H}_\infty$ performance specifications can be treated in this framework, but the resulting algebraic Riccati equations are coupled and the solution of the coupled AREs is a nontrivial task. Furthermore, since the modified AREs are only necessary conditions for a stable controller, further modifications to the AREs may be required to obtain nonconservative controller.

The stable stabilization problem is closely related to the problem of simultaneous stabilization [99, 11], which is the problem of designing a controller that will stabilize a set of distinct plants. Treating the elements from the set of distinct plants as variations from the nominal plant, it can be seen that the concept of simultaneous stabilization is similar to the robust control problem.

1.2.5 Robust Control

The robust control problem is to design a controller that achieves internal stability and the performance specification for all admissible uncertainties. The model uncertainties are treated as perturbations about the nominal plant, which could be due to the lack of knowledge about the true plant, or the need for a simplified nominal model for control design. The development of the robust control theory was motivated by the lack of guaranteed

stability margins in LQG controlled systems [21].

Three useful tools in robust control are the linear factional transformation (LFT), the structured singular value μ [26], and $\mathcal{H}_\infty$ optimization. LFT provides the general framework for robust control theory, in block diagram form, it has the interpretation of isolating the perturbation from the generalized plant in a feedback loop [23]. The main utility of LFT is that it allows a variety of control problems, including both robust stability and robust performance, to be treated using the same mathematical machinery.

The structured singular value μ introduced by Doyle *et al.* [22], and the closely related multivariable stability margin k_m introduced by Safonov [84] are powerful tools for control system robustness analysis. The structured singular value μ extends the idea of the maximum singular value for systems that contain a combination of unknown parameters and unmodeled dynamics [29]. While problems with unstructured uncertainty can be handled by the small gain theorem, μ is needed to deal with problems with structured uncertainties. However, in the general case of mixed real and complex uncertainties, μ cannot be computed exactly, and numerical methods must be used to obtain estimates of mixed μ.

The $\mathcal{H}_\infty$ optimization is used to obtain a controller that minimizes the ratio of the 2-norm between the input signals and output signals of the generalized plant. The use of weighting filters to specify required performance is an important aspect of $\mathcal{H}_\infty$ control design. The appropriate use of the weighting filters on system transfer functions allows specification of the nominal performance [91, 112]. The sub-optimal $\mathcal{H}_\infty$ controller can be obtained by solving a pair of algebraic Riccati equation as shown by Doyle *et al.* [25], and a bisection search can be used to find a near optimal $\mathcal{H}_\infty$ controller [66]. Alternatively, linear matrix inequality (LMI) can be used to obtain the $\mathcal{H}_\infty$ controller [35].

1.2.6 Active Noise Control and Narrowband Disturbance Rejection

The field of active noise control (ANC) is concerned with mitigating noise generated by a primary source in a given environment. A typical ANC setup consists of the generation of an antinoise signal that is propagated from a secondary source, which then cancels the undesired noise through the principle of superposition. The antinoise signal, which ideally

has the same magnitude but the opposite phase as the noise, is generated by a filter that is analogous to the controller in a control system, while the secondary source can be viewed as the actuator in a control system. Although ANC methods are primarily focused on acoustic noise, they have also been used in the suppression of vibration [30] and hydroacoustic noise [65].

In general, ANC can be categorized into feedforward control structure [71] and feedback control structure [76]. In the feedforward ANC setup, a reference sensor measures the primary noise to be suppressed, which is then processed by an adaptive filter to generate the antinoise; the adaptive filter is updated using signal measured from an error sensor. The main difference in the feedback control structure is that instead of using two sensors, only one sensor is used to measure the noise. The measured noise is then processed by the filter before it is passed on to the secondary source, creating the feedback loop [98]. Despite being categorized as feedforward control structure, in most instances the reference sensor will be sensitive to the antinoise generated by the secondary source, creating a feedback path that must be accounted for in the ANC design process [98]. Adaptive algorithms used in ANC include filtered-X least-mean-squares (FXLMS) [17, 103], and recursive least squares (RLS) [51, 109]. The ANC problem resembles the HHC problem in many respects, in particular, the idea of the antinoise signal is fundamentally similar to the control signal generated by the HHC algorithm. In certain applications, such as cooling fan noise reduction [61], the acoustic noise spectrum is narrowband, the ANC problem is nearly identical to the HHC problem.

Literature for control schemes to attenuate narrowband or harmonic disturbances also exist in other application fields. In the control of tape drives and optical drives, the literature refers to the scheme of periodic disturbance rejection as repetitive control [50, 95, 64]. The term convergent control [62] is used to describe an algorithm to control a rotor on magnetic bearings. Sievers and von Flotow [90] categorized a variety of control methods for the general problem of narrowband disturbance rejection.

1.3 Thesis Outline

The remainder of this thesis is organized as follows:

In Chapter 2, a review of different control algorithms for helicopter harmonic vibration reduction is given. These algorithms are based on models with varying degrees of simplifications, and range from Shaw's original discrete-time HHC to optimal control for linear time-periodic systems.

In Chapter 3, we define the performance measures for harmonic disturbance rejection, namely the bandwidth and the peak sensitivity. The performance metrics are incorporated in a notch filter, which is used as the weighting filter in the full-order $\mathcal{H}_\infty$ control method. The performance limit in harmonic disturbance rejection, in terms of the bandwidth and peak sensitivity, is obtained by using full-order $\mathcal{H}_\infty$ controller designed with high order notch filter.

The full-ordered $\mathcal{H}_\infty$ controller that is developed in Chapter 3 presents two problems. First, the controller is of high order since the notch filter of high order is required. The second problem is that the full-ordered $\mathcal{H}_\infty$ controller is not guaranteed to be stable. We develop a fixed-order $\mathcal{H}_\infty$ control methodology that produces marginally stable controller with reduced order in Chapter 4.

Linear time-invariant models are used for control design in both Chapters 3 and 4. In Chapter 5, we present the analysis of existing wind tunnel test data showing the effects of periodicity to be small, which allows us to use the LTI model for control design. We also discuss the process used to obtain the plant models from both previously collected wind tunnel test data and nonlinear simulation data.

Since significant changes occur to the dynamics of the helicopter with changes in the flight condition, we design a gain-scheduled controller to maintain disturbance rejection performance throughout the flight envelope. In Chapter 6, we provide the details of the gain-scheduled control law and present the results from closed-loop simulations.

In Chapter 7, we provide a summary of this thesis, including the main contributions, and discuss potential areas for future research.

Chapter 2

Helicopter Vibration Control

Various types of plant models have been used in the helicopter vibration reduction problem. The underlying assumptions in the plant models lead to different controller design methods. In this chapter, we examine three types of linear models, namely the quasisteady model, the linear time-invariant (LTI) model, and the linear time-periodic (LTP) model, and the control algorithms that have been developed for these three types of models. A common theme in the different control algorithms is in the inclusion of the dynamics of a harmonic oscillator, either indirectly through weighting filters in the performance index, or directly through the structure of the controller.

2.1 Linear Quasisteady Plant

The discrete-time quasisteady model of the helicopter rotor is

$$\mathbf{z}_n = \mathbf{T}\mathbf{u}_n + \mathbf{z}_0 \tag{2.1}$$

where the vectors

$$\mathbf{u}_n = \begin{bmatrix} u_{c_n} \\ u_{s_n} \end{bmatrix} \tag{2.2}$$

and

$$\mathbf{z}_n = \begin{bmatrix} z_{c_n} \\ z_{s_n} \end{bmatrix} \tag{2.3}$$

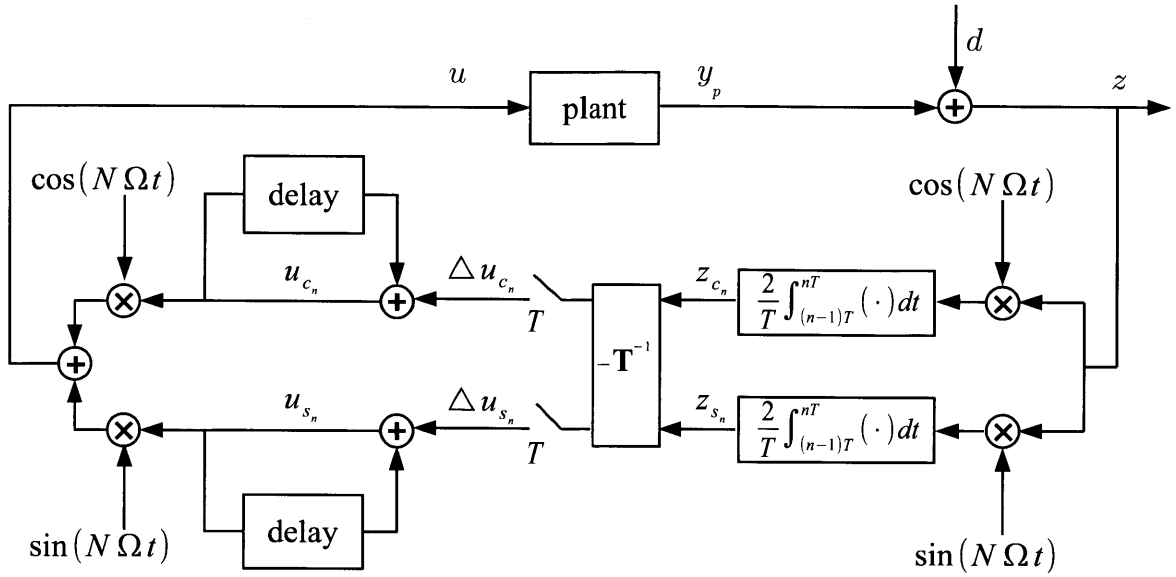

Figure 2-1: Block diagram for implementing Shaw's discrete-time HHC algorithm

are the amplitudes of the harmonic components of the plant input and output, respectively, and the subscript n indexes the discrete time steps. The constant matrix $\mathbf{T}$ in Equation (2.1) is the control response matrix, and $\mathbf{z}_0$ is a vector of the amplitudes of the harmonic components of the baseline vibration that is to be rejected [57].

2.1.1 Discrete-Time Higher Harmonic Control

The baseline harmonic vibration $\mathbf{z}_0$ in Equation (2.1) can be eliminated by applying the control

$$\mathbf{u}_n = -\mathbf{T}^{-1}\mathbf{z}_0 \tag{2.4}$$

However, since $\mathbf{z}_0$ is unknown, an alternative is to cancel the current vibration level $\mathbf{z}_n$ by applying the discrete-time control

$$\mathbf{u}_{n+1} = \mathbf{u}_n - \mathbf{T}^{-1}\mathbf{z}_n \tag{2.5}$$

Equation (2.5) is Shaw's higher harmonic control (HHC) algorithm [85], and its implementation is shown in Figure 2-1. The components of the harmonic amplitude vector $\mathbf{z}_n$ are the Fourier coefficients of the measured vibration at the frequency $N\Omega$. The Fourier co-

efficients are obtained by integrating the demodulated vibration signal over one sampling period T, which must be an integral number of blade passage periods. The amount of control adjustments Δu_c and Δu_s are obtained as the product of $\mathbf{z}_n$ and the inverse of the control response matrix $\mathbf{T}^{-1}$. The control adjustments are sampled and added to the control signal amplitudes of the previous time step, generating the current control amplitude vector $\mathbf{u}_n$. The controller output is obtained by summing the modulated components of the control amplitude vector.

The integrations of the demodulated signals in Figure 2-1 extracts the harmonic information from the measured output. As a result, Shaw's HHC algorithm accounts for the inherent periodicity of the helicopter rotor disturbance, even though the plant used for control design is quasisteady.

In the case that the plant is not exactly quasisteady, the one period integration smooths out the effect of the plant dynamics in the measured vibration signal. Since a longer integration period generally leads to an increased level of smoothing, it also diminishes the effects of the system dynamics. Thus, in the case where the rotor dynamics is important and cannot be ignored, the HHC algorithm would require a longer sampling period, which in turn leads to a controller with a long settling time that is slow to respond to changes in the disturbance. On the other hand, speeding up the response by decreasing the sampling period introduces the plant dynamics into the controller, which could destabilize the closed-loop system, since the quasisteady assumption no longer holds.

A generalization of Shaw's algorithm [16, 57] can be obtained by considering a quadratic cost function of the form

$$J(\mathbf{z}_n, \mathbf{u}_n) = \mathbf{z}_n^T \mathbf{W}_\mathbf{z} \mathbf{z}_n + \mathbf{u}_n^T \mathbf{W}_\mathbf{u} \mathbf{u}_n \tag{2.6}$$

which results in the control law

$$\mathbf{u}_{n+1} = \left(\mathbf{T}^\mathbf{T} \mathbf{W}_\mathbf{z} \mathbf{T} + \mathbf{W}_\mathbf{u}\right)^{-1} \mathbf{T}^T \mathbf{W}_\mathbf{z} \left(\mathbf{T}\mathbf{u}_n - \mathbf{z}_n\right) \tag{2.7}$$

It can be seen that without the control weighting $\mathbf{W}_\mathbf{u}$, Equation (2.7) simplifies to Equation (2.5).

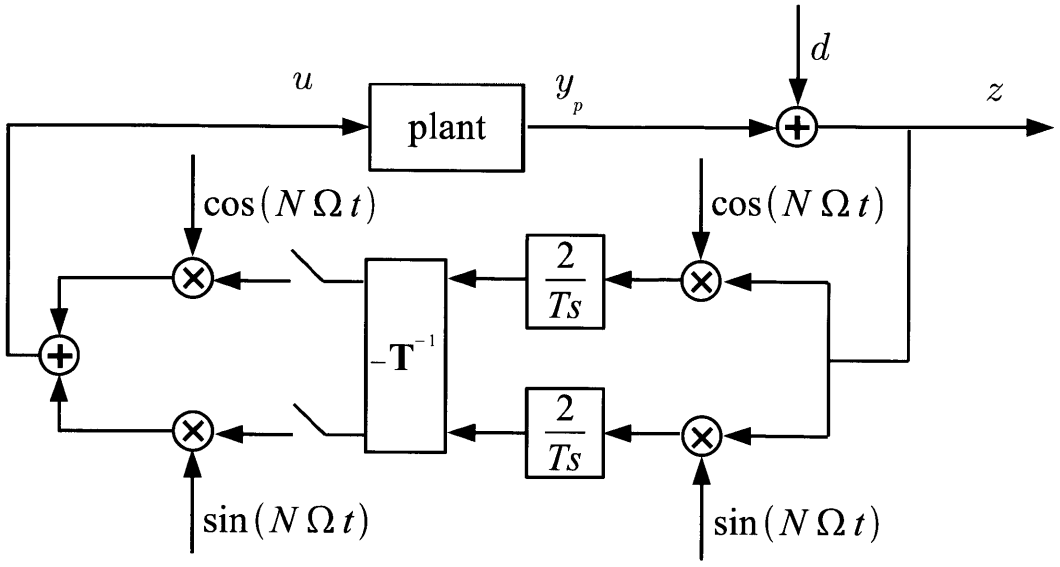

Figure 2-2: Alternative implementation of Shaw's HHC algorithm with integrators and sample and hold

2.1.2 Continuous-Time Higher Harmonic Control

Hall and Wereley [44, 45] noted that the integration over one period, the summation and the delay shown in Figure 2-1 can be replaced by a continuous integration and a sample and hold as shown in Figure 2-2. Furthermore, using the continuous signals instead of sample and hold results in the continuous-time implementation of the HHC shown in Figure 2-3.

Observing that $\mathbf{T}$ matrices of helicopter rotors are often nearly skew-symmetric [45], then the inverse control response matrix can be assumed to have the form

$$\mathbf{T}^{-1} = \begin{bmatrix} a & b \\ -b & a \end{bmatrix} \tag{2.8}$$

The transfer function of the continuous-time higher harmonic controller depicted in Figure 2-3 is given by

$$K(s) = \frac{-U(s)}{Z(s)} = 2k\frac{as + bN\Omega}{s^2 + (N\Omega)^2} \tag{2.9}$$

where $U(s)$ is the Laplace transform of $u(t)$, and $Z(s)$ is the Laplace transform of $z(t)$. The static gain k is a design parameter chosen to satisfy the stability margins and the band-

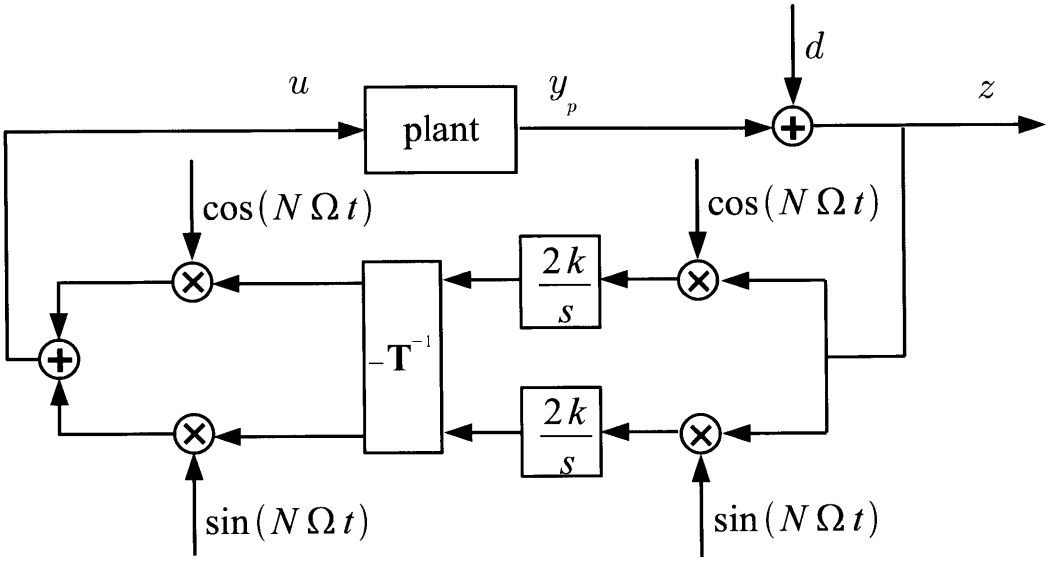

Figure 2-3: Implementation of the continuous-time HHC algorithm

width of the controller. For direct comparisons between the discrete-time algorithm and the continuous-time algorithm, the gain should be selected as

$$k = \frac{1}{T} \tag{2.10}$$

With a complex conjugate pair of poles at $s = \pm jN\Omega$, the controller $K(s)$ in Equation (2.9) is in the form of the classical controller for rejecting a sinusoidal disturbance with a frequency equal to $N\Omega$. The closed-loop pole positions can be shown to be at

$$s \approx -\frac{1}{T} \pm jN\Omega \tag{2.11}$$

where T is approximately the settling time of the closed-loop system. As in the discrete-time case, a smaller T corresponds to a faster response to changes in the harmonic disturbance, but the dynamics of the system may be destabilized.

The continuous-time HHC offers an interpretation for the relaxed version of the discrete-time HHC algorithm described by Patt *et al.* [77]. The relaxed HHC algorithm was attributed to Depailler [20], and is obtained by applying a relaxation factor $\alpha < 1$ to the

control update in Equation 2.5, resulting in

$$\mathbf{u}_{n+1} = \mathbf{u}_n - \alpha \mathbf{T}^{-1} \mathbf{z}_n \tag{2.12}$$

Simulation results [77] showed that the relaxed version increases the convergence time, but is useful in situations where the estimated $\mathbf{T}$ is uncertain, which could occur in maneuvering flight. Using the continuous-time interpretation of HHC in Equation (2.9), it can be seen that the relaxation factor $\alpha < 1$ essentially decreases the static gain, thus stabilizes the system while slowing down the response, consistent with the simulation results obtained by Patt *et al.*

2.1.3 Adaptive Higher Harmonic Control

In the HHC algorithms discussed above, the control response matrix $\mathbf{T}$ is obtained either through modeling or experimentation, and implemented in the control structure shown in Figure 2-1 or Figure 2-3. An alternative method is to estimate $\mathbf{T}$ online, and then implement it in the controller. The online estimation can be accomplished using either the recursive least squares method, or the Kalman filtering method. The combination of online identification of $\mathbf{T}$ matrix and Shaw's HHC algorithm is referred to as the adaptive HHC. A comprehensive review of various adaptive HHC algorithms was provided by Johnson [57].

To obtain the estimates of the elements in the matrix $\mathbf{T}$, the quasisteady model equation is rewritten as

$$\Delta \mathbf{z}_n = \mathbf{T} \Delta \mathbf{u}_n \tag{2.13}$$

where

$$\Delta \mathbf{u}_n = \mathbf{u}_n - \mathbf{u}_{n-1} \tag{2.14}$$

$$\Delta \mathbf{z}_n = \mathbf{z}_n - \mathbf{z}_{n-1} \tag{2.15}$$

Measurements up to step n are concatenated to give

$$\Delta \mathbf{Z}_n = \mathbf{T} \Delta \mathbf{U}_n \tag{2.16}$$

where

$$\Delta \mathbf{U}_n = \begin{bmatrix} \mathbf{u}_1 & \mathbf{u}_2 & \dots & \mathbf{u}_n \end{bmatrix} \tag{2.17}$$

$$\Delta \mathbf{Z}_n = \begin{bmatrix} \mathbf{z}_1 & \mathbf{z}_2 & \dots & \mathbf{z}_n \end{bmatrix} \tag{2.18}$$

The least squares estimate of $\mathbf{T}$ is

$$\hat{\mathbf{T}}_n = \Delta \mathbf{Z}_n \Delta \mathbf{U}_n^T \mathbf{P}_n \tag{2.19}$$

where

$$\mathbf{P}_n = \left(\Delta \mathbf{U}_n \Delta \mathbf{U}_n^T \right)^{-1} \tag{2.20}$$

and the inverse is assumed to exist. From the least squares estimate shown in Equation (2.19), Patt *et al.* derived the following equations for the recursive least squares estimate of $\mathbf{T}$

$$\mathbf{K}_{n+1} = \left(1 + \Delta \mathbf{u}_{n+1}^T \mathbf{P}_n \Delta \mathbf{u}_{n+1} \right)^{-1} \Delta \mathbf{u}_{n+1}^T \mathbf{P}_n \tag{2.21}$$

$$\hat{\mathbf{T}}_{n+1} = \hat{\mathbf{T}}_n + \left(\Delta \mathbf{z}_{n+1} - \hat{\mathbf{T}}_n \Delta \mathbf{u}_{n+1} \right) \mathbf{K}_{n+1} \tag{2.22}$$

$$\mathbf{P}_{n+1} = \mathbf{P}_n \left(I - \Delta \mathbf{u}_{n+1} \mathbf{K}_{n+1} \right) \tag{2.23}$$

The adaptive HHC algorithm is completed by substituting $\hat{\mathbf{T}}_{n+1}$ obtained in Equation (2.22) for $\mathbf{T}$ in either Equation (2.5) or Equation (2.12). In the case that the elements of $\mathbf{T}$ are assumed to be time-varying, then an exponential window should be applied to de-emphasize the older measurements. The exponential window is applied by replacing Equations (2.21) and (2.23) with

$$\mathbf{K}_{n+1} = \left(\gamma + \Delta \mathbf{u}_{n+1}^T \mathbf{P}_n \Delta \mathbf{u}_{n+1} \right)^{-1} \Delta \mathbf{u}_{n+1}^T \mathbf{P}_n \tag{2.24}$$

$$\mathbf{P}_{n+1} = \mathbf{P}_n \left(\gamma^{-1} I - \Delta \mathbf{u}_{n+1} \mathbf{K}_{n+1} \right) \tag{2.25}$$

where $0 < \gamma < 1$.

In addition to online estimation of $\mathbf{T}$, some adaptive HHC algorithms also estimate the

baseline levels of vibration $\mathbf{z}_0$ online. Although as discussed by Hall and Wereley [44], the output of the integrators in Figure 2-3 are estimates of the in-phase and quadrature components of the harmonic disturbance. Thus the HHC algorithm implicitly estimates $\mathbf{z}_0$, and explicit estimation of the baseline vibration is not needed.

The main reason cited for using adaptive HHC is to account for uncertainties in the $\mathbf{T}$ matrix [74]. However, Shaw *et al.* have demonstrated the effectiveness of the fixed-gain HHC algorithm in different flight conditions experimentally [87], and Hall and Wereley have shown the fixed-gain HHC algorithm to be quite robust to plant variations [44].

2.2 Linear Time-Invariant Plant

Assuming the periodicity effect on the helicopter rotor dynamics is small, then a linear time-invariant (LTI) system would be a suitable candidate as the plant model. The LTI system is described by the state-space model

$$\dot{x}_p(t) = A_p x_p(t) + B_p u(t) \tag{2.26}$$

$$y_p(t) = C_p x_p(t) + D_p u(t) \tag{2.27}$$

$$z(t) = y_p(t) + d(t) \tag{2.28}$$

where $x_p \in \mathbb{R}^{n_p}$ is the state vector of the plant, $u \in \mathbb{R}^{n_u}$ is the control input, $y_p \in \mathbb{R}^{n_y}$ is the plant output, $z \in \mathbb{R}^{n_y}$ is the performance output to be controlled, $d \in \mathbb{R}^{n_y}$ is the harmonic disturbance with frequency $N\Omega$, and A_p, B_p, C_p, and D_p are matrices of the appropriate dimensions. The transfer function from the input u to the performance variable z is

$$G(s) = C_p(sI - A_p)^{-1}B_p + D_p \tag{2.29}$$

For the discussion in this section, we consider a single-input/single-output (SISO) plant. Most of the results presented below can be generalized to the multi-input/multi-output (MIMO) case with suitable modifications,.

2.2.1 Continuous-Time Higher Harmonic Control

In the quasisteady case examined earlier, the continuous-time controller is given by

$$K(s) = 2k\frac{as + bN\Omega}{s^2 + (N\Omega)^2} \tag{2.30}$$

where the coefficients a and b are the elements in the inverse control response matrix

$$\mathbf{T}^{-1} = \begin{bmatrix} a & b \\ -b & a \end{bmatrix} \tag{2.31}$$

Under the LTI assumption, the coefficients a and b of Equation (2.30) can be obtained by evaluating the system transfer function $G(s)$ at the harmonic frequency $N\Omega$ as [44]

$$a = \text{real}\left(\frac{1}{G(jN\Omega)}\right) \tag{2.32}$$

$$b = -\text{imag}\left(\frac{1}{G(jN\Omega)}\right) \tag{2.33}$$

The sensitivity transfer function is the closed-loop system transfer function from the disturbance d to the output z. For a negative feedback control system, it is given by

$$S(s) = \frac{1}{1 + L(s)} \tag{2.34}$$

where

$$L(s) = G(s)K(s) \tag{2.35}$$

is the loop transfer function. The magnitude of the sensitivity transfer function is the level of attenuation or amplification of the disturbance. With the controller given by Equation (2.30), it can be seen from Equation (2.34) that

$$S(jN\Omega) = 0 \tag{2.36}$$

Equation (2.36) implies that any disturbance with frequency equal to $N\Omega$ will be completely rejected by the controller $K(s)$ in the closed-loop system, regardless of the static

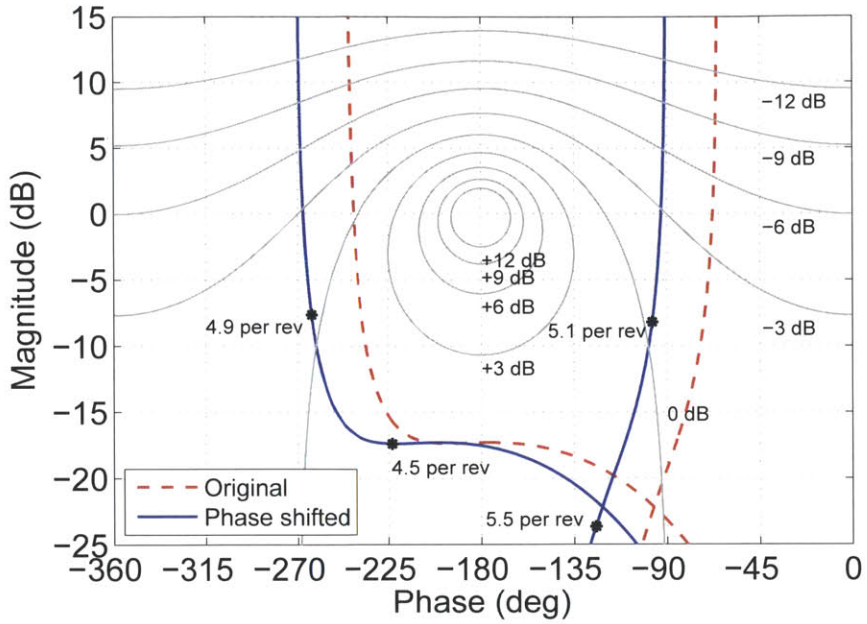

Figure 2-4: Nichols plots for a typical loop transfer function of the helicopter rotor and continuous-time HHC

gain k, and the coefficients a and b in the numerator. Note that $s = \pm jN\Omega$ are the poles of the controller $K(s)$, hence the controller gain at the harmonic frequency is infinite, resulting in complete rejection of the harmonic disturbance.

The stability margins of the closed-loop system are related to the maximum amplitude of $S(s)$. A lower value of the maximum amplitude of $S(s)$ guarantees greater gain and phase margins. The parameters k, a, and b can be chosen, based on the plant dynamics, to minimize the maximum amplitude of $S(s)$, resulting in a controller with greater stability margins.

Shin, Cesnik, and Hall [88] used the Nichols plot to determine the amount of phase shift ϕ of the plant dynamics needed to decrease the maximum amplitude of $S(s)$ to an acceptable level, thus achieving the desired gain and phase margins. The value of the plant transfer function used to determine the coefficients a and b of the controller in Equations (2.32) and (2.33) is

$$G(jN\Omega)e^{-j\phi} \tag{2.37}$$

As an example, Figure 2-4 shows the Nichols plot of a typical loop transfer function with a continuous-time HHC in red dashed line. The contour lines in the figure represent constant

values of $|S(s)|$. The solid blue line is the loop transfer function with a controller obtained from the plant with a phase shift $\phi = -25$ deg. The points marked by asterisks show the direction of increasing frequency. The controller designed with the phase shifted plant has approximately 25 deg more phase margin, and also a slight increase in gain margin.

Shin, Cesnik, and Hall [88] also examined reducing vibration at different harmonic frequencies using multiple modes of actuation. The multi-mode controller is a summation of individual continuous-time controllers, it has the form

$$K(s) = \sum_i \frac{2}{T_i} \frac{a_i s + a_i N_i \Omega}{s^2 + (N_i \Omega)^2} \tag{2.38}$$

where the subscript i is an index of different combinations of mode of actuation and the harmonic frequency to be attenuated. The multi-mode controller was implemented with an anti-windup algorithm developed for the parallel integrators of the demodulation/modulation structure of the continuous-time HHC. The anti-windup mechanism is incorporated in the demodulation/modulation structure as shown in Figure 2-5, and the logic is given by

$$\dot{\mathbf{v}} = \begin{cases} 2k\mathbf{u}, & \text{if } |\mathbf{v}| < \mathrm{v_{sat}}, \text{ or } |\mathbf{v}| > \mathrm{v_{sat}} \text{ and } (\mathbf{u} \cdot \mathbf{v}) < 0 \\ 2k\left[\mathbf{u} - (\mathbf{u} \cdot \mathbf{n})\mathbf{n} - \alpha_v(|\mathbf{v}| - \mathrm{v_{sat}})\mathbf{n}\right], & \text{if } |\mathbf{v}| > \mathrm{v_{sat}}, \text{ and } (\mathbf{u} \cdot \mathbf{n}) > 0 \end{cases} \tag{2.39}$$

where

$$\mathbf{v} = \begin{bmatrix} v_1 \\ v_2 \end{bmatrix} \tag{2.40}$$

$$\mathbf{u} = \begin{bmatrix} u_1 \\ u_2 \end{bmatrix} \tag{2.41}$$

and $\mathbf{n}$ is the outward unit normal vector given by

$$\mathbf{n} = \mathbf{v}/|\mathbf{v}| \tag{2.42}$$

For each individual controller, a maximum allowable amplitude $\mathrm{v_{sat}}$ was assigned, and α_v

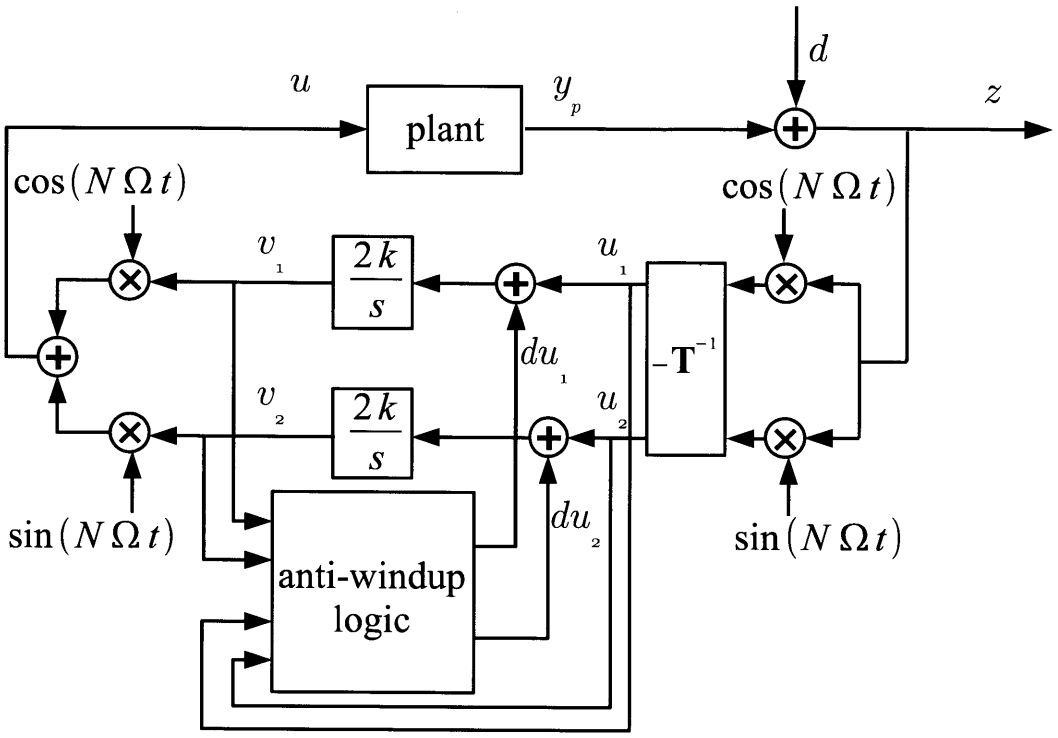

Figure 2-5: Continuous-time higher harmonic controller with anti-windup algorithm

was chosen to provide the desired convergence rate of the control vector. The anti-windup logic prevents degradation of performance in the case of actuator saturation.

2.2.2 Frequency Weighted Linear Quadratic Regulator

Gupta and Du Val proposed applying a modified version of the linear quadratic regulator (LQR) method to solve the helicopter vibration problem [40, 41]. The constant weighting matrices in a typical LQR cost functional place equal emphasis at all frequencies. Gupta and Du Val proposed a generalized frequency domain cost functional of the form

$$J = \int_{-\infty}^{\infty} [z^*(j\omega)Q_{zz}(j\omega)z(j\omega) + \rho u*(j\omega)u(j\omega)]\, d\omega \tag{2.43}$$

where Q_{zz} is a dynamic weighting filter, and * denotes complex conjugation. The weighting filter is assumed to have the spectral factorization

$$Q_{zz}(j\omega) = P^*(j\omega)P(j\omega) \tag{2.44}$$

For harmonic disturbance rejection, the filter

$$P(j\omega) = \frac{j\omega(N\Omega)^2}{-\omega^2 + (N\Omega)^2} \tag{2.45}$$

is chosen to provide infinite weighting at the harmonic frequency $\omega = N\Omega$. A state-space realization of $P(j\omega)$ is given by

$$\dot{x}_w(t) = A_w x_w(t) + B_w z(t) \tag{2.46}$$

$$z_w(t) = C_w x_w(t) \tag{2.47}$$

where z_w is the weighted variable to be controlled, and

$$A_w = \begin{bmatrix} 0 & 1 \\ -(N\Omega)^2 & 0 \end{bmatrix} \tag{2.48}$$

$$B_w = \begin{bmatrix} 0 \\ (N\Omega)^2 \end{bmatrix} \tag{2.49}$$

$$C_w = \begin{bmatrix} 0 & 1 \end{bmatrix} \tag{2.50}$$

The augmented state-space model, which contains the additional dynamics introduced by the weighting filter $P(j\omega)$, is

$$\dot{x}(t) = Ax(t) + Bu(t) \tag{2.51}$$

$$z_w(t) = Cx(t) \tag{2.52}$$

where the augmented state vector is

$$x = \begin{bmatrix} x_p \\ x_w \end{bmatrix} \tag{2.53}$$

and the state-space matrices are

$$A = \begin{bmatrix} A_p & 0 \\ B_w C_p & A_w \end{bmatrix} \tag{2.54}$$

$$B = \begin{bmatrix} B_p \\ 0 \end{bmatrix} \tag{2.55}$$

$$C = \begin{bmatrix} 0 & C_w \end{bmatrix} \tag{2.56}$$

The cost functional in Equation (2.43) can be expressed in terms of the augmented state-space plant as

$$J = \int_0^\infty \left[z_w^2(t) + \rho u^2(t) \right] dt \tag{2.57}$$

The resulting full state feedback law is

$$u = -gx \tag{2.58}$$

$$= -\begin{bmatrix} g_p & g_w \end{bmatrix} \begin{bmatrix} x_p \\ x_w \end{bmatrix} \tag{2.59}$$

where the gain g is given by

$$g = \frac{1}{\rho} B^T X \tag{2.60}$$

and S is the solution to the algebraic Riccati equation

$$0 = A^T X + XA + C^T C - \frac{1}{\rho} XBB^T X \tag{2.61}$$

Since the rotor and fuselage states are not easily obtained, Du Val, Gregory and Gupta [27] investigated a simplified controller using feedback on just the weighting filter state x_w. The transfer function of the resulting output feedback controller is

$$K(s) = \frac{(g_{w_2} s + g_{w_1})(N\Omega)^2}{s^2 + (N\Omega)^2} \tag{2.62}$$

where g_{w_1} and g_{w_2} are the elements of g_w given by

$$g_w = \begin{bmatrix} g_{w_1} & g_{w_2} \end{bmatrix} \tag{2.63}$$

To account for the phase lag of the actuator, an additional derivative factor

$$\frac{s}{N\Omega} \tag{2.64}$$

is included in the controller to add 90 deg of phase. The derivative factor also decreases the controller gains in low frequencies, which reduces adverse effects on the rotor and fuselage dynamics.

The transfer function in Equation (2.62) has the same classical narrowband disturbance rejection controller form as in the continuous-time HHC. The poles of Equation (2.62) are the poles of the weighting filter $P(j\omega)$, which is a harmonic oscillator with a natural frequency of $N\Omega$. The inclusion of a model of the disturbance in the controller is known as the internal model principle [31], and serves as another interpretation for the common structure shared by the continuous-time HHC method and the frequency weighted LQR method.

2.3 Linear Time-Periodic Plant

The state-space representation of a linear time-periodic (LTP) system is

$$\dot{x}_p(t) = A_p(t)x_p(t) + B_p(t)u(t) \tag{2.65}$$

$$y_p(t) = C_p(t)x_p(t) + D_p(t)u(t) \tag{2.66}$$

$$z(t) = y_p(t) + d(t) \tag{2.67}$$

which differs from the LTI model in that the matrices $A_p,\ B_p,\ C_p,\ D_p$ are periodic with period T, *i.e.*,

$$A_p(t+T) = A_p(t) \tag{2.68}$$

$$B_p(t+T) = B_p(t) \tag{2.69}$$

$$C_p(t+T) = C_p(t) \tag{2.70}$$

$$D_p(t+T) = D_p(t) \tag{2.71}$$

The vectors $x_p,\ y_p,\ z,\ u$, and d in Equations (2.65) - (2.67) are analogous to their counterparts in the LTI system described by Equations (2.26) - (2.28).

2.3.1 Harmonic Transfer Functions

The notion of the transfer function is not well defined for an LTP system, since a complex exponential input to an LTP system results in an output with an infinite number of harmonics. Wereley and Hall [102] used the exponentially modulated periodic (EMP) signal to derive the frequency response of an LTP system.

An EMP signal can be expressed as

$$u(t) = e^{st} \sum_{n \in \mathbb{Z}} u_n e^{jn\omega_p t} \tag{2.72}$$

$$= \sum_{n \in \mathbb{Z}} u_n e^{s_n t} \tag{2.73}$$

where $u_n,\ n \in \mathbb{Z}$, are the complex Fourier coefficients of a periodic signal with frequency ω_p, and $s_n = s + jn\omega_p$. The relationship between the EMP signal and the LTP system is analogous to the relationship between the complex exponential function and the LTI system. Input signals in the form of Equation (2.73) lead to a frequency domain representation of the LTP system called the harmonic transfer function (HTF).

In order to obtain the HTF of an LTP system, Wereley and Hall first note that the steady-state response of an LTP system to an EMP input $u(t)$ is also an EMP signals, *i.e.*,

$$x_p(t) = \sum_{n\in\mathbb{Z}} x_n e^{s_n t} \tag{2.74}$$

$$\dot{x}_p(t) = \sum_{n\in\mathbb{Z}} s_n x_n e^{s_n t} \tag{2.75}$$

$$y_p(t) = \sum_{n\in\mathbb{Z}} y_n e^{s_n t} \tag{2.76}$$

Second, the system dynamics matrix $A_p(t)$ can be expanded in a complex Fourier series as

$$A_p(t) = \sum_{m\in\mathbb{Z}} A_m e^{jm\omega_p t} \tag{2.77}$$

The matrices $B_p(t)$, $C_p(t)$, and $D_p(t)$ can also be expressed as complex Fourier series in a similar fashion.

Expanding the LTP state-space Equations (2.65) and (2.66) in terms Equations (2.73) - (2.77) results in the harmonic state-space model

$$s\mathcal{X} = (\mathcal{A} - \mathcal{N})\mathcal{X} + \mathcal{B}\mathcal{U} \tag{2.78}$$

$$\mathcal{Y} = \mathcal{C}\mathcal{X} + \mathcal{D}\mathcal{U} \tag{2.79}$$

where $\mathcal{A}$ is a Toeplitz form composed of the complex Fourier coefficient matrices A_m, $m \in \mathbb{Z}$,

$$\mathcal{A} = \begin{bmatrix} \ddots & \vdots & \vdots & \vdots & \vdots & \vdots & \\ \cdots & A_0 & A_{-1} & A_{-2} & A_{-3} & A_{-4} & \cdots \\ \cdots & A_1 & A_0 & A_{-1} & A_{-2} & A_{-3} & \cdots \\ \cdots & A_2 & A_1 & A_0 & A_{-1} & A_{-2} & \cdots \\ \cdots & A_3 & A_2 & A_1 & A_0 & A_{-1} & \cdots \\ \cdots & A_4 & A_3 & A_2 & A_1 & A_0 & \cdots \\ & \vdots & \vdots & \vdots & \vdots & \vdots & \ddots \end{bmatrix} \tag{2.80}$$

with the matrices $\mathcal{B}$, $\mathcal{C}$, and $\mathcal{D}$ similarly formed from the complex Fourier coefficient matrices B_m, C_m, and D_m of the the state-space matrices $B_p(t)$, $C_p(t)$, and $D_p(t)$. The matrix $\mathcal{N}$ is an infinite block diagonal matrix given by

$$\mathcal{N} = \text{diag}\left(jn\omega_p I;\ n \in \mathbb{Z}\right) \tag{2.81}$$

The infinite harmonic vectors $\mathcal{X}, \mathcal{U}$, and $\mathcal{Y}$ are formed by stacking the Fourier coefficients of $x_p(t)$, $y_p(t)$, and $u(t)$

$$\mathcal{X}^T = \begin{bmatrix} \dots & x_{-2}^T & x_{-1}^T & x_0^T & x_1^T & x_2^T & \dots \end{bmatrix} \tag{2.82}$$

$$\mathcal{Y}^T = \begin{bmatrix} \dots & y_{-2} & y_{-1} & y_0 & y_1 & y_2 & \dots \end{bmatrix} \tag{2.83}$$

$$\mathcal{U}^T = \begin{bmatrix} \dots & u_{-2} & u_{-1} & u_0 & u_1 & u_2 & \dots \end{bmatrix} \tag{2.84}$$

The frequency domain relationship between harmonic input vector $\mathcal{U}$ and the harmonic output vector $\mathcal{Y}$

$$\mathcal{Y} = \hat{\mathcal{G}}(s)\mathcal{U} \tag{2.85}$$

results directly from the harmonic state-space model, where the harmonic transfer function $\hat{\mathcal{G}}(s)$ is given by

$$\hat{\mathcal{G}}(s) = \mathcal{C}\left(s\mathcal{I} - (\mathcal{A} - \mathcal{N})\right)^{-1}\mathcal{B} + \mathcal{D} \tag{2.86}$$

For practical usage, the harmonic transfer function must be truncated, retaining the non-trivial terms in the Fourier series expansion of $\mathcal{A}$, $\mathcal{B}$, $\mathcal{C}$, and $\mathcal{D}$. In the case that only the coefficient matrices A_0, B_0, C_0, and D_0 are significant, the HTF reduces to a transfer function, and the LTP system can be simply represented by an LTI system.

2.3.2 Periodic Disturbance Rejection Control

An observer based periodic controller was developed by Arcara, Bittanti, and Lovera [3] to attenuate the vibration of the main rotor in forward flight. The plant model was an analytical model of the helicopter rotor in constant speed flight in the state-space form given by Equations (2.65) - (2.67).

The controller proposed by Arcara, Bittanti, and Lovera is designed to optimize the performance index

$$J = E\left\{\lim_{t\to\infty}\frac{1}{2t}\int_{-t}^{t}\left[\tilde{x}_p^T(t)Q\tilde{x}_p(t) + \tilde{u}^T(t)R\tilde{u}(t)\right]dt\right\} \tag{2.87}$$

for an equivalent LTP system with the state-space representation

$$\dot{\tilde{x}}_p(t) = A_p(t)\tilde{x}_p(t) + B_p(t)\tilde{u}(t) \tag{2.88}$$

$$z(t) = C_p(t)\tilde{x}(t) + D_p(t)\tilde{u}(t) \tag{2.89}$$

where

$$\tilde{u} = u(t) + \tilde{d}(t) \tag{2.90}$$

and $\tilde{d}(t)$ is the input equivalent disturbance.

The equivalent input disturbance has the Fourier series expansion

$$\tilde{d}(t) = \sum_{k=0}^{\infty}\tilde{d}^{(k)}(t) \tag{2.91}$$

where $\tilde{d}^{(k)}(t)$ is a sinusoidal signal with frequency $k\Omega$. For practical reasons, only r sinusoids are used to approximate $\tilde{d}(t)$. Each $\tilde{d}^{(k)}(t)$ is generated by a harmonic oscillator with the state-space representation

$$\dot{x}_w^{(k)}(t) = A_w^{(k)}x_w^{(k)}(t) + n^{(k)}(t) \tag{2.92}$$

$$\tilde{d}^{(k)}(t) = C_w^{(k)}x_w^{(k)}(t) \tag{2.93}$$

where

$$A_w^{(k)} = \begin{bmatrix} 0 & -(k\Omega)^2 \\ 1 & 0 \end{bmatrix} \tag{2.94}$$

$$C_w^{(k)} = \begin{bmatrix} 1 & 0 \end{bmatrix} \tag{2.95}$$

and $n^{(k)}(t)$ is a white noise vector. Combining the r state-space models of $\tilde{d}^{(k)}(t)$, $k =$

$1, 2, \ldots, r$ in parallel results in the global disturbance model

$$\dot{x}_w(t) = A_w x_w(t) + n(t) \tag{2.96}$$

$$\tilde{d}(t) = C_w x_w(t) \tag{2.97}$$

The global disturbance model is augmented to the plant model given by Equations (2.88) and (2.89) to form a combined model with the state vector given by

$$x = \begin{bmatrix} \tilde{x}_p \\ x_w \end{bmatrix} \tag{2.98}$$

A Kalman filter is designed to estimate the state vector x of the combined model, the estimated state vector is denoted by

$$\hat{x} = \begin{bmatrix} \hat{\tilde{x}}_p \\ \hat{x}_w \end{bmatrix} \tag{2.99}$$

The input equivalent disturbance is obtained using Equation (2.97), with $\hat{x}_w(t)$ in place of $x_w(t)$.

With the cost functional given by Equation (2.87), and the plant model given by Equations (2.88) and (2.89), the optimal control law is

$$u(t) = \tilde{u}(t) - \tilde{d}(t) = k(t)\tilde{x}_p(t) - \tilde{d}(t) \tag{2.100}$$

where

$$k(t) = -R^{-1}B^T(t)P(t) \tag{2.101}$$

and $P(t)$ is the positive semidefinite periodic solution to the periodic Riccati equation [6]

$$-\dot{P}(t) = A_p^T(t)P(t) + P(t)A_p(t) + Q - P(t)B_p(t)R^{-1}B_p^T(t)P(t) \tag{2.102}$$

The state feedback control law in Equation (2.100) is implemented using the estimated state from the Kalman filter as shown in Figure 2-6.

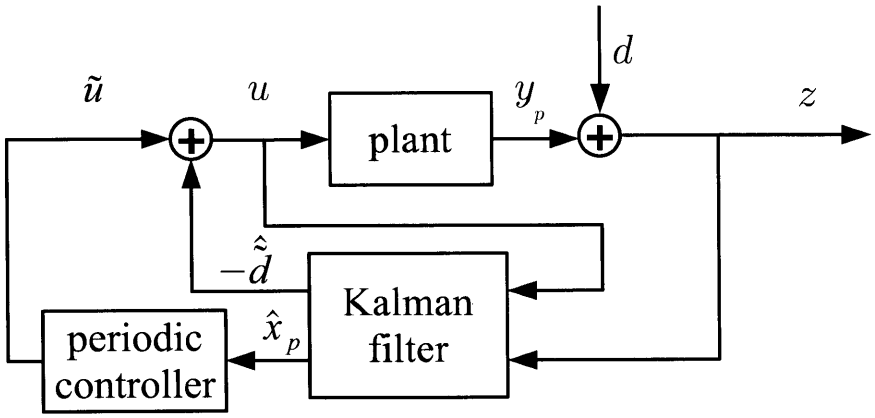

Figure 2-6: Implementation of periodic controller for harmonic disturbance rejection

2.4 Summary

In this chapter, we examined three different types of systems that have been used to model the dynamics of helicopter rotor for control design, and the associated methods for harmonic disturbance rejection controller synthesis.

The quasisteady T matrix approach was used in Shaw's original HHC formulation in discrete-time. Estimation of the T matrix can be performed online, resulting in the adaptive HHC algorithm. A continuous-time version of Shaw's algorithm was presented by Hall and Wereley. The continuous-time HHC naturally leads to control synthesis using LTI models. The LTI models allow the controller to account for the dynamics of the helicopter rotor, which results in improved robustness and performance. A method using the Nichols plot to improve the gain and phase margin was introduced by Shin, Cesnik, and Hall, who also extended the continuous-time HHC to attenuate multiple harmonic disturbances using different modes of actuation. The LTI representation of the helicopter rotor dynamics was used by Gupta and Du Val in a linear quadratic regulator approach to design harmonic disturbance rejection controller. For LTP models, Arcara, Bittanti, and Lovera proposed a procedure to design observer based periodic controllers for harmonic disturbance rejection.

All the methods described above, despite the difference in plant models, make use of a harmonic oscillator either directly in the controller structure, or in the weighting function of the performance index. In the case of the periodic controller, the sinusoidal disturbance model is introduced by the Kalman estimator, which contains the augmented dynamics of

the harmonic oscillator.

Chapter 3

$\mathcal{H}_\infty$ Higher Harmonic Controller

In this chapter, we address the problem of higher harmonic vibration reduction in helicopters using $\mathcal{H}_\infty$ control theory. We first discuss the nature of the harmonic disturbance based on wind tunnel test data. Then we define a performance measure for harmonic disturbance rejection based on the idea of a weighting filter. Specifically, we use two parameters, peak sensitivity and bandwidth, to define both the weighting filter, and the controller performance. The weighting filter is used in the synthesis of the full-order $\mathcal{H}_\infty$ controller for harmonic disturbance rejection. Using higher order weighting filters, the resulting $\mathcal{H}_\infty$ controllers establish the performance limits that can be achieved in terms of peak sensitivity and bandwidth.

In order to examine the performance of the controller using the framework of linear control theory, we represents the plant by the state-space model

$$\dot{x}_p(t) = A_p x_p(t) + B_p u(t) \tag{3.1}$$

$$y_p(t) = C_p x_p(t) \tag{3.2}$$

$$y(t) = C_p x_p(t) + d(t) \tag{3.3}$$

where $x_p \in \mathbb{R}^{n_p}$ is the plant state vector, $u \in \mathbb{R}^{n_u}$ is the control input, $y_p \in \mathbb{R}^{n_y}$ is the plant output, $y \in \mathbb{R}^{n_y}$ is the measured output, which includes $d \in \mathbb{R}^{n_y}$, the open-loop disturbance, A_p, B_p, and C_p are real matrices of appropriate dimensions. In our case, the plant is a model of the helicopter rotor dynamics at a fixed operating flight condition.

Our model of the helicopter rotor is a single-input, single-output (SISO) system, with the input $u \in \mathbb{R}$ representing the collective voltage applied to the on-blade actuators, $y_p \in \mathbb{R}$ representing the normal force produced by the rotor minus the nominal lift force, and $y \in \mathbb{R}$ representing the measured normal force at the rotor minus the nominal lift force. The procedure for controller synthesis we describe subsequently is applicable to the general multiple-input, multiple-output (MIMO) case with appropriate generalizations of the SISO case.

3.1 Disturbance Rejection Performance

In order to reduce the effect of the disturbance $d(t)$, we use a linear time-invariant output feedback control law, expressed in the frequency domain as

$$U(s) = K(s)Y(s) \tag{3.4}$$

where $K(s)$ is the transfer function of the feedback controller, $U(s)$ is the Laplace transform of $u(t)$, and $Y(s)$ is the Laplace transform of $y(s)$. The closed-loop transfer function from the disturbance $d(t)$ to the measured output $y(t)$ is the sensitivity transfer function $S(s)$

$$\frac{Y(s)}{D(s)} = S(s) = (1 - G(s)K(s))^{-1} \tag{3.5}$$

where $D(s)$ is the Laplace transform of $d(t)$, and $G(s)$ is the plant transfer function from the control input $u(t)$ to the plant output $y_p(t)$ given by

$$\frac{Y_p(s)}{U(s)} = G(s) = C_p(sI - A_p)^{-1}B_p \tag{3.6}$$

where $Y_p(s)$ is the Laplace transform of $y_p(t)$. The magnitude of $S(j\omega)$ is the attenuation (or amplification if $|S(j\omega)| > 1$) of a disturbance at frequency ω by the closed-loop system.

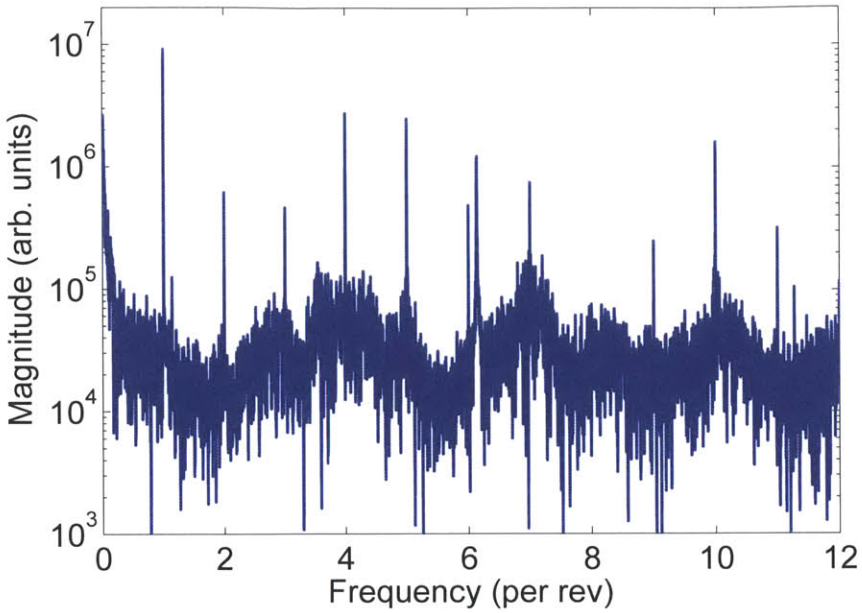

Figure 3-1: Spectrum of the rotor normal force in Flight Condition 1

Table 3.1: Flight condition for wind tunnel testing

Flight Condition	1
Velocity, V (kt)	83
Advance ratio, μ	0.20
Tip Mach number, M_{T}	0.623
Advancing tip Mach number, M_{AT}	0.746
Shaft angle, α (deg)	2.0
Blade loading coefficient, C_{T}/σ	0.075

3.1.1 Bandwidth

Data from wind tunnel tests conducted by Hall *et al.* show that significant levels of vibration exist at almost all harmonic frequencies within the test frequency range [42]. Figure 3-1 shows spectrum of the open-loop rotor hub normal force for Flight Condition 1, which is described in Table 3.1. The spectrum at the harmonic frequencies are essentially impulses, which implies the disturbance $d(t)$ in Equation (3.3) contain sinusoidal components with frequency $n\Omega,\ n = 1, 2, \ldots$, where $\Omega = 1$ per rev is the fundamental frequency.

From the definition of the sensitivity function $S(s)$ in Equation (3.5), we can eliminate the harmonic disturbances in the closed-loop response if

$$|S(jn_i\Omega)| = 0, \quad \forall n_i,\ i = 1, 2, \ldots, M \tag{3.7}$$

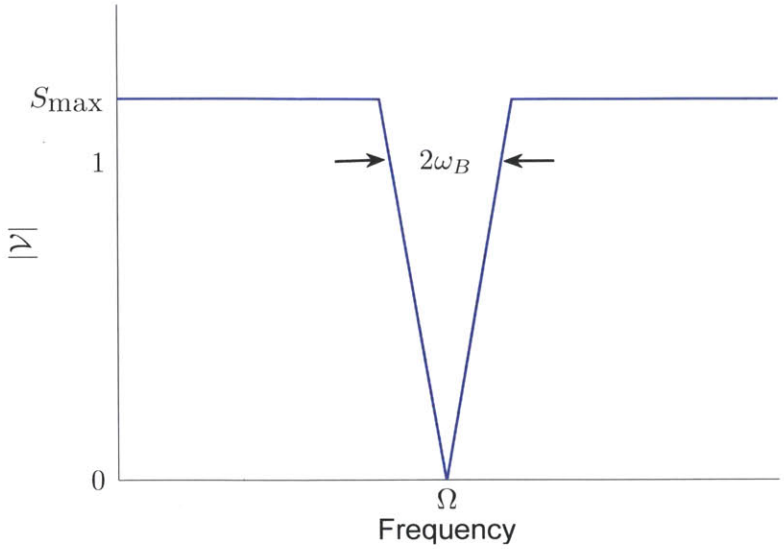

Figure 3-2: Ideal linear notch at $\omega = \Omega$

where $n_i\Omega,\ i = 1, 2, \ldots, M$ are the frequencies of the higher harmonic disturbances to be attenuated.

Equation (3.7) implies there are notches in the sensitivity function at $\omega = n_i\Omega,\ i = 1, 2, \ldots, M$. The notion of *bandwidth* of the controller is associated with the width of these notches. A wider notch corresponds to a greater bandwidth, and a large bandwidth is desired because it would lead to faster response to changes in the harmonic disturbances. In particular, we consider an ideal piecewise linear notch as shown in Figure 3-2. The width of the ideal notch is inversely proportional to its slope, and since the ideal notch is symmetric about the harmonic frequency, we define the bandwidth ω_B as the largest ω_B such that

$$|S(j\omega)| \leq \frac{1}{\omega_B} |\omega - n_i\Omega|, \quad \forall \omega \in \mathbb{R} \tag{3.8}$$

3.1.2 Peak Sensitivity

The disturbance $d(t)$ in Equation (3.3) may also contain broadband noise in addition to the harmonic components, and to ensure that the effect of the broadband noise is not amplified

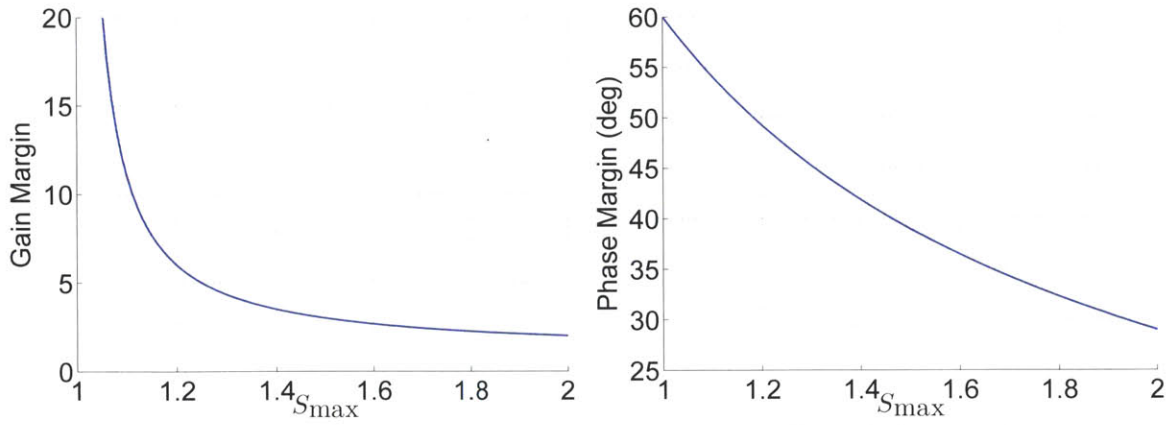

(a) $S_{\max}$ and gain margin

(b) $S_{\max}$ and phase margin

Figure 3-3: Relationship between $S_{\max}$ and gain and phase margins

significantly, we require that the *peak sensitivity*, defined as

$$S_{\max} = \sup_{\omega} |S(j\omega)| = \|S\|_{\infty} \tag{3.9}$$

to be no greater than some specified threshold level. The peak sensitivity will be at least unity, because the loop gain $G(j\omega)K(j\omega) \to 0$ as $\omega \to \infty$, and so $S(j\omega) \to 1$ as $\omega \to \infty$. In general, it is desirable for the peak sensitivity to be as small as possible for two reasons. First, the peak sensitivity is the maximum amplification of vibration at non-harmonic frequencies. While the vibration away from the harmonic frequency is usually small, it is still undesirable to amplify those vibrations. Second, and more importantly, lower peak sensitivities correspond to higher gain and phase margins [91]. In particular, the gain margin (GM) and phase margin (PM) are bounded by

$$\text{GM} \geq \frac{S_{\max}}{S_{\max} - 1} \tag{3.10}$$

$$\text{PM} \geq 2 \arcsin\left(\frac{1}{2S_{\max}}\right) \tag{3.11}$$

The relationships between $S_{\max}$ and both the gain and phase margins are shown in Figure 3-3, and as an example, $S_{\max} = 1.2$ implies GM ≥ 6 and PM ≥ 49.2 deg.

3.1.3 Controller Performance Analysis

The $\mathcal{H}_\infty$ framework can be used to determine whether a given higher harmonic control system has a specified bandwidth ω_B, and peak sensitivity of $S_{\max}$. To do this, we first need to create a function of frequency $\mathcal{V}(\omega; \omega_B, S_{\max})$ that meets the required bandwidth and peak sensitivity requirements, such a function is illustrated in Figure 3-2. Then the control system has peak sensitivity less than $S_{\max}$ and bandwidth greater than ω_B if and only if

$$|S(j\omega)| \leq \mathcal{V}(\omega; \omega_B, S_{\max}), \quad \forall \omega \in \mathbb{R} \tag{3.12}$$

The bound in Equation (3.12) can be rewritten as

$$|\mathcal{W}(j\omega; \omega_B, S_{\max})S(j\omega)| \leq 1, \quad \forall \omega \in \mathbb{R} \tag{3.13}$$

where $\mathcal{W}(j\omega; \omega_B, S_{\max})$ is any causal transfer function such that

$$|\mathcal{W}(j\omega; \omega_B, S_{\max})| = \mathcal{V}^{-1}(\omega; \omega_B, S_{\max}) \tag{3.14}$$

Then Equation (3.13) is equivalent to

$$\|\mathcal{W}S\|_\infty \leq 1 \tag{3.15}$$

That is, the problem of determining whether the harmonic disturbance rejection controller meets the desired specification is equivalent to the problem of determining whether the infinity norm of the transfer function $\mathcal{W}S$ is less than or equal to unity. Numerically efficient methods have been developed for determining the infinity norm of rational transfer functions expressed in state-space form [25]. Unfortunately, we cannot simply take $\mathcal{W}(j\omega; \omega_B, S_{\max}) = \mathcal{V}^{-1}(\omega; \omega_B, S_{\max})$, because the resulting transfer function is not rational. In the following section, rational transfer functions approximating different notch shapes are developed.

3.2 Notch Filters

In this section, we present the linear and parabolic notch filters, both defined in terms of bandwidth ω_B and peak sensitivity $S_{\max}$, that when inverted, can be used as weighting filters in the analysis of controllers performance.

3.2.1 Linear Notch

We first consider a piecewise linear ideal notch filter $H(j\omega)$, with the bandwidth defined as the largest ω_B that satisfies Equation (3.8)

To simplify the derivation, we develop the filter for the case $\Omega = 0$ and $\omega_B = 1$ first, and subsequently introduce the transformation to obtain the general filter. The magnitude of such an ideal linear notch filter is given by

$$|H(j\omega)| = \begin{cases} |\omega|, & |\omega| < 1 \\ 1, & |\omega| \geq 1 \end{cases} \tag{3.16}$$

An approximation to the squared magnitude of H is

$$|H_m(j\omega)|^2 = \frac{\omega^2(\omega^{2m} - 1)}{\omega^{2m+2} - 1}, \quad m = 1, 2, \ldots \tag{3.17}$$

It is easily verified that as the order of approximation $m \to \infty$,

$$|H_m(j\omega)|^2 \to \begin{cases} \omega^2, & |\omega| < 1 \\ 1, & |\omega| \geq 1 \end{cases} \tag{3.18}$$

as required. Factoring the numerator and denominator of $|H_m(j\omega)|^2$ and eliminating a common factor of $\omega^2 - 1$ results in the equivalent representation

$$|H_m(j\omega)|^2 = \frac{\omega^{2m} + \omega^{2(m-1)} + \ldots + \omega^2}{\omega^{2m} + \omega^{2(m-1)} + \ldots + \omega^2 + 1} \tag{3.19}$$

A causal approximation H_m may be obtained as follows. If $H_m(j\omega)$ is the transfer

function of a real system, then $H_m(-j\omega)$ is the complex conjugate of $H_m(j\omega)$, and therefore

$$|H_m(j\omega)|^2 = H_m(j\omega)H_m(-j\omega) \tag{3.20}$$

In terms of the Laplace variable $s = j\omega$, define

$$M(s) = H_m(s)H_m(-s) = \frac{-s^2 + s^4 - \ldots + (-1)^m s^{2m}}{1 - s^2 + s^4 - \ldots + (-1)^m s^{2m}} \tag{3.21}$$

Because $M(s)$ is a rational function of s^2, the spectral factorization of $M(s)$ results in factors that are rational functions of s. The stable and minimum phase factor $H_m(s)$ has as poles and zeros all the open left half-plane poles and zeros of $M(s)$, plus one of the two zeros of $M(s)$ at the origin. By making the substitution $\omega^2 = -s^2$ in the numerator of Equation (3.17), it can be seen that there are two zeros at the origin, one of which belongs to $H_m(s)$, and the rest of the zeros of $H_m(s)$ are the left half-plane roots of

$$s^{2m} + 1 = 0, \quad m = 1, 3, 5, \ldots \tag{3.22}$$

$$s^{2m} - 1 = 0, \quad m = 2, 4, 6, \ldots \tag{3.23}$$

The roots of both Equations (3.22) and (3.23) are spaced at an angle of π/m rad apart around the unit circle, starting at $s = 1j$. Similarly, making the substitution $\omega^2 = -s^2$ in the denominator of Equation (3.17) shows the poles of $H_m(s)$ are the left half-plane roots of

$$s^{2(m+1)} - 1 = 0, \quad m = 1, 3, 5, \ldots \tag{3.24}$$

$$s^{2(m+1)} + 1 = 0, \quad m = 2, 4, 6, \ldots \tag{3.25}$$

For Equations (3.24) and (3.25), the roots also start at $s = 1j$, but are space at an angle of $\pi/(m+1)$ rad apart around the unit circle. Note that pole zero cancellation occurs at $s = 1j$ and $s = -1j$, thus the resulting $H_m(s)$ has m poles in a Butterworth pattern, and $m - 1$ zeros that are also in a Butterworth pattern, plus an additional zero at the origin.

The magnitude of the linear notch approximation H_m for various values of m is shown

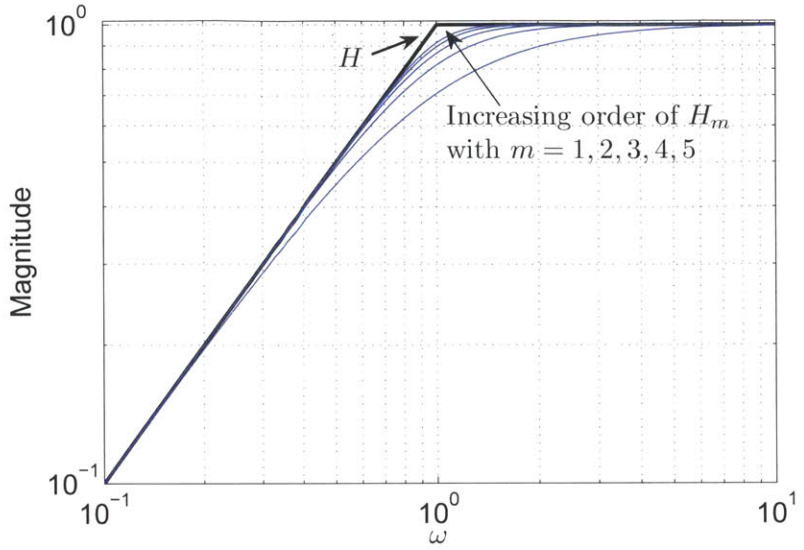

Figure 3-4: Ideal linear notch and various order of notch approximation

in Figure 3-4. As m increases, $|H_m(j\omega)|$ closely approximates the ideal linear notch. As a practical matter, we have found that increasing the filter order beyond $m = 6$ has little effect on the analysis of controller performance.

When the disturbance contains multiple harmonics n_i, $i = 1, 2, \ldots, M$, the ideal bound can be expressed in terms of the ideal linear notch as[1]

$$\mathcal{V}(\omega; \omega_B, S_{\max}) = S_{\max} \prod_{i=1}^{M} \left| H\left(\frac{j\omega - jn_i\Omega}{\omega_B S_{\max}}\right)\right| \cdot \left| H\left(\frac{j\omega + jn_i\Omega}{\omega_B S_{\max}}\right)\right| \tag{3.26}$$

The product on the right hand side of Equation (3.26) has two notches for each of the M harmonic frequencies of interest, one for frequency $\omega = n_i\Omega$, and one for frequency $\omega = -n_i\Omega$. Because the maximum magnitude of the ideal linear notch is unity, the product has a maximum magnitude of unity. The factor $S_{\max}$ is needed to make the maximum of $\mathcal{V}$ be $S_{\max}$. The notches must also be scaled by $\omega_B S_{\max}$ to achieve the appropriate bandwidth as defined by Equation (3.8). The finite-dimensional approximation of the ideal linear

[1] Note that Equation (3.26) is correct only if the individual notches do not overlap, which requires that

$$\omega_B \leq \frac{\Omega}{2S_{\max}}$$

For practical parameter values, this condition will always hold.

notch at multiple harmonic frequencies is

$$V(s) = S_{\max} \prod_{i=1}^{M} \left| H_m \left(\frac{j\omega - jn_i\Omega}{\omega_B S_{\max}} \right) \right| \cdot \left| H_m \left(\frac{j\omega + jn_i\Omega}{\omega_B S_{\max}} \right) \right| \tag{3.27}$$

Finally, we approximate the weighting filter $\mathcal{W}(\omega; \omega_B, S_{\max})$ by a finite-dimensional approximation $W(j\omega)$, with W defined by

$$W(s) = V^{-1}(s) = \left(S_{\max} \prod_{i=1}^{M} H_m \left(\frac{s - jn_i\Omega}{\omega_B S_{\max}} \right) H_m \left(\frac{s + jn_i\Omega}{\omega_B S_{\max}} \right) \right)^{-1} \tag{3.28}$$

Note that the resulting $W(s)$ has all its zeros in the open left half-plane, but has poles in the closed left half-plane, including poles on the $j\omega$-axis, because $H_m(s)$ has a zero at the origin. For any controller that satisfies the bandwidth and peak sensitivity constraints, the resulting sensitivity transfer function $S(s)$ will have zeros on the $j\omega$-axis that cancel the $j\omega$-axis poles of $W(s)$. The analysis problem is then to determine whether for the given controller $K(s)$,

$$\|T_{zd}\|_\infty = \|WS\|_\infty \leq 1 \tag{3.29}$$

where T_{zd} is the transfer function from d to z in the block diagram shown in Figure 3-5. A controller that satisfies Inequality (3.29) will also satisfy

$$\|\mathcal{W}S\|_\infty \leq 1 \tag{3.30}$$

because $|W(j\omega)| \geq |\mathcal{W}(j\omega; \omega_B, S_{\max})|$ for all ω. The conservatism introduced by using W instead of $\mathcal{W}$ can be reduced by using a high order H_m, at the expense of greater computational complexity.

3.2.2 Parabolic Notch

If a controller satisfies the inequality $\|WS\| \leq 1$, where W is the inverse of the linear notch filter of Section 3.2.1, then the closed-loop response to the harmonic disturbance will increase linearly with deviation in the frequency of the disturbance. A notch filter with a

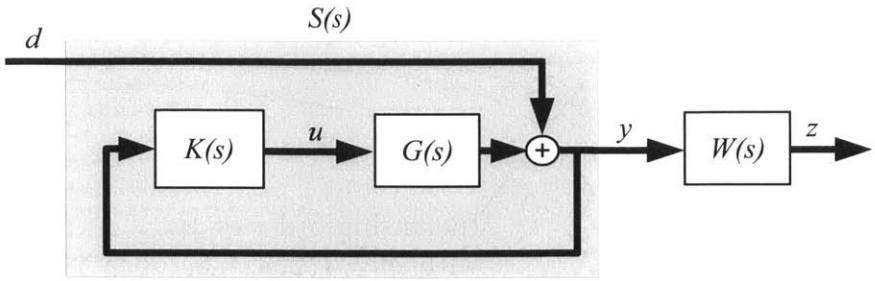

Figure 3-5: $\mathcal{H}_\infty$ performance analysis block diagram

parabolic shape near the harmonic frequency would be less sensitive to deviations in the harmonic frequency, as long as the deviation in frequency is not too large. In this section, we develop the parabolic notch filter with the bandwidth defined as the largest ω_B such that

$$|S(j\omega)| \leq \frac{1}{\omega_B^2} |\omega - n_i\Omega|^2, \quad \forall \omega \in \mathbb{R} \tag{3.31}$$

The magnitude of the ideal parabolic notch, with $\Omega = 0$ and $\omega_B = 1$ is given by

$$|H(j\omega)| = \begin{cases} \omega^2, & |\omega| < 1 \\ 1, & |\omega| \geq 1 \end{cases} \tag{3.32}$$

An approximation of the squared magnitude of the ideal parabolic notch is

$$|H_m(j\omega)|^2 = \frac{\omega^4(\omega^{2m} - 1)}{\omega^{2m+4} - 1}, \quad m = 1, 2, \ldots \tag{3.33}$$

and as in the case for the linear notch, it can be verified that as the order of approximation $m \to \infty$,

$$|H_m(j\omega)|^2 \to \begin{cases} \omega^4, & |\omega| < 1 \\ 1, & |\omega| \geq 1 \end{cases} \tag{3.34}$$

as required. By following the same procedure carried out for the linear notch filter in Section 3.2.1, the approximation of the ideal quadratic notch is obtained from the stable

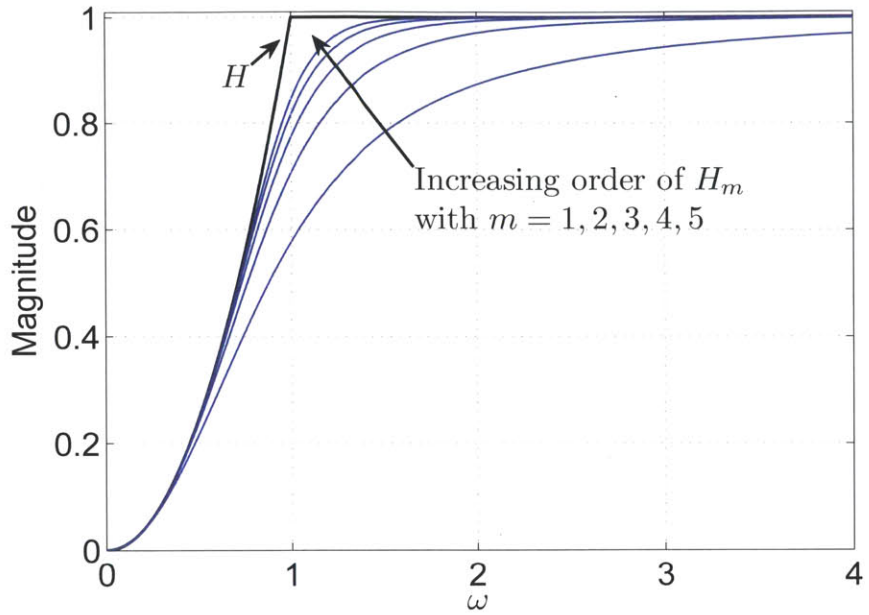

Figure 3-6: Ideal parabolic notch and various order of notch approximation

and minimum phase factor $H_m(s)$ of

$$M(s) = H_m(s)H_m(-s) = \begin{cases} \frac{s^4 - s^6 + \ldots + (-1)^{m+1} s^{2(m+1)}}{1 - s^2 + s^4 - \ldots + (-1)^{m+1} s^{2(m+1)}}, & m = 1, 3, 5, \ldots \\ \frac{s^4 + s^8 + \ldots + s^{2m}}{1 + s^4 + s^8 + \ldots + s^{2m}}, & m = 2, 4, 6, \ldots \end{cases} \tag{3.35}$$

where a common factor of $\omega^2 - 1$ is eliminated from Equation (3.33) in the case m is odd, and a common factor of $\omega^4 - 1$ is eliminated in the case m is even. Similar to the linear notch filter case, the poles of $H_m(s)$ are arranged in a Butterworth pattern, and the zeros are also arranged in a Butterworth pattern, but the parabolic case has two additional zeros at the origin. Whereas the subscript m indicates the filter order for the linear notch filter, the order of the parabolic filter depends on whether m is odd or even. For odd m, the filter has $m + 1$ poles and zeros. For even m, the number of poles and zeros are both equal to m. The approximations of the parabolic notch for various values of m are shown in linear scale in Figure 3-6.

The derivation for the ideal bound $\mathcal{V}(\omega; \omega_B, S_{\max})$ in the parabolic notch case also fol-

lows the derivation in linear notch case. The ideal bound for parabolic notch is given by

$$\mathcal{V}(\omega;\omega_B,S_{\max}) = S_{\max}\prod_{i=1}^{M}\left|H\left(\frac{j\omega - jn_i\Omega}{\omega_B\sqrt{S_{\max}}}\right)\right|\cdot\left|H\left(\frac{j\omega + jn_i\Omega}{\omega_B\sqrt{S_{\max}}}\right)\right| \tag{3.36}$$

and the resulting weighting filter is

$$W(s) = \left(S_{\max}\prod_{i=1}^{M}H_m\left(\frac{s - jn_i\Omega}{\omega_B\sqrt{S_{\max}}}\right)H_m\left(\frac{s + jn_i\Omega}{\omega_B\sqrt{S_{\max}}}\right)\right)^{-1} \tag{3.37}$$

In this case, the argument is scaled by $1/(\omega_B\sqrt{S_{\max}})$ instead of $1/(\omega_B S_{\max})$ in the linear notch. Since $H_m(s)$ has two zeros at the origin, $W(s)$ has two poles at $\omega = n_i\Omega$ and two poles at $\omega = -n_i\Omega$. Thus, any controller that satisfies

$$\|WS\|_\infty \leq 1 \tag{3.38}$$

where $W(s)$ is the weighting filter of the parabolic notch given in Equation 3.37, must have two poles at $\omega = n_i\Omega$, and two poles at $\omega = -n_i\Omega$, in order to generate the necessary zeros in $S(s)$ to cancel the $j\omega$-axis poles of $W(s)$.

While the notch could be made even flatter in the vicinity of the harmonic frequencies by including more zeros at the origin in the notch filter, a strong argument against using more than two zeros at the origin can be made by considering the root locus of such a system. In order for the sensitivity transfer function to have k zeros at the origin, the controller and plant combined must have k poles at the origin. While it is possible to direct the two branches of the root loci at the origin to the left-half plane with the correct phase adjustment, this is not possible when there are more than two poles at the origin. At least one branch of the resulting root loci will initially venture into the right-half plane, resulting in a conditionally stable closed-loop system. Since a decrease in the static gain could cause the conditionally stable system to destabilize, it would in general not be practical to go beyond a parabolic notch filter.

3.3 $\mathcal{H}_\infty$ Controller Synthesis

The analysis framework presented above can be used to develop an $\mathcal{H}_\infty$ controller synthesis methodology, albeit with some complication for the cases with complete harmonic disturbance rejection. In theses cases, because $W(s)$ has poles on the $j\omega$-axis, any controller for which $\|WS\|_\infty$ is finite will result in system zeros in $S(s)$ on the $j\omega$-axis that cancel the $j\omega$-axis poles in $W(s)$, as discussed above. However, the usual $\mathcal{H}_\infty$ synthesis procedure will fail, because the poles of $W(s)$ on the $j\omega$-axis are both unstable and unobservable.

The problem is similar to that encountered when an integral weighting filter is used to ensure rejection of constant disturbances, as discussed by Zhou and Doyle [112]. One way to remedy this problem is to factor $W(s)$ into two not strictly proper transfer functions as

$$W(s) = W_2(s)W_1(s) \tag{3.39}$$

such that $W_1(s)$ contains all the poles of $W(s)$ on the $j\omega$-axis, and $W_2(s)$ contains the rest of the poles of $W(s)$ and is minimum phase. The control synthesis is performed as if the plant were $W_1(s)G(s)$, and the weighting were $W_2(s)$, which results in a controller $\widehat{K}_\infty(s)$ that acts on the augmented plant $W_1(s)G(s)$. The controller acting on the plant $G(s)$ is then

$$K_\infty(s) = \widehat{K}_\infty(s)W_1(s) \tag{3.40}$$

The inclusion of $W_1(s)$ in the $\mathcal{H}_\infty$ controller as shown in Equation (3.40) implies the controller contains poles on the $j\omega$-axis at the harmonic frequencies. The controller thus generates infinite gain at these harmonic frequencies, which is necessary for the complete rejection of the harmonic disturbances. The block diagram for the modified controller synthesis problem is shown in Figure 3-7.

3.3.1 Augmented Plant and $\mathcal{H}_\infty$ Higher Harmonic Control

Another way to remedy the problem of the unstable and unobservable poles on the $j\omega$-axis in the weighting filter is presented in this section using a state-space formulation. The main difference is that the decomposition of the weighting filter in Equation (3.39) is in series,

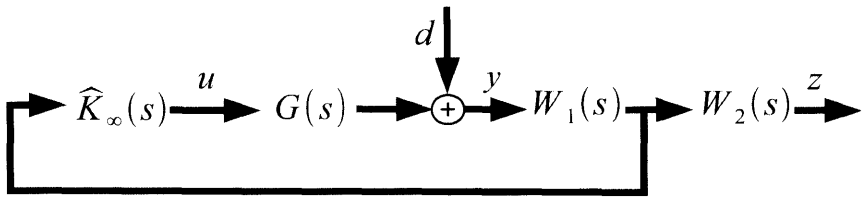

Figure 3-7: $\mathcal{H}_\infty$ control synthesis setup when weighting filter contains poles on $j\omega$-axis

while a parallel decomposition is used in this section.

We first partition the state-space realization of the weighting filter

$$W(s) \sim \left(\begin{array}{c|c} A_W & B_W \\ \hline C_W & D_W \end{array}\right) \tag{3.41}$$

into

$$A_W = \begin{bmatrix} A_1 & 0 \\ 0 & A_2 \end{bmatrix} \tag{3.42}$$

$$B_W = \begin{bmatrix} B_1 \\ B_2 \end{bmatrix} \tag{3.43}$$

$$C_W = \begin{bmatrix} C_1 & C_2 \end{bmatrix} \tag{3.44}$$

where the eigenvalues of A_1 are all the poles of $W(s)$ that are on the $j\omega$-axis, and the eigenvalues of A_2 are the remaining poles of $W(s)$ that are not on the $j\omega$-axis. The restriction that A_W be block diagonal can be easily accomplished by realizing $W(s)$ in modal form, or Jordan form if $W(s)$ has repeated poles.

The augmented plant for $\mathcal{H}_\infty$ controller synthesis in terms of the decomposed weighting

filter is

$$\begin{bmatrix} \dot{x}_p \\ \dot{x}_1 \\ \dot{x}_2 \end{bmatrix} = \begin{bmatrix} A_p & 0 & 0 \\ B_1 C_p & A_1 & 0 \\ B_2 C_p & 0 & A_2 \end{bmatrix} \begin{bmatrix} x_p \\ x_1 \\ x_2 \end{bmatrix} + \begin{bmatrix} 0 & B_p \\ B_1 & 0 \\ B_2 & 0 \end{bmatrix} \begin{bmatrix} d \\ u \end{bmatrix} \tag{3.45}$$

$$\begin{bmatrix} z_1 \\ z_2 \end{bmatrix} = \begin{bmatrix} D_W C_p & C_1 & C_2 \\ 0 & I & 0 \end{bmatrix} \begin{bmatrix} x_p \\ x_1 \\ x_2 \end{bmatrix} + \begin{bmatrix} D_W & 0 \\ 0 & 0 \end{bmatrix} \begin{bmatrix} d \\ u \end{bmatrix} \tag{3.46}$$

It is also possible to include a weighting on the control effort. For example, a constant scalar weighting W_u on control effort could be incorporated in the augmented plant by appending Equation (3.46) with

$$z_3 = \begin{bmatrix} 0 & 0 & 0 \end{bmatrix} \begin{bmatrix} x_p \\ x_1 \\ x_2 \end{bmatrix} + \begin{bmatrix} 0 & W_u \end{bmatrix} \begin{bmatrix} d \\ u \end{bmatrix} \tag{3.47}$$

Applying the $\mathcal{H}_\infty$ synthesis procedure to the augmented plant of Equations (3.45) and (3.46) results in an $\mathcal{H}_\infty$ controller $\widehat{K}_\infty(s)$ with the state-space realization

$$\widehat{K}_\infty(s) \sim \left(\begin{array}{c|c} A_{\widehat{K}} & B_{\widehat{K}} \\ \hline C_{\widehat{K}} & D_{\widehat{K}} \end{array} \right) \tag{3.48}$$

The block diagram of the $\mathcal{H}_\infty$ controller synthesis setup is shown in Figure 3-8, where

$$\widehat{W}_1(s) \sim \left(\begin{array}{c|c} A_1 & B_2 \\ \hline I & 0 \end{array} \right) \tag{3.49}$$

$$\widehat{W}_2(s) \sim \left(\begin{array}{c|c} A_2 & B_2 \\ \hline C_2 & D_W \end{array} \right) \tag{3.50}$$

The controller $\widehat{K}_\infty(s)$ is combined with the harmonic part of the weighting filter $\widehat{W}_1(s)$ to

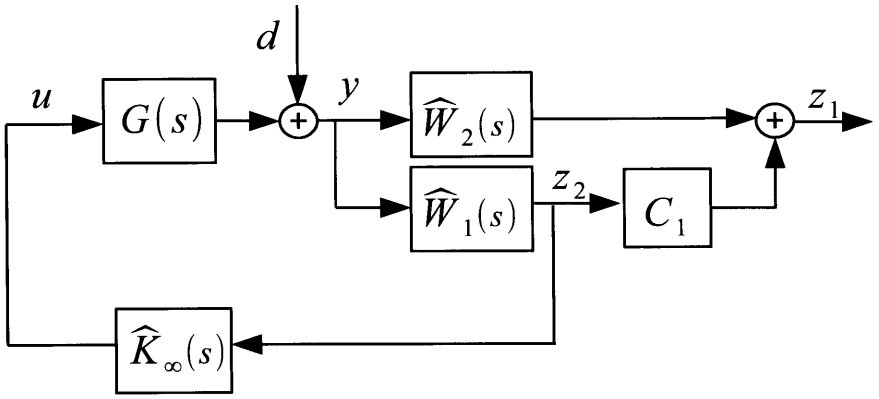

Figure 3-8: Block diagram of augmented plant in $\mathcal{H}_\infty$ controller synthesis

form the $\mathcal{H}_\infty$ higher harmonic controller $K_\infty(s)$ with the state-space representation

$$K_\infty(s) \sim \left(\begin{array}{c|c} \begin{bmatrix} A_1 & 0 \\ B_{\widehat{K}} & A_{\widehat{K}} \end{bmatrix} & \begin{bmatrix} B_1 \\ 0 \end{bmatrix} \\ \hline \begin{bmatrix} D_{\widehat{K}} & C_{\widehat{K}} \end{bmatrix} & 0 \end{array} \right) \tag{3.51}$$

The order of the $\mathcal{H}_\infty$ higher harmonic controller $K_\infty(s)$ is

$$n_c = n_p + n_W + n_{W_1} \tag{3.52}$$

where n_p is the order of the plant, n_W is order of the weighting filter $W(s)$, and n_{W_1} is the order of $\widehat{W}_1(s)$.

3.4 $\mathcal{H}_\infty$ HHC Performance

In this section, the performance of the $\mathcal{H}_\infty$ controllers designed using the different notch shapes is examined using an LTI model of the helicopter rotor. The model is derived from wind tunnel test data at Flight Condition 1, the output is the rotor hub normal force, and the input is the collective voltage to the rotor on-blade actuators. The parameters for Flight Condition 1 are shown in Table 3.1. Details of the model and the system identification process used to obtain them are described in Chapter 5. The plant model is of order $n_p = 19$. All controllers examined below are designed to eliminate the disturbances at the first

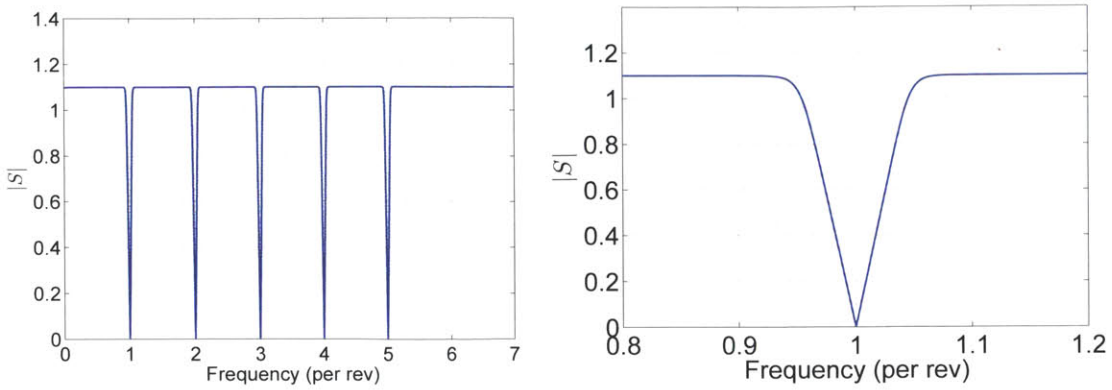

(a) Sensitivity transfer function

(b) Close-up view at the first harmonic frequency

Figure 3-9: Sensitivity transfer function with linear notch

five harmonics, *i.e.*, $n_i = i$, $i = 1, 2, 3, 4, 5$. Because there are five harmonic frequencies in the disturbance to be rejected, the weighting filter $W(s)$ has order $n_W = 2mM = 10m$, where m is the order of the weighting filter, and $M = 5$ is the number of harmonic frequencies to be rejected. The order of $\widehat{W_1}(s)$ is $n_{W_1} = 2M = 10$ for the linear notch filter, and $n_{W_1} = 4M = 20$ for the parabolic notch filter. The resulting $\mathcal{H}_\infty$ higher harmonic controller is of order $N_c = n_p + 10m + 2M = 29 + 10m$ for the linear notch case, and $N_c = n_p + 10m + 4M = 39 + 10m$ for the parabolic notch case.

3.4.1 Linear Notch Performance

The magnitude of a sensitivity transfer function with linear notch is shown in Figure 3-9. The $\mathcal{H}_\infty$ controller was generated using weighting filters of order $m = 6$, and the peak sensitivity is selected to be $S_{\max} = 1.1$, resulting in a bandwidth $\omega_B = 0.043$ per rev. The magnitude of the sensitivity functions matches the shape specified by the weighting filter to the specified tolerance used in the $\mathcal{H}_\infty$ synthesis procedure. Figure 3-9b shows the detail of the notch shapes at the first harmonic.

A Pareto frontier in terms of peak sensitivity $S_{\max}$ and bandwidth ω_B can be established using the $\mathcal{H}_\infty$ method for harmonic disturbance rejection. This is because the $\mathcal{H}_\infty$ method will generate a controller that makes the magnitude of the sensitivity transfer function arbitrarily close to the finite dimensional notch approximation, and the finite dimensional notch approximation approaches the ideal notch shape as the filter approximation order $m \to \infty$.

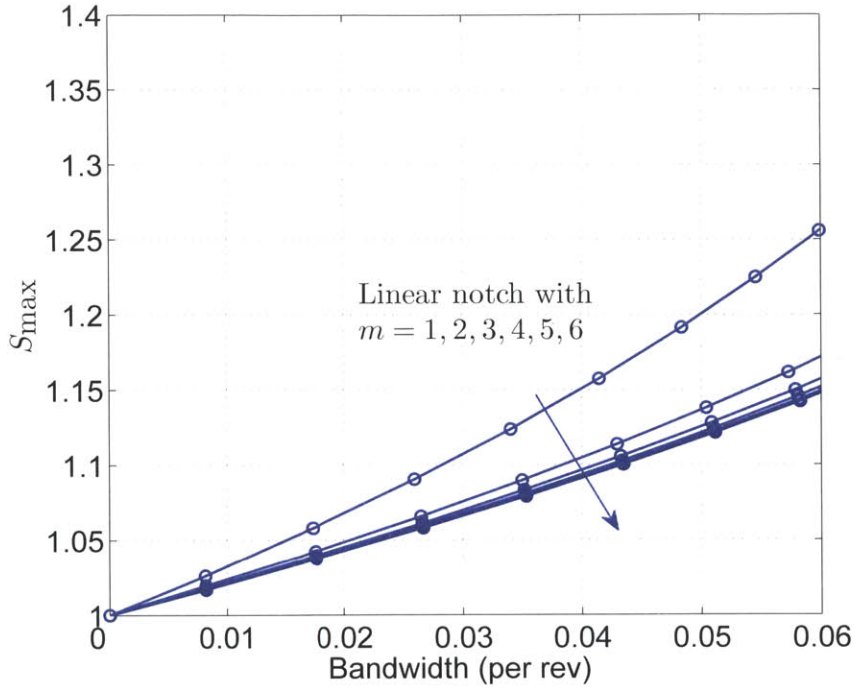

Figure 3-10: Pareto frontier of peak sensitivity and bandwidth for linear notch

The Pareto frontiers are shown in Figure 3-10, where each individual curve represents the achievable performance within a family of controllers of the same order. Because the performance is better with either larger bandwidth or smaller peak sensitivity, improvement in performance is indicated by a movement of the curve down and to the right. For the $\mathcal{H}_\infty$ method, little improvement is obtained beyond $m = 6$, thus the curves corresponding to $m = 6$ is a good representation of the achievable Pareto frontier for continuous-time higher harmonic control performance.

3.4.2 Parabolic Notch Performance

Similar to the linear notch case above, the $\mathcal{H}_\infty$ controller for parabolic notch was generated using weighting filters of order $m = 6$, and the peak sensitivity is selected to be $S_{\max} = 1.1$, resulting in $\omega_B = 0.023$ per rev. The sensitivity function is shown in Figure 3-11.

Pareto frontiers in terms of peak sensitivity $S_{\max}$ and bandwidth ω_B can also be established for the parabolic notch case, as shown in Figure 3-12. Note that the bandwidth ω_B is defined differently for the parabolic notch, thus the Pareto frontiers are not directly

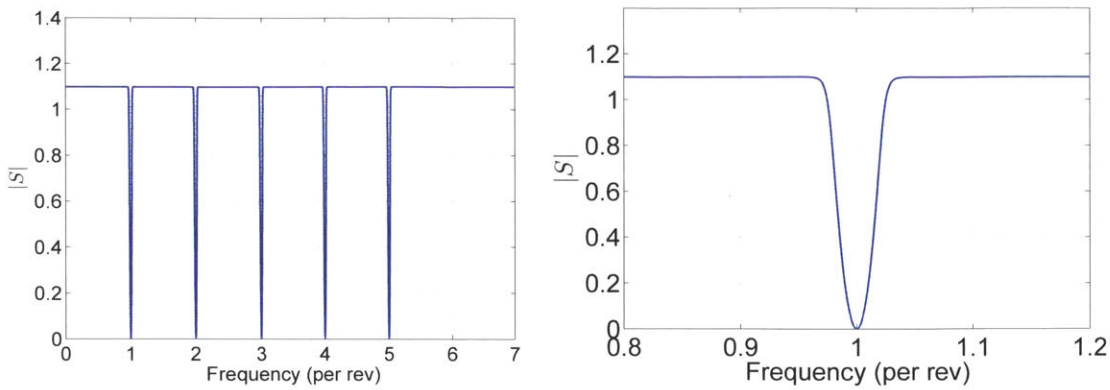

(a) Sensitivity transfer function

(b) Close-up view at the first harmonic frequency

Figure 3-11: Sensitivity transfer function with parabolic notch

comparable to the linear notch case.

3.4.3 Transient Response

The bandwidth and peak sensitivity are metrics that we can address directly in the design of controllers. While we defined the performance metrics with the transient performance in mind, it is important to verify the transient behavior of the closed-loop system through simulation.

For the transient performance, we look at the settling time of the closed-loop system to a harmonic disturbance

$$d(t) = \begin{cases} 0, & t < 0 \\ A\sin(n\Omega t + \tau), & t \geq 0 \end{cases} \tag{3.53}$$

where the independent variable t represents the azimuthal position of the rotor, A is the amplitude of the harmonic disturbance, and τ is the phase of the harmonic disturbance. For $A = 1$, $n = 1$, $\tau = 0$, the responses produced by the closed-loop system with the different controllers are shown in Figure 3-13. While the larger bandwidth value of the linear notch case implies a shorter settling time than the parabolic notch case by approximately a factor of 2, the settling time to -20 dB for the linear notch case is actually shorter by a factor of nearly 4 (7.81 rev for the linear notch case, 26.77 rev for the parabolic notch case). The

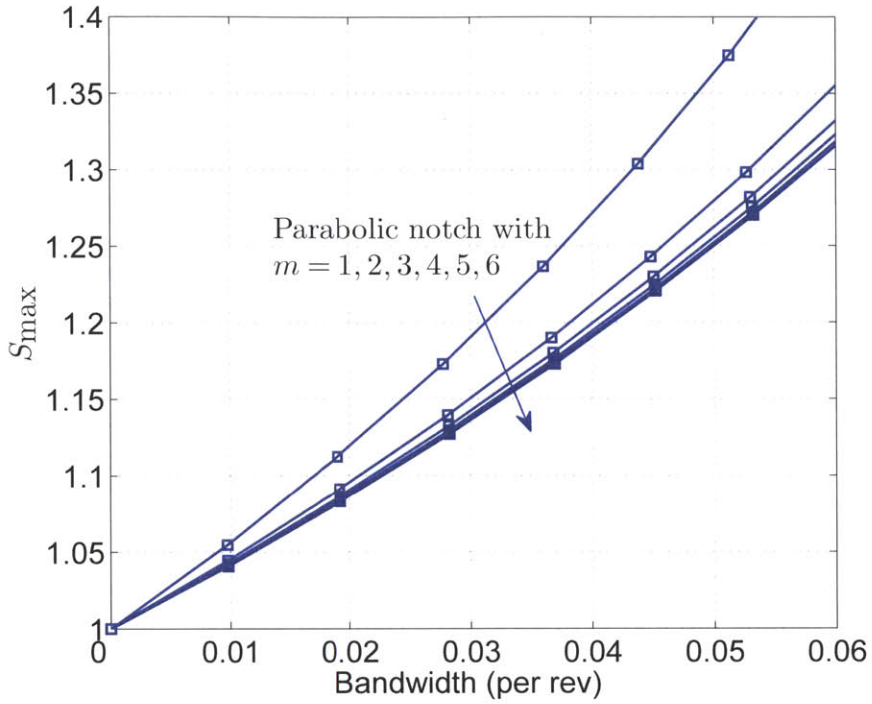

Figure 3-12: Pareto frontier of peak sensitivity and bandwidth for parabolic notch

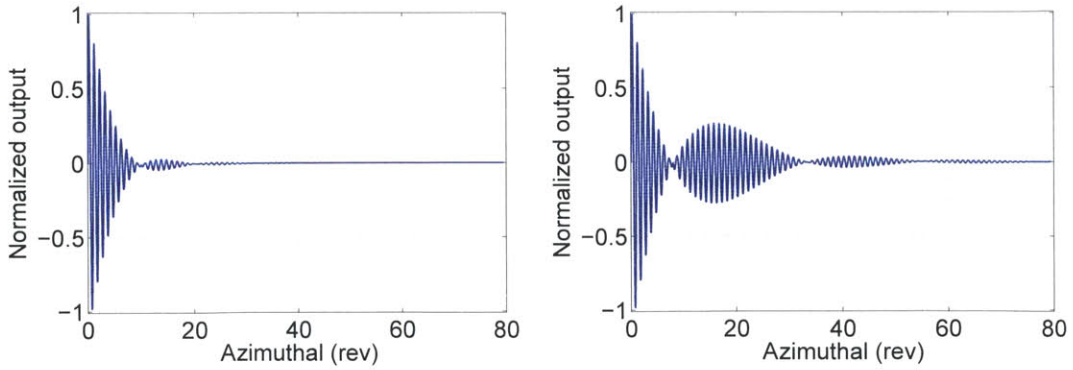

(a) Linear notch case

(b) Parabolic notch case

Figure 3-13: Normalized response of the closed-loop system to a harmonic disturbance

discrepancy in the ratio of settling time and ratio of bandwidth can be attributed to the difference in the shape of the notch in the sensitivity function. Since the controllers for this comparison have the same value of $S_{\max}$, the only way for the parabolic notch controller to approach the transient performance of the linear notch controller is to relax $S_{\max}$, which will lead to increased broadband vibration level, and reduced gain and phase margins.

3.4.4 RMS Performance

The parameters A, τ, and Ω of the disturbance in Equation (3.53) may vary during helicopter operation, even at constant flight condition. The changes in A, τ, and Ω may be stochastic in nature, for example, they could be caused by wind gust, which will change the power spectral density of the disturbance from an impulse to one with finite width.

In order to examine the RMS performance, Hall and Wereley [44] suggested modeling the narrow band disturbance using a Gauss-Markov process with the autocorrelation function

$$R_{dd}(t) = \sigma_d^2 \exp\left\{-\frac{|t|}{\tau}\right\} \cos(\omega_0 t) \tag{3.54}$$

where σ_d is the standard deviation of the disturbance, τ is the correlation time of the Gauss-Markov disturbance, and ω_0 is the central frequency of the disturbance. The power spectral density of the narrow band disturbance is

$$S_{dd}(s) = F(j\omega)F(-j\omega)S_w(j\omega)$$

where $S_{dd}(s)$ is the power spectral density of the disturbance, $S_w(s)$ is the power spectral density of the Gaussian white noise with intensity σ_d^2 , and F is the shaping filter is given by

$$F(s) = \sqrt{\frac{2}{\tau}} \frac{s + \sqrt{\frac{1}{\tau^2} + \omega_0^2}}{s^2 + \frac{2}{\tau}s + \frac{1}{\tau^2} + \omega_0^2} \tag{3.55}$$

The RMS vibration level of the closed-loop system can be obtained by computing

$$\frac{\sigma_z}{\sigma_d} = \|S(s)F(s)\|_2 \tag{3.56}$$

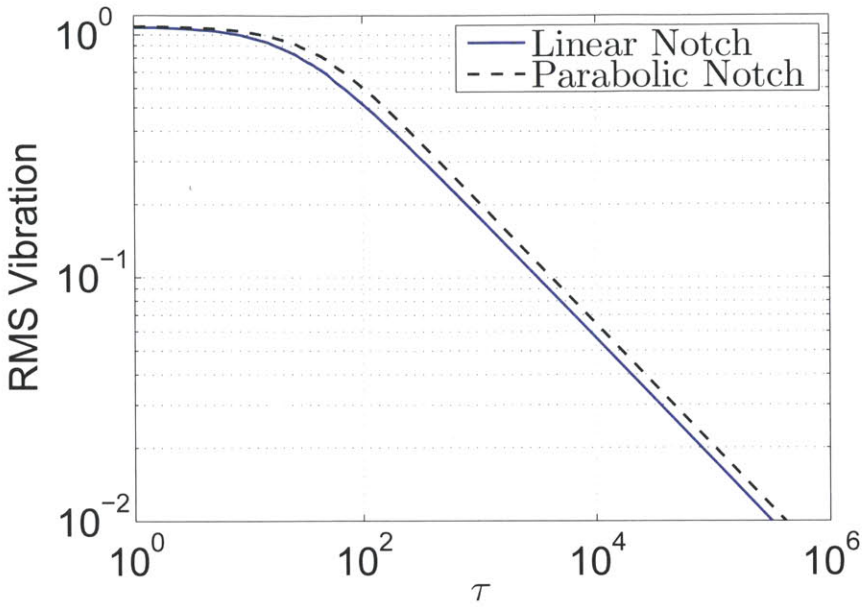

Figure 3-14: RMS vibration level for $\omega_0 = \Omega$

Again, we consider the two controllers with $S_{\max} = 1.1$, but different notch shapes. The RMS vibration level as a function of correlation time τ for $\omega_0 = \Omega$ is plotted in Figure 3-14, which shows that the linear notch has lower RMS vibration level for all values of τ. The RMS vibration level as a function of τ for $\omega_0 = 1.01\Omega$ is plotted in Figure 3-15, in this case, the linear notch case has lower vibration level for small values of τ, while the parabolic notch case has lower vibration level for larger values of τ. Although the RMS vibration level is an important aspect of controller design, the utility of the RMS analysis is dependent on the nature of the disturbance. Unfortunately, the knowledge about the random characteristics of the disturbance on the rotor is currently lacking, more data or better modeling is required to make the RMS vibration analysis a useful tool for design purpose.

3.5 Summary

In this chapter, we showed that the performance in harmonic disturbance rejection can be quantified by the bandwidth ω_B and the peak sensitivity $S_{\max}$. The bandwidth ω_B and peak sensitivity $S_{\max}$ are defined relative to the shape of the ideal notch. We presented two types

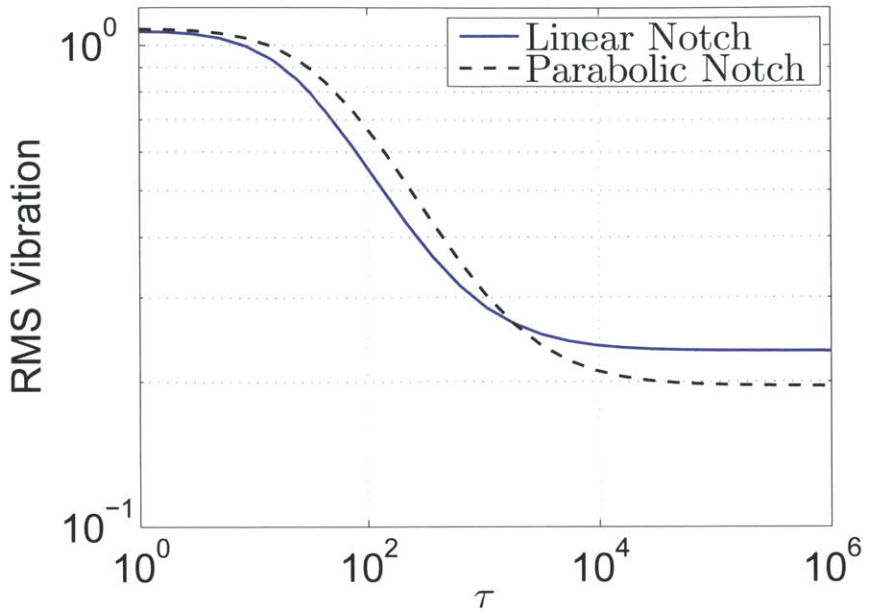

Figure 3-15: RMS vibration level for $\omega_0 = 1.01\Omega$

of notch filters: the linear notch filter and the quadratic notch filter. The notch filters are approximations of the ideal notch shape, and when inverted, are used as the weighting filter $W(s)$ in the $\mathcal{H}_\infty$ frame work for analysis and synthesis. Based on the transient performance of the controllers, the linear notch shape is a better metric than the parabolic notch. Furthermore, controllers designed using high order $W(s)$ provide the achievable performance in terms of ω_B and $S_{\max}$. However, it is important to note that in many cases, the $\mathcal{H}_\infty$ controllers are unstable, although the closed-loop system is stable. Unstable controllers are unacceptable for higher harmonic control systems in practice, because if the actuators ever saturate, the system effectively operates in open-loop, and the control system will be destabilized.

Chapter 4

Fixed-Order $\mathcal{H}_\infty$ Controller Synthesis

One difficulty with the full-order $\mathcal{H}_\infty$ higher harmonic control (HHC) approach outlined in the previous chapter is that the resulting controller order can be quite high. The order of the $\mathcal{H}_\infty$ controller is the order of the plant plus the order of the weighting filter. For example, the order of the linear weighting filter is $2mM$, where m is the order of the notch approximation, and M is the number of harmonics to be suppressed. In the HHC problem, it would not be unusual to have $M = 5$, and we have found that we need up to $m = 6$ to adequately approximate the notch. The order of the helicopter plant model is at least twice the number of significant rotor modes within the bandwidth of interest, and so can easily be 10 to 15. Thus, a typical weighting filter would be of order 60 or higher, leading to controllers of order 70 or more. Another difficulty with the full-order $\mathcal{H}_\infty$ HHC approach is that the controller itself may not be stable. An unstable controller is problematic because if the actuator becomes saturated, the closed-loop system effectively operates in open-loop with an unstable element, causing the entire system to become unstable.

In this chapter, we describe a methodology for obtaining stable fixed-order controllers that optimize the $\mathcal{H}_\infty$ performance objective for harmonic disturbance rejection. The aim of the fixed-order $\mathcal{H}_\infty$ controller is to strike a balance between controller complexity and performance, while ensuring the controller itself does not cause instability in the event of actuator saturation.

4.1 Fixed-Order Controller Synthesis Parameterization

In this section, we develop the fixed-order $\mathcal{H}_\infty$ controller by using the linear notch filter $V(s)$ developed in Chapter 3 as the performance measure. The bandwidth ω_B and peak sensitivity $S_{\max}$ associated with $V(s)$ are the metrics used to quantify the performance of the controller, while the inverse of the linear notch filter $W(s) = V^{-1}(s)$ is used in the synthesis procedure as the weighting filter. As in the previous chapter, we consider the plant with the state-space representation

$$\dot{x}_p(t) = A_p x(t) + B_p u(t) \tag{4.1}$$

$$y_p(t) = C_p x(t) \tag{4.2}$$

$$y(t) = C_p x(t) + d(t) \tag{4.3}$$

in the development of the fixed-order $\mathcal{H}_\infty$ controller for harmonic disturbance rejection. The transfer function from $u(t)$ to $y_p(t)$ is

$$G(s) = C_p(sI - A_p)^{-1}B_p \tag{4.4}$$

The sensitivity transfer function $S(s)$, which is the closed-loop transfer function from d(t) to $y(t)$ is

$$S(s) = (I - G(s)K(s))^{-1} \tag{4.5}$$

where $K(s)$ is the transfer function of the output feedback controller.

4.1.1 $\mathcal{H}_\infty$ Cost Function

In the $\mathcal{H}_\infty$ framework, the specified closed-loop performance is quantified by a weighting filter $W(s)$. The weighted sensitivity function is formed by connecting the weighting filter $W(s)$ in series with the sensitivity transfer function as shown in Figure 4-1. The weighted sensitivity function is the closed-loop transfer function from $d(t)$ to the performance variable $z(t)$, and is denoted by

$$T_{zd}(s) = W(s)S(s) \tag{4.6}$$

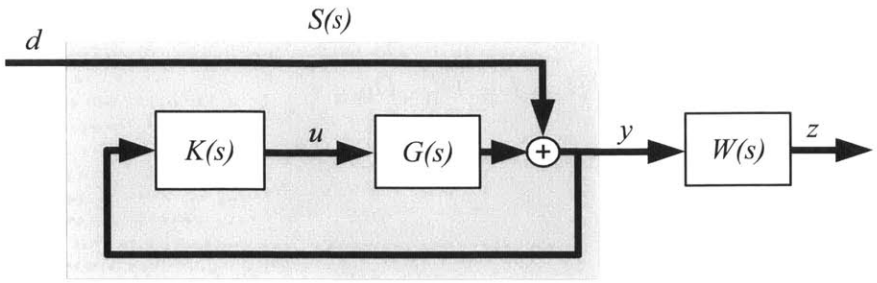

Figure 4-1: $\mathcal{H}_\infty$ performance analysis block diagram

The $\mathcal{H}_\infty$ analysis problem for a given stabilizing controller is to check whether

$$\|T_{zd}\|_\infty < 1$$

Since the infinity norm can be efficiently computed using state-space methods [25], we proceed with the state-space realization

$$T_{zd}(s) \sim \left(\begin{array}{c|c} A_{WS} & B_{WS} \\ \hline C_{WS} & D_{WS} \end{array}\right) \tag{4.7}$$

for the weighted sensitivity function

The necessary conditions [112] for $\|T_{zd}\|_\infty < 1$ are that

$$|D_{WS}| < 1 \tag{4.8}$$

and that the algebraic Riccati equation

$$\bar{A}Q + Q\bar{A}^T + \bar{B}\bar{B}^T + Q\bar{C}^T\bar{C}Q = 0 \tag{4.9}$$

has a symmetric, positive definite solution Q, where

$$\bar{A} = A_{WS} + B_{WS}R^{-1}D_{WS}^T C_{WS} \tag{4.10}$$

$$\bar{B} = B_{WS}R^{-\frac{1}{2}} \tag{4.11}$$

$$\bar{C} = (I + D_{WS}R^{-1}D_{WS}^T)^{\frac{1}{2}} C_{WS} \tag{4.12}$$

and

$$R = I - D_{WS}^T D_{WS} \tag{4.13}$$

Both Inequality (4.8) and the existence of a symmetric, positive definite solution to Equation are essentially binary conditions, not suitable for gradient based optimization methods. In order to obtain a continuous cost function that may be optimized via gradient methods, we define (following Mustafa [75]) the auxiliary cost J_a as the negative of the entropy of $T_{zd}(s)$, given by

$$J_a = \text{trace}\left[\bar{C}Q\bar{C}^T\right]$$

where Q is the positive definite, symmetric solution of Equation (4.9). This entropy cost approaches infinity as $\|T_{zd}\|_\infty$ approaches unity, so minimizing the entropy cost tends to make $\|T_{zd}\|_\infty$ smaller. The cost function J is the auxiliary cost, augmented via a Lagrange multiplier P with the constraint imposed by Equation (4.9), so that the performance index is

$$J = \text{trace}\left[\bar{C}Q\bar{C}^T + P\left(\bar{A}Q + Q\bar{A}^T + \bar{B}\bar{B}^T + Q\bar{C}^T\bar{C}Q\right)\right] \tag{4.14}$$

The performance index J is a function of $\bar{A}$, $\bar{B}$, and $\bar{C}$, which are constructed using the state-space realization of the weighted sensitivity function

$$W(s)S(s) = W(s)(I - G(s)K(s))^{-1} \tag{4.15}$$

Thus, the fixed-order $\mathcal{H}_\infty$ synthesis problem can be formulated as the optimization problem

$$\min_K J(K) \tag{4.16}$$

In the next section, we present the parameterization of the state-space realization of the controller K, which enables the optimization problem posed in Expression (4.16) to be solved.

4.1.2 Fixed-Order Controller Parameterization

As in the case of the full-order $\mathcal{H}_\infty$ synthesis with linear notch filter, we want to achieve complete disturbance rejection at the harmonic frequencies $n_i\Omega,\ i = 1, 2, \ldots, M$. In order to have complete harmonic disturbance rejection, we impose that the controller must have poles at the harmonic frequencies to be attenuated. The poles of the weighting filter $W(s)$ on the $j\omega$-axis are to be retained in the fixed-order controller by a decomposition as shown in Figure 4-2. The weighting filter is represented as

$$W(s) = C_W \begin{bmatrix} W_1(s) \\ W_2(s) \end{bmatrix} + D_W \tag{4.17}$$

where $W_1(s)$ is a $2M \times 1$ transfer function matrix, with poles on the $j\omega$-axis at each of the harmonic frequencies, $W_2(s)$ is a $2(m-1)M \times 1$ transfer function matrix, C_W is a $1 \times 2mM$ matrix, and D_W is a scalar.

The fixed-order controller $K(s)$ is given by

$$K(s) = kW_1(s) + K_c(s) \tag{4.18}$$

where

$$k = \begin{bmatrix} k_1 & k_2 & \ldots & k_{2M} \end{bmatrix} \tag{4.19}$$

and $K_c(s)$ is a scalar transfer function, with fixed order n_c that can be varied as a design parameter. As a result, the order of the controller $K(s)$ is

$$N_c = n_c + 2M \tag{4.20}$$

The decomposition of the weighting filter in Equation (4.17) ensures that the $\mathcal{H}_\infty$ cost can be calculated using state-space methods, and that there is an appropriate representation for the fixed-order controller $K(s)$, which must have poles on the $j\omega$-axis for complete harmonic disturbance rejection.

The transfer functions described above are realized as follows. The weighting filter

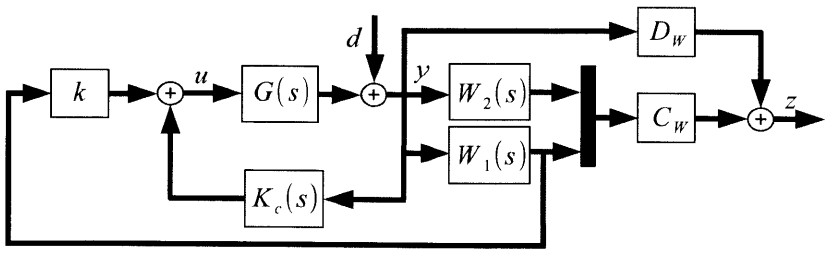

Figure 4-2: Fixed-order $\mathcal{H}_\infty$ controller setup

$W(s)$ is realized in modal form as

$$W(s) \sim \left(\begin{array}{c|c} A_W & B_W \\ \hline C_W & D_W \end{array}\right) \tag{4.21}$$

where A_W and B_W have the following partitions

$$A_W = \begin{bmatrix} A_1 & 0 \\ 0 & A_2 \end{bmatrix} \tag{4.22}$$

$$B_W = \begin{bmatrix} B_1 \\ B_2 \end{bmatrix} \tag{4.23}$$

The matrix A_1 is real, block-diagonal, and contains all the poles of $W(s)$ on the $j\omega$-axis, it has the form

$$A_1 = \begin{bmatrix} \begin{bmatrix} 0 & n_1\Omega \\ -n_1\Omega & 0 \end{bmatrix} & & & \\ & \begin{bmatrix} 0 & n_2\Omega \\ -n_2\Omega & 0 \end{bmatrix} & & \\ & & \ddots & \\ & & & \begin{bmatrix} 0 & n_M\Omega \\ -n_M\Omega & 0 \end{bmatrix} \end{bmatrix} \tag{4.24}$$

The matrix A_2 is also real and block-diagonal, but may contain first and second order blocks

so that its eigenvalues are the poles of $W(s)$ not on the $j\omega$-axis. The matrix B_1 is

$$B_1 = \begin{bmatrix} 1 & 0 & 1 & 0 & \dots & 1 & 0 \end{bmatrix}^T \tag{4.25}$$

and B_2 is also a matrix of ones and zeros, so that the system is completely controllable. The matrices C_W and D_W are chosen so that the open-loop transfer function from d to z is the desired weighting filter $W(s)$. The transfer functions $W_1(s)$ and $W_2(s)$ then have the state-space realizations

$$W_1(s) \sim \left(\begin{array}{c|c} A_1 & B_1 \\ \hline I_{2M} & 0_{2M\times 1} \end{array}\right) \tag{4.26}$$

$$W_2(s) \sim \left(\begin{array}{c|c} A_2 & B_2 \\ \hline I_{2M(m-1)} & 0_{2M(m-1)\times 1} \end{array}\right) \tag{4.27}$$

The transfer function $K_c(s)$ has the state-space realization

$$K_c(s) \sim \left(\begin{array}{c|c} A_c & B_c \\ \hline C_c & 0 \end{array}\right) \tag{4.28}$$

In order to reduce the number of free parameters in the optimization, we place some constraints on the realization of $K_c(s)$. In particular, we parameterize the controller state-space matrices as

$$A_c = \begin{bmatrix} a_1 & a_{n_c+1} & 0 & \cdots & 0 \\ -a_{n_c+1} & a_2 & a_{n_c+2} & \ddots & \vdots \\ 0 & -a_{n_c+2} & \ddots & \ddots & 0 \\ \vdots & \ddots & \ddots & a_{n_c-1} & a_{2n_c-1} \\ 0 & \cdots & 0 & -a_{2n_c-1} & a_{n_c} \end{bmatrix} \tag{4.29}$$

$$B_c = \begin{bmatrix} b_1 & b_2 & \cdots & b_{n_c} \end{bmatrix}^T \tag{4.30}$$

$$C_c = \begin{bmatrix} 1 & \cdots & 1 \end{bmatrix} \tag{4.31}$$

This parameterization of $K_c(s)$ allows for the representation of any proper transfer function

of order n_c, with only a few more free parameters than in canonical realizations that are numerically more sensitive, such as phase variable canonical form. In addition, the form of A_c allows one to easily add a constraint requiring that $K_c(s)$ be stable, because a sufficient (but not necessary) condition for stability of A_c is that its diagonal elements are all negative. For practical higher harmonic control implementations, $K_c(s)$ must be stable to ensure that the control system remains stable in the event of actuator saturation. For the result presented in this thesis, we always constrain the fixed-order controller to have poles in the closed left half-plane in order to obtain a stable controller.

The controller $K(s)$ as given in Equation (4.18) has the state-space realization

$$K(s) \sim \left(\begin{array}{c|c} A_K & B_K \\ \hline C_K & 0 \end{array}\right) \tag{4.32}$$

where

$$A_K = \begin{bmatrix} A_c & 0_{n_c \times 2M} \\ 0_{2M \times n_c} & A_1 \end{bmatrix} \tag{4.33}$$

$$B_K = \begin{bmatrix} B_c \\ B_1 \end{bmatrix} \tag{4.34}$$

$$C_K = \begin{bmatrix} C_c & k \end{bmatrix} \tag{4.35}$$

The unknown parameters of the fixed-order controller $K(s)$ are combined into a single vector as

$$\Theta = \begin{bmatrix} \theta_1 & \theta_2 & \dots & \theta_{3n_c+2M-1} \end{bmatrix}^T \tag{4.36}$$

$$= \begin{bmatrix} a_1 \dots a_{n_c} & a_{n_c+1} \dots a_{2n_c-1} & b_1 \dots b_{n_c} & k_1 \dots k_{2M} \end{bmatrix}^T \tag{4.37}$$

The fixed-order control synthesis problem is to find $\Theta \in \mathbb{R}^{3n_c+2M-1}$ to achieve the desired performance in terms of bandwidth and peak sensitivity.

Finally, the state-space realization of the weighted sensitivity function $T_{zd}(s)$ for the

fixed-order setup is

$$T_{zd}(s) \sim \left(\begin{array}{c|c} A_{WS} & B_{WS} \\ \hline C_{WS} & D_{WS} \end{array} \right) \tag{4.38}$$

where

$$A_{WS} = \begin{bmatrix} A_p & B_pC_c & B_pk & 0 \\ B_cC_p & A_c & 0 & 0 \\ B_1C_p & 0 & A_1 & 0 \\ B_2C_p & 0 & 0 & A_2 \end{bmatrix} \tag{4.39}$$

$$B_{WS} = \begin{bmatrix} 0 \\ B_c \\ B_1 \\ B_2 \end{bmatrix} \tag{4.40}$$

$$C_{WS} = \begin{bmatrix} D_WC_p & 0 & C_W \end{bmatrix} \tag{4.41}$$

$$D_{WS} = D_W \tag{4.42}$$

and 0 represents the zero matrix of the appropriate dimensions.

The state-space realizations given above allows value of the cost function J in Equation (4.14) to be computed. Furthermore, we can formulate the stable, fixed-order harmonic disturbance rejection controller synthesis problem as the optimization problem

$$\min_{\Theta} J(\Theta) \text{ subject to } S(s) \text{ stable, } K(s) \text{ stable} \tag{4.43}$$

4.1.3 Fixed-Order Controller Optimization

The $\mathcal{H}_\infty$ cost function J defined by Equation (4.14) is a function of P, Q, and the controller $K(s)$. Because the controller $K(s)$ is parameterized by Θ, the necessary conditions for a stationary point of J are

$$\frac{\partial J}{\partial P} = \bar{A}Q + Q\bar{A}^T + Q\bar{C}^T\bar{C}Q + \bar{B}\bar{B}^T = 0 \tag{4.44}$$

$$\frac{\partial J}{\partial Q} = \left(\bar{A} + Q\bar{C}^T\bar{C}\right)^T P + P\left(\bar{A} + Q\bar{C}^T\bar{C}\right) + \bar{C}^T\bar{C} = 0 \tag{4.45}$$

$$\frac{\partial J}{\partial \Theta} = 0 \tag{4.46}$$

For a given controller, the cost function J is computed by solving the Riccati equation given by Equation (4.44) for Q, and solving a Lyapunov equation given by Equation (4.45) for P. To ensure that the controller is stabilizing, we require the solution Q of Equation (4.44) to be symmetric and positive definite. To guarantee the controller is itself stable, we add the constraint that all the diagonal elements of A_c in Equation (4.29) be negative.

Since the desire to maximize bandwidth ω_B and minimize peak sensitivity $S_{\max}$ are generally in conflict, we can find a Pareto frontier of achievable performance by varying one parameter in an outer loop, and optimizing the other in an inner loop. Here, we describe an algorithm to obtain the Pareto frontier by varying ω_B over a range of bandwidths in the outer loop, and $S_{\max}$ is minimized in the inner loop. The algorithm for the inner loop optimization consists of the following steps:

1. For the given value of ω_B, find an initial feasible controller.
2. Find $S_{\max}$ such that $\sup\{\|T_{zd}\|_\infty\} = 1$.
3. Define the weighting filter $W(s)$ based on ω_B and $S_{\max}$.
4. Obtain a new controller by performing a conjugate gradient search on Θ to minimize J.
5. Iterate steps 2, 3, and 4 until the parameters of $K(s)$ converge.

We use the continuous-time HHC (CTHHC) approach of Hall and Wereley [44] to generate the initial feasible controller used in the inner loop optimization. The time constant parameter T_{n_i} for the CTHHC controller are all set to T, which yields a baseline controller with approximate bandwidth $\omega_B \approx 1/T$. The actual bandwidth achieved is found directly from

the sensitivity transfer function. The desired values of the bandwidths in the outer loop of the algorithm can be obtained by varying the value of T used to generate the baseline controllers.

To initialize the parameter vector Θ, the baseline CTHHC controller $K_0(s)$ is realized in state-space as

$$K_0(s) \sim \left(\begin{array}{c|c} A_1 & B_1 \\ \hline k_0 & 0 \end{array}\right) \tag{4.47}$$

where A_1 and B_1 are the same matrices as in Equation (4.26), and k_0 is used as the initial k in Equation (4.35). With the CTHHC given by

$$K_0(s) = \sum_{i=1}^{M} \frac{\alpha_i s + \beta_i n_i \Omega}{s^2 + (n_i \Omega)^2} \tag{4.48}$$

the initial k is simply

$$k_0 = \left[\begin{array}{cccccc} \alpha_1 & -\beta_1 & \alpha_2 & -\beta_2 & \ldots & \alpha_M \quad -\beta_M \end{array}\right] \tag{4.49}$$

The initial values for the diagonal elements of A_c, a_i, $i = 1, 2, \ldots, n_c$ are set to any negative number (we used -1 for most cases), the superdiagonal and subdiagonal elements of A_c, a_i, $i = n_c + 1, n_c + 2, \ldots, 2n_c - 1$ can be set to any number (we used 0 for most cases). The initial values for the elements of B_c are all set to zero. Since B_c is the zero vector, the output of the initial $K_c(s)$ is identically zero, and the initial controller is equivalent to the baseline CTHHC. Note that while $K_c(s)$ could be implemented in series with $kW_1(s)$, resulting in a fixed-order controller $K(s) = K_c(s)kW_1(s)$, we choose the parallel implementation of Equation (4.18) because it allows us to easily obtain an initial set of controller parameters as described above.

For each initial controller, the peak sensitivity is found by performing a binary search for the smallest $S_{\max}$ for which $\|T_{zd}\| < 1$. The performance metric J, which depends on ω_B, $S_{\max}$, and $K(s)$, is then minimized with respect to the parameters of $K(s)$ by a conjugate gradient search. Analytical expressions for the gradient are provided in the next section.

The algorithm described above requires a stabilizing initial controller. However, the baseline CTHHC algorithm does not produce controllers with bandwidths beyond a threshold value, which depends on the plant transfer function. The reason is that increasing the value of the bandwidth corresponds to increasing the value of the static gain in the CTHHC, eventually resulting in an unstable system. In order to obtain fixed-order controllers with bandwidths greater than the threshold value, we can instead find an initial controller with the desired peak sensitivity, and iterate on ω_B in the inner loop.

4.1.4 Analytical Gradient

The optimization in the fixed-order controller synthesis requires the gradient of the cost function, which can be obtained using numerical approximation. Since the controller parameter Θ given in Equation (4.37) are arranged such that the diagonal elements of A_c are listed first, the superdiagonal elements of A_c are listed second, elements of C_c are next, followed by the elements of k, the elements of the gradient are grouped similarly as

$$\frac{\partial J}{\partial \Theta} = \left[\begin{array}{cccc} \frac{\partial J}{\partial \theta_1} & \frac{\partial J}{\partial \theta_2} & \cdots & \frac{\partial J}{\partial \theta_{3n_c+2M-1}} \end{array} \right] \tag{4.50}$$

$$= \left[\begin{array}{ccccccccccc} \frac{\partial J}{\partial a_1} & \cdots & \frac{\partial J}{\partial a_{n_c}} & \frac{\partial J}{\partial a_{n_c+1}} & \cdots & \frac{\partial J}{\partial a_{2n_c-1}} & \frac{\partial J}{\partial b_1} & \cdots & \frac{\partial J}{\partial b_{n_c}} & \frac{\partial J}{\partial k_1} & \cdots & \frac{\partial J}{\partial k_{2M}} \end{array} \right] \tag{4.51}$$

$$= \left[\begin{array}{cccc} \frac{\partial J}{\partial \text{diag}(A_c)} & \frac{\partial J}{\partial \text{superdiag}(A_c)} & \frac{\partial J}{\partial B_c} & \frac{\partial J}{\partial k^T} \end{array} \right] \tag{4.52}$$

where

$$\text{diag}(A_c) = \left[\begin{array}{cccc} a_1 & a_2 & \ldots & a_{n_c} \end{array} \right]^T \tag{4.53}$$

$$\text{superdiag}(A_c) = \left[\begin{array}{cccc} a_{n_c+1} & a_{n_c+2} & \ldots & a_{2n_c-1} \end{array} \right]^T \tag{4.54}$$

The ith element of the gradient can be approximated using the forward finite difference formula

$$\frac{\partial J}{\partial \theta_i} \approx \frac{J(\Theta + \delta\theta_i e_i) - J(\Theta)}{\delta\theta_i} \tag{4.55}$$

where $\delta\theta_i$ is a small perturbation in the ith element of Θ, and

$$e_i = \begin{bmatrix} 0 & \dots & 0 & 1 & 0 & \dots & 0 \end{bmatrix}^T \quad (4.56)$$

$\uparrow$

ith element

The numerical approximation in Equation (4.55) requires solving Equation (4.14) with perturbed values of the controller parameters for each element of the gradient. Since computing the cost function J requires the solution of a Riccati equation (Equation (4.44)) and a Lyapunov equation (Equation (4.45)), it is computationally expensive to use the finite difference method to obtain the gradient for optimization purpose.

The gradient can be computed in a more efficient manner using analytical expressions. The analytical expressions are dependent on the formulation and parameterization of the fixed-order control synthesis problem. Here, we provide the analytical expressions for the gradient of the cost function, defined by Equation (4.14), with respect to Θ as defined by Equation (4.37).

Using the chain rule of differentiation for matrices, the general expression for the ith element of the gradient is

$$\frac{\partial J}{\partial \theta_i} = \text{trace}\left[\left(\frac{\partial J}{\partial \bar{A}}\right)^T\left(\frac{\partial \bar{A}}{\partial \theta_i}\right) + \left(\frac{\partial J}{\partial (\bar{B}\bar{B}^T)}\right)^T\left(\frac{\partial (\bar{B}\bar{B}^T)}{\partial \theta_i}\right) + \left(\frac{\partial J}{\partial (\bar{C}^T\bar{C})}\right)^T\left(\frac{\partial (\bar{C}^T\bar{C})}{\partial \theta_i}\right)\right] \quad (4.57)$$

where

$$\frac{\partial J}{\partial \bar{A}} = (QP)^T + PQ = 2PQ \tag{4.58}$$

$$\frac{\partial J}{\partial (\bar{B}\bar{B}^T)} = P \tag{4.59}$$

$$\frac{\partial J}{\partial (\bar{C}^T\bar{C})} = QPQ + Q \tag{4.60}$$

$$\begin{aligned}\frac{\partial \bar{A}}{\partial \theta_i} = & \frac{\partial A_{WS}}{\partial \theta_i} + \frac{\partial B_{WS}}{\partial \theta_i} R^{-1} D_{WS} C_{WS} \\ & + B_{WS} \frac{\partial (R^{-1})}{\partial \theta_i} D_{WS}^T C_{WS} + B_{WS} R^{-1} \frac{\partial D_{WS}^T}{\partial \theta_i} C_{WS} \\ & + B_{WS} R^{-1} D_{WS}^T \frac{\partial C_{WS}}{\partial \theta_i}\end{aligned} \tag{4.61}$$

$$\frac{\partial (\bar{B}\bar{B}^T)}{\partial \theta_i} = \frac{\partial B_{WS}}{\partial \theta_i} R B_{WS}^T + B_{WS} \frac{\partial R}{\partial \theta_i} B_{WS}^T + B_{WS} R \frac{\partial B_{WS}^T}{\partial \theta_i} \tag{4.62}$$

$$\begin{aligned}\frac{\partial (\bar{C}^T\bar{C})}{\partial \theta_i} = & \frac{\partial C_{WS}^T}{\partial \theta_i} \left(I + D_{WS} R^{-1} D_{WS}^T\right) C_{WS} \\ & + C_{WS}^T \frac{\partial \left(I + D_{WS} R^{-1} D_{WS}^T\right)}{\partial \theta_i} C_{WS} \\ & + C_{WS}^T \left(I + D_{WS} R^{-1} D_{WS}^T\right) \frac{\partial C_{WS}}{\partial \theta_i}\end{aligned} \tag{4.63}$$

$$\begin{aligned}\frac{\partial \left(I + D_{WS} R^{-1} D_{WS}^T\right)}{\partial \theta_i} = & \frac{\partial D_{WS}}{\partial \theta_i} R^{-1} D_{WS}^T + D_{WS} \frac{\partial R^{-1}}{\partial \theta_i} D_{WS}^T \\ & + D_{WS} R^{-1} \frac{\partial D_{WS}^T}{\partial \theta_i}\end{aligned} \tag{4.64}$$

To compute the gradient using Equations (4.57) to (4.64) requires the expressions for $\frac{\partial A_{WS}}{\partial \theta_i}$, $\frac{\partial B_{WS}}{\partial \theta_i}$, $\frac{\partial C_{WS}}{\partial \theta_i}$, $\frac{\partial D_{WS}}{\partial \theta_i}$, and $\frac{\partial R^{-1}}{\partial \theta_i}$. With the matrices R^{-1}, A_{WS}, B_{WS}, C_{WS}, and D_{WS} defined by Equations (4.13), (4.39)–(4.42), the partial derivatives with respect to θ_i are matrices whose elements are mostly, if not entirely, zeros. Substituting the required partial derivatives into Equations (4.57) to (4.64) results in the analytical expressions for

Table 4.1: Flight condition for wind tunnel testing

Flight Condition	1	2
Velocity, V (kt)	83	124
Advance ratio, μ	0.20	0.30
Tip Mach number, M_{T}	0.623	0.623
Advancing tip Mach number, M_{AT}	0.746	0.805
Shaft angle, α (deg)	2.0	-9.1
Blade loading coefficient, C_{T}/σ	0.075	0.075

the gradient

$$\frac{\partial J}{\partial a_i} = 2e_{n_p+i}^T PQe_{n_p+i}, \quad i = 1, \ldots, n_c \tag{4.65}$$

$$\frac{\partial J}{\partial a_{n_c+i}} = 2e_{n_p+1}^T PQe_{n_p+1+i} - 2e_{n_p+1+i}^T PQe_{n_p+i}, \quad i = 1, \ldots, n_c - 1 \tag{4.66}$$

$$\frac{\partial J}{\partial b_i} = 2C_p \begin{bmatrix} I & 0 \end{bmatrix} QPe_{n_p+i} + \frac{2D_{WS}^T}{R} C_{WS} QPe_{n_p+i} + \frac{2}{R} B_{WS}^T Pe_{n_p+i}, \quad i = 1, \ldots, n_c \tag{4.67}$$

$$\frac{\partial J}{\partial k_i} = 2B_p^T \begin{bmatrix} I & 0 \end{bmatrix} PQe_{n_p+n_c+i}, \quad i = 1, \ldots, n_{w_1} \tag{4.68}$$

where e_i is defined by Equation (4.56), I is the identity matrix of dimension $n_p \times n_p$, and 0 is the zero matrix of dimension $n_p \times (n_c + n_{w_1} + n_{w_2})$.

We note that the gradient is dependent on the parameterization of the problem, what we show in this section provides a template in obtaining analytical expression of the gradient for problems with different parameterizations.

4.2 Fixed-Order $\mathcal{H}_\infty$ Controller Performance

In this section, we examine the performance of the fixed-order $\mathcal{H}_\infty$ controllers. We consider the vibration reduction performance at two different flight conditions that are listed in Table 4.1. The helicopter rotor models for the two flight conditions were identified from wind tunnel test data collected by Hall *et al.* [42]. The order of the plant for Flight Condition 1 is

$n_p = 19$, and the order of the plant for Flight Condition 2 is $n_p = 15$. The fixed-order $\mathcal{H}_\infty$ higher harmonic controllers in this section are developed using the linear notch filter, hence its performance, in terms of peak sensitivity $S_{\max}$ and bandwidth ω_B, can be compared to the Pareto frontier established by the full-order $\mathcal{H}_\infty$ controller developed in Chapter 3 for the linear notch case.

One of the main motivations for the fixed-order methodology is to reduce the order of the controller. The baseline CTHHC is of order $2M$, where M is the number of harmonic frequencies to be attenuated, is the minimum order required for the HHC problem. The full-order $\mathcal{H}_\infty$ controller is of order $n_p + 10m + 2M$, where m is the order of the weighting filter, where $m = 6$ provides controllers with performance that approaches the performance limit. The order of the fixed-order $\mathcal{H}_\infty$ controller is

$$N_c = n_c + 2M \tag{4.69}$$

where n_c is the order of $K_c(s)$. Unlike the full-order $\mathcal{H}_\infty$ controller, the order of the fixed-order $\mathcal{H}_\infty$ controller is not dependent on the order of the plant or the weighting filter. For the results produced here, an 80th order weighting filter $W(s)$ is used ($M = 5$, $m = 8$), and we consider cases with $n_c \leq 5$. While the order of the weighting filter does not affect the order of the controller, it does impact the size of the optimization problem, since the matrices $\bar{A}$, $\bar{B}$, and $\bar{C}$ in Equations (4.44) and (4.45) are dependent on $W(s)$.

4.2.1 Sensitivity Transfer Function

The sensitivity transfer functions with fixed-order $\mathcal{H}_\infty$ controllers of order $N_c = 11$, 13, and 15 are shown in Figure 4-3 for Flight Condition 1, and in Figure 4-4 for Flight Condition 2. For both flight conditions, the bandwidths of the controllers are fixed at $\omega_B = 0.04$ per rev. From both Figure 4-3a and Figure 4-4a, it can be seen that a substantial decrease of peak sensitivity from the baseline CTHHC controller can be achieved with an increase in controller order of just one. It can also be seen that the peak sensitivity values decrease as the controller order N_c increases, and the sensitivity transfer functions become smoother with increasing N_c. While the sensitivity transfer functions of the full-order $\mathcal{H}_\infty$ cases

in Chapter 3 are smoother, the order of the full-order $\mathcal{H}_\infty$ controller, with comparable performance to the 15th order fixed-order controller, is greater than 30.

The details of the notches in the sensitivity function are shown in Figure 4-3b and Figure 4-4b. As the controller order N_c increases, the notches become more symmetric about the first harmonic frequency of 1 per rev. Because the definition of the bandwidth is the inverse of the steepest slope at either side of the harmonic frequencies to be attenuated, the optimization would try to keep the slopes the same (in magnitude) on either side of the harmonic frequencies, resulting in notches that are more symmetric.

4.2.2 Pareto Frontier

For Flight Condition 1, the performance achieved by the fixed-order $\mathcal{H}_\infty$ controller is shown in Figure 4-5. Within the range of bandwidths where $S_{\max} < 1.2$, both the 14th order and the 15th order fixed-order $\mathcal{H}_\infty$ controllers ($n_c = 4$, and $n_c = 5$, respectively) have peak sensitivity values within 0.01 of the peak sensitivity for the full-order $\mathcal{H}_\infty$ controller of 39th order. The 15th order fixed-order $\mathcal{H}_\infty$ controller has lower peak sensitivity than the 39th order full-order $\mathcal{H}_\infty$ controller when $\omega_B > 0.056$ per rev. Similar results apply to Flight Condition 2, as shown in Figure 4-6. Thus, the fixed-order $\mathcal{H}_\infty$ optimization technique may be preferable to the full-order $\mathcal{H}_\infty$ technique, especially if computational complexity of the controller is an important consideration for implementation.

4.3 Summary

Two problems associated with the full-order $\mathcal{H}_\infty$ controllers, namely the high controller order and lack of guarantee on the stability of the controller itself, led to the development of the fixed-order $\mathcal{H}_\infty$ control synthesis methodology. The fixed-order controllers are obtained by optimizing a cost function that reflects the $\mathcal{H}_\infty$ optimality of the closed-loop system. To ensure that the fixed-order controllers are stable, we use a controller parameterization that allows the stability of the controller to be formulated as a constraint in the optimization problem. We present the analytical expressions for the gradient, and use them in the optimization algorithm for better efficiency. Compared to the baseline CTHHC con-

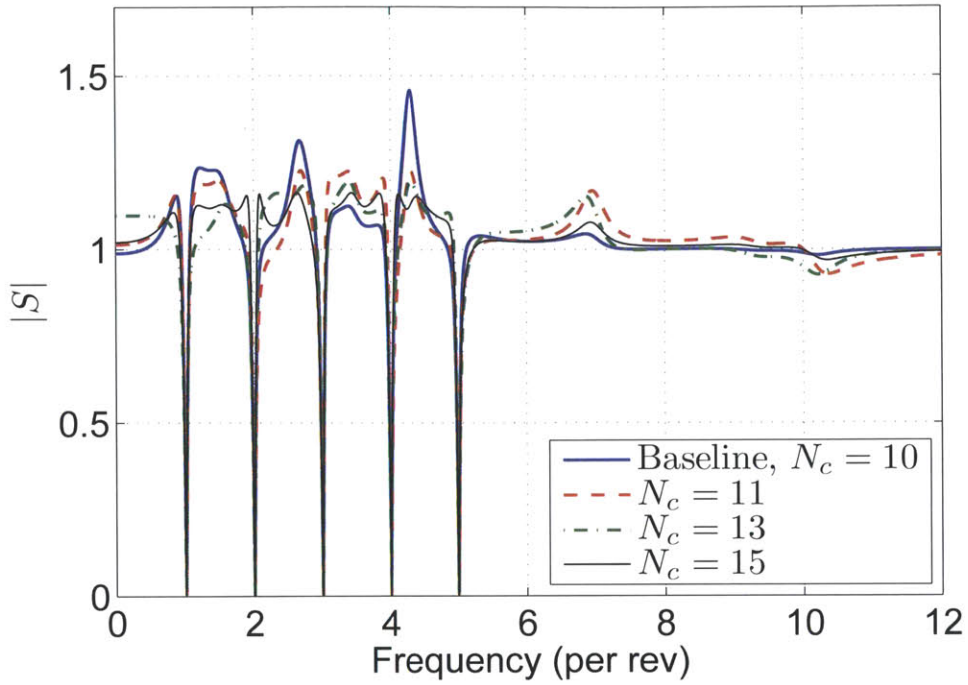

(a) Sensitivity transfer functions

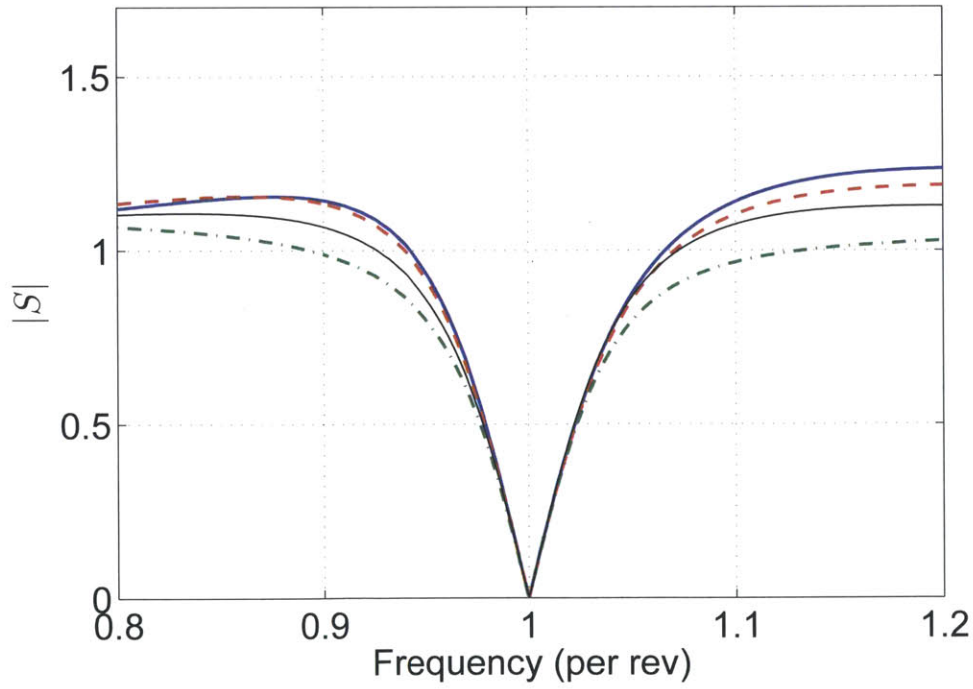

(b) Close-up view at the first harmonic frequency

Figure 4-3: Sensitivity transfer function with fixed-order $\mathcal{H}_\infty$ controllers for Flight Condition 1

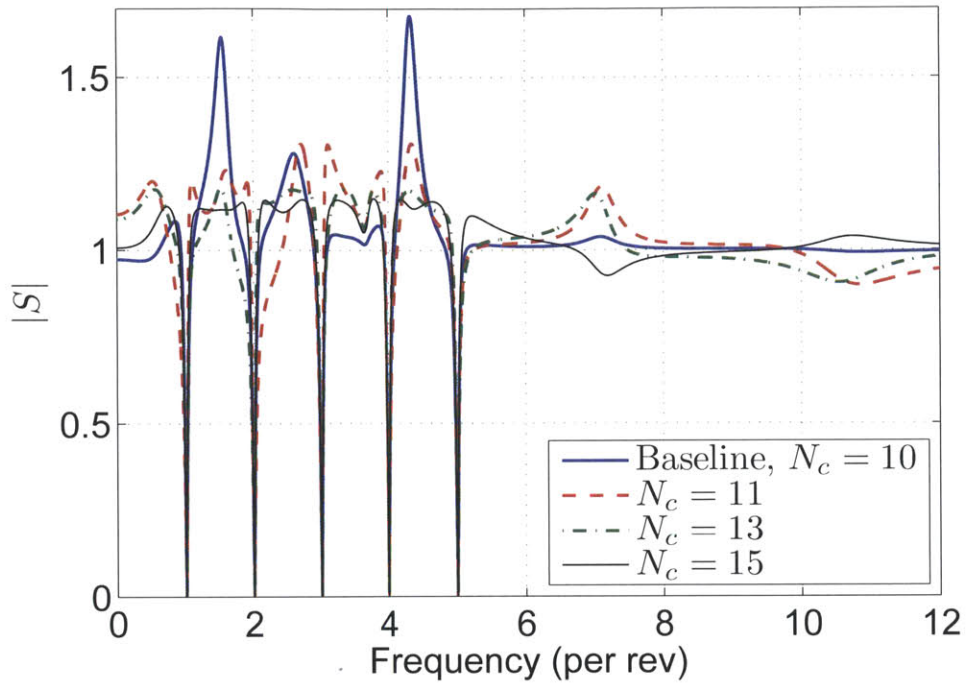

(a) Sensitivity transfer functions

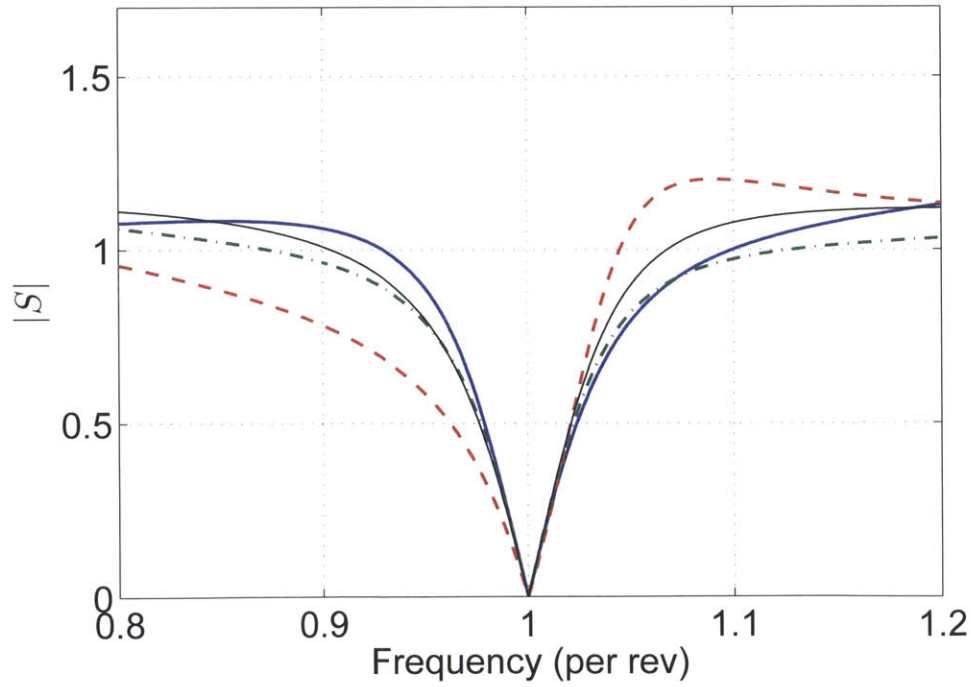

(b) Close-up view at the first harmonic frequency

Figure 4-4: Sensitivity transfer function with fixed-order $\mathcal{H}_\infty$ controllers for Flight Condition 2

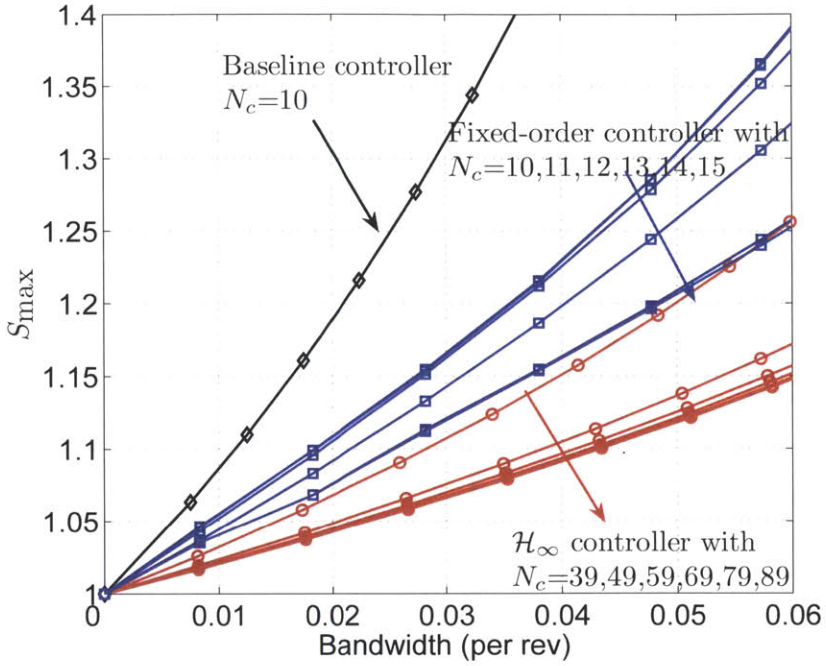

Figure 4-5: Performance comparison between controllers for Flight Condition 1

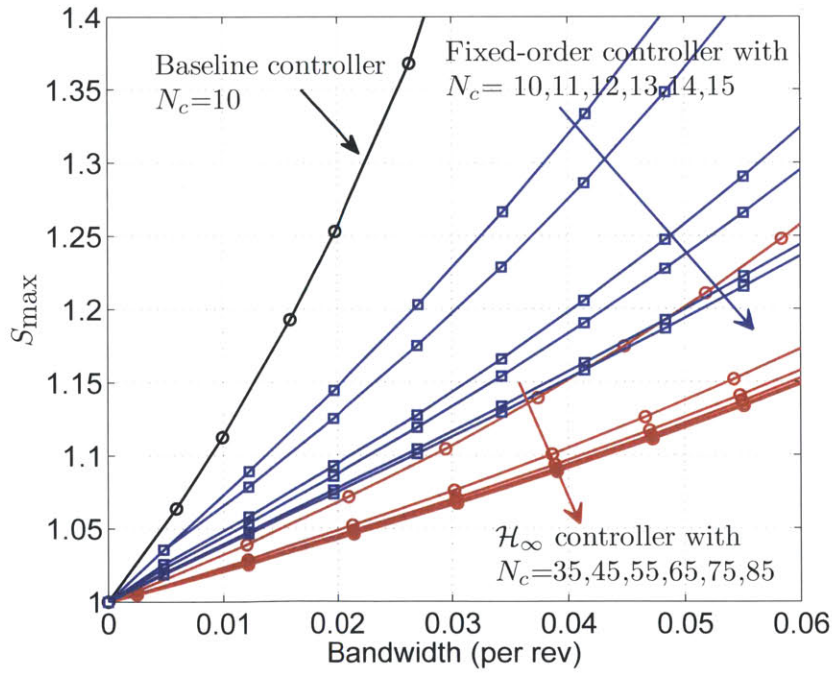

Figure 4-6: Performance comparison between controllers for Flight Condition 2

trollers, the optimized fixed-order $\mathcal{H}_\infty$ controllers have approximately twice the bandwidth, for a given peak sensitivity, with only a small increase in the controller order. Compared to the full-order $\mathcal{H}_\infty$ controllers, the optimized fixed-order controllers of order $N_c = 15$ provide performance comparable to full-order $\mathcal{H}_\infty$ controllers with orders that are higher by a factor of at least two.

Chapter 5

Helicopter Rotor Model for Higher Harmonic Control

For this thesis, the purpose of the helicopter rotor model is to enable the design of controllers for harmonic disturbance rejection. To achieve effective harmonic disturbance rejection, it is necessary to understand the behavior of the physical system, and in particular, the characteristics of the disturbance. Instead of formulating a model of the helicopter rotor from first principles, we derived the model using data from previously conducted wind tunnel tests and nonlinear simulations. In this chapter, we first analyze the wind tunnel data to quantify the harmonic disturbance and examine the effects of periodicity. We then obtain parametric models of the helicopter rotor plant suitable for control synthesis. Because the effect of periodicity does not appear to be significant, we proceed to implement a system identification procedure to obtain linear time-invariant (LTI) models of the helicopter rotor at different flight conditions. Since the wind tunnel data is limited to only two different flight conditions, we use nonlinear simulation data generated by the Boeing Company to obtain additional LTI models to cover the flight envelope. The models identified from the simulation data show the same qualitative characteristics as the wind tunnel data, enabling us to determine the relative importance of different flight parameters on the plant behavior.

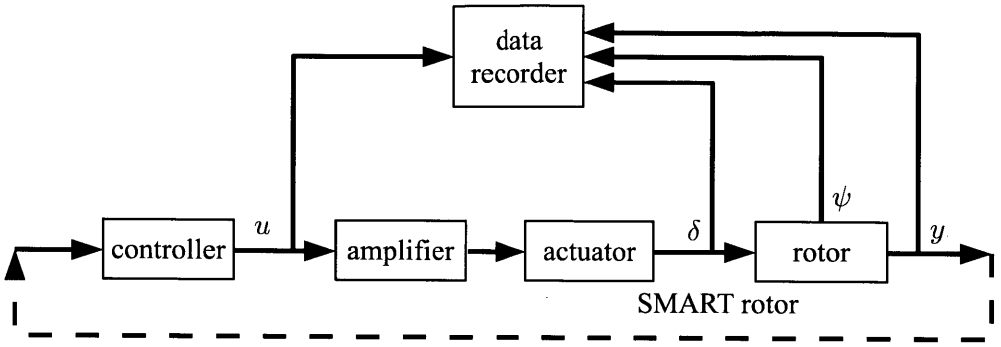

Figure 5-1: Simplified block diagram of helicopter control system in wind tunnel test

5.1 Plant Models from Wind Tunnel Test Data

To demonstrate our control synthesis techniques, we use plant models based on the Boeing Smart Material Actuated Rotor Technology (SMART) helicopter rotor. The SMART rotor has $N = 5$ rotor blades, with a nominal rotor rotational speed of $\Omega = 392$ rpm. Each blade of the rotor contains an active partial span trailing edge flap that can be driven independently, via a piezoelectric actuator, to produce a change in the rotor forces and moments. Details on the SMART rotor and its piezoelectric actuators can be found in [43, 97].

5.1.1 Wind Tunnel Test Setup

The test data we used to generate the plant models were collected by Hall *et al.* in 2008 [42] at the Air Force National Full-Scale Aerodynamic complex 40- by 80-foot anechoic wind tunnel. The test setup consisted of a full-scale SMART rotor supported on top of the Large Rotor Test Stand, and the necessary instrumentation to record the data. Figure 5-1 shows a simplified block diagram of the components and the recorded signals in the wind tunnel test. The recorded signals relevant for our purpose are the controller output u, the individual on-board trailing edge flap deflections δ, the rotor azimuthal position ψ, and the rotor hub normal force y. We consider the collective voltage generated by the controller[1] as the input to the plant, and the deviation from the nominal hub normal force of the rotor as the output of the plant.

[1]For the collective command, the voltage generated by the controller is supplied to the actuators without any phase shift. The voltage generated by the controller is amplified before it reaches the individual piezoelectric actuators.

Table 5.1: Flight conditions for wind tunnel testing

Flight Condition	1	2
Velocity, V (kt)	83	124
Advance ratio, μ	0.20	0.30
Tip Mach number, M_{T}	0.623	0.623
Advancing tip Mach number, M_{AT}	0.746	0.805
Shaft angle, α (deg)	2.0	-9.1
Blade loading coefficient, C_{T}/σ	0.075	0.075

The wind tunnel test session included open-loop tests with no control input to determine the baseline harmonic vibration level, open-loop tests with three successive sinusoidal sweeps as control input for system identification purpose, and closed-loop tests to examine the performance of the baseline higher harmonic controllers. The frequency of the sinusoidal sweep signal for system identification varied linearly from 0 Hz to 80 Hz over a span of 40 seconds, with a pause of 5 seconds in between each sinusoidal sweep. All of the tests were conducted for two different flight conditions. Flight Condition 1 simulates descending flight, and Flight Condition 2 simulates level cruising flight. The parameters of the two flight conditions are shown in Table 5.1

Since there was some variation of the rotor frequency Ω during the wind tunnel test, the period of the system is not constant in terms of time. Although the variation in Ω was small, it nevertheless complicates the analysis. However, if the independent variable is the azimuthal position of the rotor, instead of time, the period of the system will be constant, almost by definition. Thus, it is convenient to use the azimuthal position of the rotor as the independent variable in describing rotor dynamics. Since the azimuthal position ψ of the rotor was collected during the wind tunnel test, we re-sample the time stamped input and output data in constant azimuthal intervals, and use the azimuthal position as the independent variable in our analysis of the data and for the models[2]. The unit of the azimuthal position is revolution, abbreviated by rev, and rad/rev is the unit of the corresponding angular frequency. The frequency has the unit per rev (/rev).

[2]The "time" in linear time-invariant and linear time-periodic system refers to the independent variable, which for our case is the azimuthal position of the helicopter rotor.

5.1.2 Open-Loop Spectrum

The open-loop wind tunnel tests allow us to characterize the disturbance experienced by the helicopter rotor. The spectrum of the disturbance is obtained by applying the fast Fourier transform (FFT) to the hub normal force data. However, since the FFT is a discrete Fourier transform, in order to correctly represent the harmonic components in the time history as impulses in the spectrum, the length of the data must contain an integral number of periods of all the harmonic components, and the sampling rate must result in an integral number of data points within each period. Thus, we have to regularize the time stamped hub normal force data before the application of the FFT. The regularization procedure consists of interpolating and re-sampling the time history data so that the independent variable is in constant azimuthal increment of $1/360$ rev, then the data is truncated to the nearest multiple of a complete revolution. Once regularized, any pure harmonic component of the data will appear as impulses in the spectrum. Not regularizing the data will result in spectral leakage when the FFT is applied, which is manifested as the broadening of the peaks at the harmonic frequencies in the spectrum.

The baseline levels of the harmonic vibrations can be seen in the spectra of the hub normal force for Flight Conditions 1 and 2, shown in Figure 5-2. The unit of the vertical axis for the spectrum plot is arbitrary, because the magnitude of the harmonic components is proportional to the length of the data, and hence the ratio of the magnitude between the harmonic and the broadband part of the spectrum is dependent on the number of sample points in the FFT. The spectra show impulses at almost all the harmonic frequencies, instead of at just multiples of 5 per rev as typically expected for a symmetric rotor with 5 blades. The existence of vibration at nearly all harmonics is indicative of asymmetry in the rotor, which could result in blade-to-blade tracking error. The non-harmonic and slightly broadened peak at approximately 6.2 per rev is due to transmission gear-tooth mesh frequency.

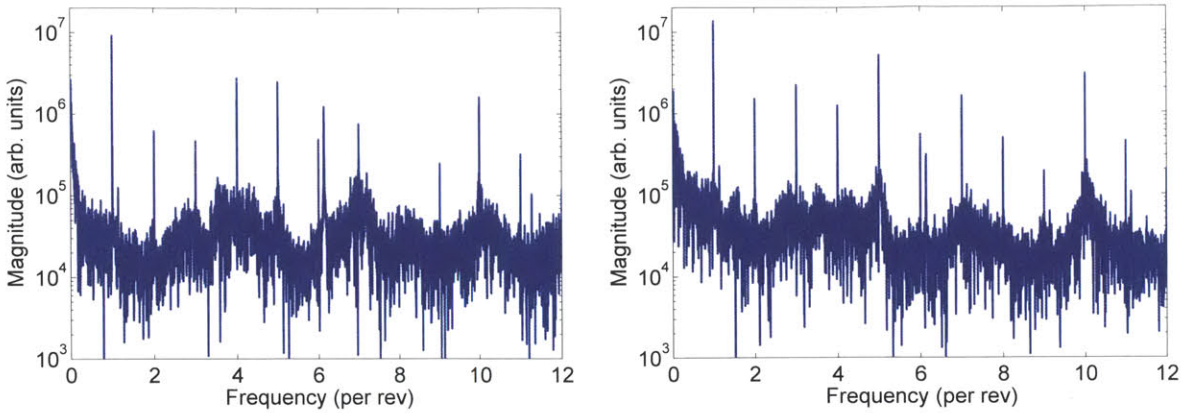

(a) Open-loop spectrum for Flight Condition 1

(b) Open-loop spectrum for Flight Condition 2

Figure 5-2: Spectra of hub normal force without vibration control

5.1.3 Harmonic Transfer Functions

Due to the periodicity of the helicopter rotor in operation, it may be modeled as a linear time-periodic (LTP) system. The general state-space representation of an LTP system is

$$\dot{x}(t) = A(t)x(t) + B(t)u(t) \tag{5.1}$$

$$y(t) = C(t)x(t) + D(t)u(t) \tag{5.2}$$

where the matrices $A(t)$, $B(t)$, $C(t)$, and $D(t)$ are periodic with period T, *i.e.*, $A(t+kT) = A(t),\ k \in \mathbb{Z}$.

LTP systems cannot be represented in the frequency domain by transfer functions, since multiple input frequencies contribute to the output at a given frequency. Wereley and Hall [102] introduced the harmonic transfer function (HTF) to describe the frequency response of LTP systems. For the purpose of LTP system identification, Siddiqi [89] proposed an input-output relationship of the form

$$Y(j\omega) = \sum_{i=-\infty}^{\infty} \mathcal{G}_i(j\omega)U(j(\omega - iN\Omega)) \tag{5.3}$$

for an N-bladed helicopter rotor with rotor frequency Ω. In Equation (5.3), $\mathcal{G}_i,\ i = \ldots, -1, 0, 1, \ldots$, are the harmonic transfer functions of the helicopter rotor, Y is the Fourier

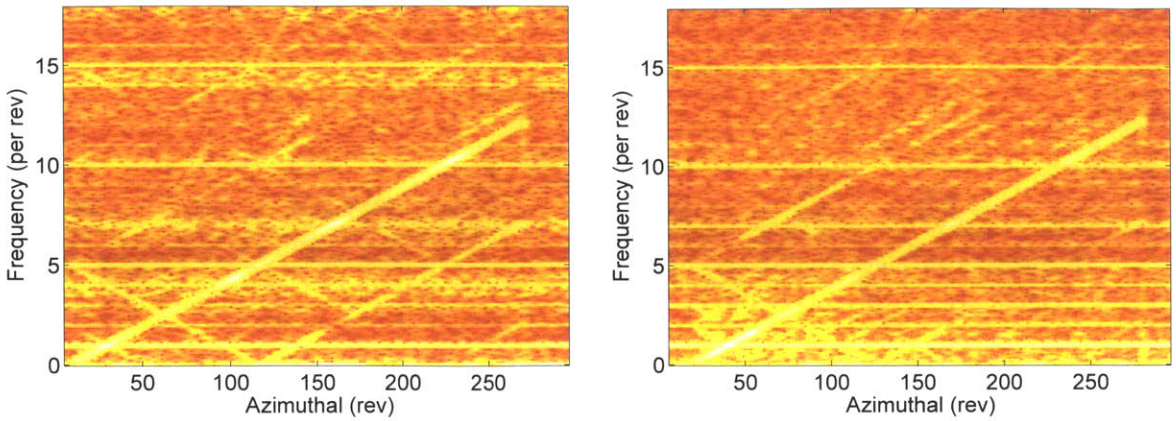

(a) Spectrogram for Flight Condition 1

(b) Spectrogram for Flight Condition 2

Figure 5-3: Spectrograms of rotor response to linear sinusoidal sweep input

transform of the output y, and U is the Fourier transform of the input u. To estimate the harmonic transfer functions, it is only necessary to consider a finite number of $\mathcal{G}_i$. To determine the number of terms to include in the summation of Equation (5.3), we can qualitatively examine the effect of periodicity using the spectrogram of the output data.

The spectrograms of the hub normal force measured in the wind tunnel are shown in Figure 5-3. The x-axis of the spectrogram represents the independent variable, which in our case is the rotor azimuthal position. The y-axis of the spectrogram represents frequency. The amplitude of the data is represented by the color intensity, with lighter color corresponding to higher amplitude. The spectrogram is obtained by dividing the measured hub normal force into overlapping segments, and applying FFT to each segment. The color intensity of a vertical slice of the spectrogram at azimuthal position $\psi = \psi_1$ is a snapshot of the relative magnitude of the FFT for the segment of hub normal force data that starts at ψ_1. A horizontal slice of the spectrogram at frequency $f = f_1$ shows the relative amplitude of the component of hub normal force with frequency f_1 as a function of azimuthal position. Because a linear sinusoidal sweep was used as the excitation signal, the color intensity of the diagonal line starting at the lower left corner represents the response of $\mathcal{G}_0$ to the input. The magnitude of the response of $\mathcal{G}_i,\ i = 1, 2, \ldots$, are represented by the color intensities of the diagonal lines that are $5i$ per rev above the main diagonal line, while those below correspond to $\mathcal{G}_i,\ i = -1, -2, \ldots$. Since the responses of $\mathcal{G}_i,\ |i| > 1$, appear negligible,

we consider only three terms, $i = -1, 0, 1$, in Equation (5.3). Also apparent in the spectrogram are the harmonic disturbances, which appear as horizontal lines at the harmonic frequencies.

We follow the identification procedure developed by Siddiqi [89] to obtain the values of the harmonic transfer functions $\mathcal{G}_{-1}$, $\mathcal{G}_0$, and $\mathcal{G}_1$. First, both the input and output data are regularized as described in the previous section. We then remove all the harmonic components from the data, since we will include them as additive output disturbances in our model. Next, the processed input data $u(t)$ is modulated by complex exponential functions to generate the modulated input signals

$$u_{+1}(t) = u(t)\exp(j5\Omega t) \tag{5.4}$$

$$u_{-1}(t) = u(t)\exp(-j5\Omega t) \tag{5.5}$$

The Fourier transform of the signals u_{+1} and u_{-1} are

$$U_{+1}(j\omega) = U(j(\omega - 5\Omega)) \tag{5.6}$$

$$U_{-1}(j\omega) = U(j(\omega + 5\Omega)) \tag{5.7}$$

which are frequency shifted version of the Fourier transform of u. Substituting the modulated input signals into Equation (5.3) results in

$$Y(j\omega) = \begin{bmatrix} U_{+1}(j\omega) & U_0(j\omega) & U_{-1}(j\omega) \end{bmatrix} \begin{bmatrix} \widehat{\mathcal{G}}_1(j\omega) \\ \widehat{\mathcal{G}}_0(j\omega) \\ \widehat{\mathcal{G}}_{-1}(j\omega) \end{bmatrix} = \mathbf{U}(j\omega) \begin{bmatrix} \widehat{\mathcal{G}}_1(j\omega) \\ \widehat{\mathcal{G}}_0(j\omega) \\ \widehat{\mathcal{G}}_{-1}(j\omega) \end{bmatrix} \tag{5.8}$$

where $\widehat{\mathcal{G}}_1$, $\widehat{\mathcal{G}}_0$, and $\widehat{\mathcal{G}}_{-1}$ are, respectively, the estimates of the harmonic transfer functions $\mathcal{G}_1$, $\mathcal{G}_0$, and $\mathcal{G}_{-1}$. The empirical harmonic transfer functions $\widehat{\mathcal{G}}_1$, $\widehat{\mathcal{G}}_0$, and $\widehat{\mathcal{G}}_{-1}$ are obtained by solving

$$\widehat{\mathbf{\Phi}}_{\mathbf{U}Y}(j\omega) = \widehat{\mathbf{\Phi}}_{\mathbf{U}\mathbf{U}}(j\omega) \begin{bmatrix} \widehat{\mathcal{G}}_1(j\omega) \\ \widehat{\mathcal{G}}_0(j\omega) \\ \widehat{\mathcal{G}}_{-1}(j\omega) \end{bmatrix} \tag{5.9}$$

where

$$\widehat{\mathbf{\Phi}}_{\mathbf{U}Y}(j\omega) = \begin{bmatrix} \widehat{\Phi}_{U_{+1}Y}(j\omega) \\ \widehat{\Phi}_{UY}(j\omega) \\ \widehat{\Phi}_{U_{-1}Y}(j\omega) \end{bmatrix} \tag{5.10}$$

$$\widehat{\mathbf{\Phi}}_{\mathbf{U}\mathbf{U}}(j\omega) = \begin{bmatrix} \widehat{\Phi}_{U_{+1}U_{+1}}(j\omega) & \widehat{\Phi}_{U_{+1}U}(j\omega) & \widehat{\Phi}_{U_{+1}U_{-1}}(j\omega) \\ \widehat{\Phi}_{UU_{+1}}(j\omega) & \widehat{\Phi}_{UU}(j\omega) & \widehat{\Phi}_{UU_{-1}}(j\omega) \\ \widehat{\Phi}_{U_{-1}U_{+1}}(j\omega) & \widehat{\Phi}_{U_{-1}U}(j\omega) & \widehat{\Phi}_{U_{-1}U_{-1}}(j\omega) \end{bmatrix} \tag{5.11}$$

The elements of the matrices in Equations (5.10) and (5.11) are estimates of the auto- and cross-spectral densities obtained using the Blackman-Tukey procedure [10], with a Gaussian window used for smoothing [14].

The magnitude of $\widehat{\mathcal{G}}_{-1}$, $\widehat{\mathcal{G}}_0$, and $\widehat{\mathcal{G}}_1$ for both flight conditions are shown in Figure 5-4. The empirical harmonic transfer functions are only plotted up to a frequency of 7 per rev, because the highest frequency in the sinusoidal sweep signal only excites $\widehat{\mathcal{G}}_{-1}$ to 7 per rev. As evident in Figure 5-4, the magnitude of the empirical harmonic transfer functions $\widehat{\mathcal{G}}_{-1}$ and $\widehat{\mathcal{G}}_{+1}$ are approximately an order of magnitude lower than the magnitude of $\widehat{\mathcal{G}}_0$, which leads to our conclusion that the helicopter rotor blade at a constant flight condition can effectively be treated as an LTI system.

5.2 Parametric Models for Control Synthesis

Since the wind tunnel test data showed that the effect of periodicity on the helicopter rotor is small, we proceed to model it as an LTI system, with the harmonic disturbance treated as an additive disturbance to the output of the system. In this section, we first find the empirical transfer functions from the data, and then derive parametric models of the helicopter rotor. The empirical transfer function is a nonparametric model, which allows us to generate the initial parameters needed for obtaining a parametric model. The parametric model is in the

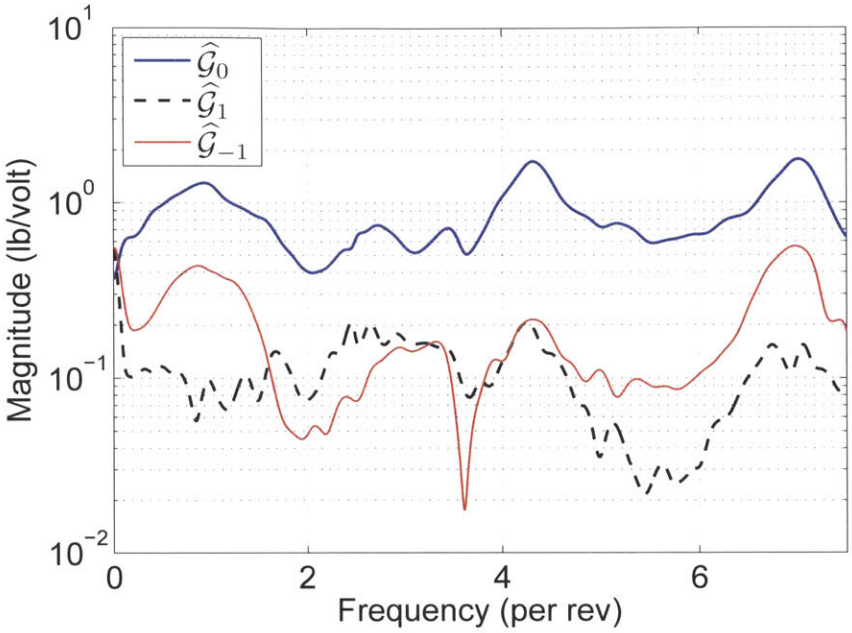

(a) Flight Condition 1

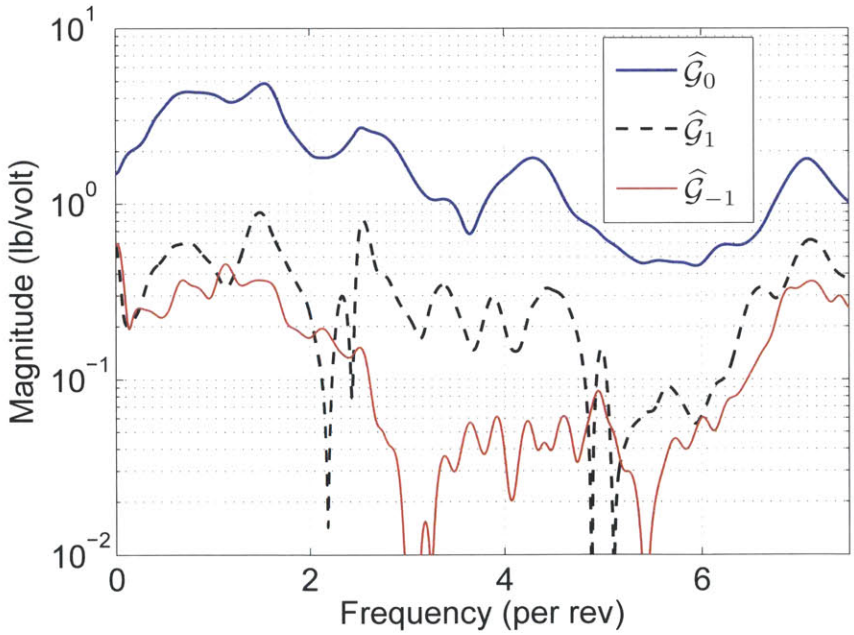

(b) Flight Condition 2

Figure 5-4: Harmonic transfer functions

form of a rational transfer function, whose coefficients in the numerator and denominator are obtained by optimizing the output prediction error.

5.2.1 Empirical Transfer Functions

In this section, we use the wind tunnel data to obtain the empirical transfer function estimates (ETFE) for both flight conditions. The process for generating the ETFE is similar to the process of generating the empirical harmonic transfer function described in Section 5.1.3, and is summarized in the following steps:

1. The input and output data are interpolated and re-sampled, so that the samples occur at regular azimuthal increments. The data are then truncated to the nearest integral number of rotor revolutions. This step is necessary so that the resulting power spectral densities, obtained using FFT, appropriately represent the periodic vibrations as line spectra at the harmonic frequencies.

2. The harmonic components of the data are removed for the first 12 harmonics[3], the transmission gear-tooth mesh noise at 6.2 per rev is also removed. This step is necessary because almost all of the energy in the output at the harmonics is due to the disturbance, not the control input.

3. Estimates of the autospectral density of the input $\widehat{\Phi}_{UU}(j\omega)$, and the cross-spectral density of the input and output $\widehat{\Phi}_{UY}(j\omega)$, are obtained using the Blackman-Tukey method with a Gaussian window [10, 14].

4. The ETFE at $j\omega$ is calculated as the ratio of the spectral density estimates at each frequency [69]

$$\widehat{G}_{\text{ETFE}}(j\omega) = \frac{\widehat{\Phi}_{UY}(j\omega)}{\widehat{\Phi}_{UU}(j\omega)} \tag{5.12}$$

The ETFE for the two flight conditions are shown in Figure 5-5 . While the empirical

[3]The bandwidth of the sinusoidal sweep input signal is 80 Hz, which corresponds to 12.25 per rev. We do not remove harmonic components beyond 12 per rev since the data only allows the model to be valid up to 12 per rev.

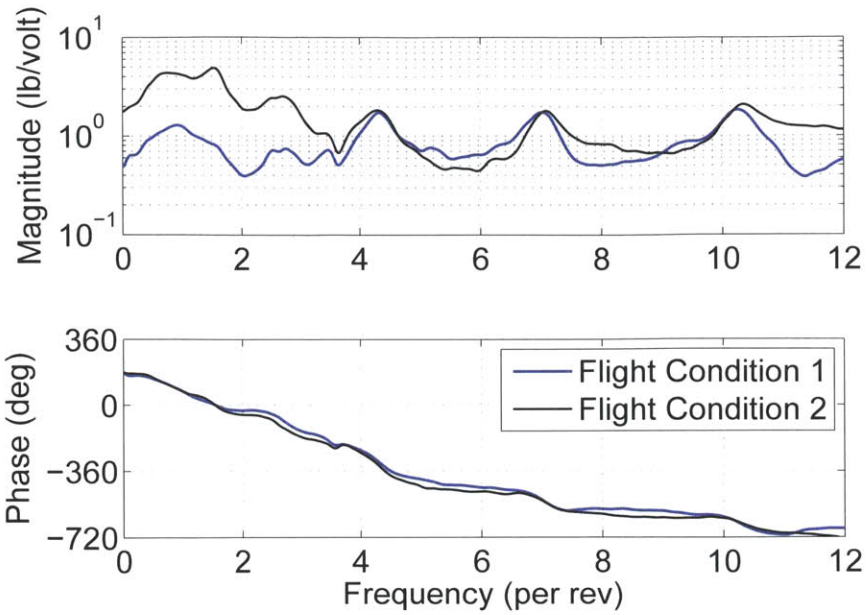

Figure 5-5: ETFE from wind tunnel test data

transfer function can be used in the frequency response methods of classical control theory for control design, our optimization based methods require a state-space model of the system. In the next section, we obtain a rational transfer function model based on the wind tunnel data, with initial parameters generated from the empirical transfer function. The rational transfer function can be realized in state-space form, providing the model we need for control synthesis.

5.2.2 Parametric Model

For the purpose of parametric system identification of the helicopter rotor, we consider a rational transfer function of the form

$$\widehat{G}(s;\Theta) = \sum_{i=1}^{N} \frac{b_{i1}s + b_{i2}}{s^2 + a_{i1}s + a_{i2}} + d_1 \tag{5.13}$$

where M is the number of second order systems in the model, and the real coefficients d_1, b_{i1}, b_{i2}, a_{i1}, a_{i2}, $i = 1, 2, \ldots, M$, form the unknown parameter vector Θ, which we seek to determine.

The output error E is defined as

$$E(j\omega;\Theta) = Y(j\omega) - \widehat{G}(j\omega;\Theta)U(j\omega) \tag{5.14}$$

where U and Y are, respectively, the input and output data from the wind tunnel test. In order to obtain the unknown coefficients in Equation (5.13), we minimize the cost function J, defined as the weighted squared output error

$$J = \|E(j\omega;\Theta)\|^2_{W(j\omega)} = \int |W(j\omega)E(j\omega;\Theta)|^2 \, d\omega \tag{5.15}$$

where $W(j\omega)$ is a frequency dependent weighting function. Without the weighting function $W(j\omega)$ in Equation (5.15), the transfer function near the complex poles of the system where the transfer function's magnitude is large will be fitted well, but since the response around the system zeros is small, the transfer function in the vicinity of the zero generally will not be fitted well. Thus, we select the weighting function to be the inverse of the empirical transfer function

$$W(j\omega) = \widehat{G}^{-1}_{\text{ETFE}}(j\omega) \tag{5.16}$$

to fit the transfer function well at all frequencies. See Ljung [69] for a more in-depth discussion on parametric system identification.

To optimize the cost function shown in Equation (5.15), a computer program was written to compute the value of the cost function J. The gradient $\frac{\partial J}{\partial \Theta}$ is obtained through the use of automatic differentiation software [18]. The automatic differentiation software analyzes the lines of the computer program that computes the value of J, and then produces a computer program that computes the values of the gradient.

Based on the data from the wind tunnel test, we know the plant is stable, so we impose a stability constraint on the identified system. The stability constraint is formulated as

$$a_{ij} \;>\; 0, \quad i = 1,2,\ldots,M,\; j = 1,2 \tag{5.17}$$

which is the necessary and sufficient condition for the stability of the system shown in

Equation (5.13).

The initial parameters of the parametric model are obtained from the magnitude of the empirical transfer function $\left|\widehat{G}_{\text{ETFE}}\right|$. We first locate all the peaks in $\left|\widehat{G}_{\text{ETFE}}\right|$ that indicate the likely presence of complex poles, the total number of peaks is denoted by M. For each peak, a stable second order system of the form

$$\frac{\beta_{i2}}{-\omega^2 + \alpha_{i1} j\omega + \alpha_{i2}}, \quad i = 1, 2, \ldots, M \tag{5.18}$$

is fitted to $\widehat{G}_{\text{ETFE}}$ using the least squares method. The range of data used to obtain the real parameters α_{i1}, α_{i2}, and β_{i2}, $i = 1, 2, \ldots, M$, in Equation (5.18) is dependent on the width of the peak. We typically use a frequency range of 0.1 per rev or less around each peak. The initial parameters needed for the optimization are

$$b_{i1} = 0, \quad i = 1, 2, \ldots, M \tag{5.19}$$

$$b_{i2} = \beta_{i2}, \quad i = 1, 2, \ldots, M \tag{5.20}$$

$$a_{i1} = \alpha_{i1}, \quad i = 1, 2, \ldots, M \tag{5.21}$$

$$a_{i2} = \alpha_{i2}, \quad i = 1, 2, \ldots, M \tag{5.22}$$

$$d_1 = 0 \tag{5.23}$$

A conjugate gradient optimization algorithm is used to obtain the optimal parameter vector Θ, with the automatic differentiation software generated program used to compute the gradient. In our cases, the resulting transfer functions are just proper (d_1 is not zero for both flight conditions). To facilitate control design, an additional pole at $s = -2\pi 50$ rad/rev (50 per rev) is added by multiplying the identified models by

$$\frac{1}{s/2\pi 50 + 1} \tag{5.24}$$

The additional pole makes the model strictly proper, and has only a small effect on the transfer function within the frequency range in which the model is valid. The resulting rational transfer function models of the helicopter rotor are plotted in Figure 5-6, with the

ETFE for the corresponding flight condition plotted for comparison. The models for Flight Conditions 1 and 2 are 19th and 15th order, respectively. For both flight conditions, the phase of the parametric model closely matches the phase of the ETFE, and the magnitude is relatively close as well.

In the case that the parametric model does not match the ETFE well, a different set of initial parameters could be generated using different range of frequencies around the peaks of $\left|\widehat{G}_{\text{ETFE}}\right|$, and different combinations of the peaks could be selected as well. In addition, in the frequency ranges that are poorly fitted, additional second order systems could be added with $\beta_{i2} = 0,\ i = M+1, \ldots$, and the denominator chosen to reflect frequency ranges.

5.2.3 Actuator Model and System Delay

Besides providing the information for creating the plant models, the wind tunnel test data can also be used to obtain the delay in the system, as well as the dynamics of the actuator. Since we treat the collective input voltage to the amplifier instead of the piezoelectric actuators as the plant input, the plant contains the dynamics of the actuator and the amplifier. Using the closed-loop wind tunnel test data, we can examine the transfer function from the controller output u to the averaged flap deflection δ, denoted by $T_{\delta u}$. The empirical transfer function $T_{\delta u}$, obtained using the procedure described in Section 5.2.1, is shown in Figure 5-7. The combined dynamics of the actuator and amplifier has relatively flat frequency response as expected, but adds approximately 28 deg of phase lag to the system throughout the bandwidth of the model. Unfortunately, since the amplifier voltage was not recorded, we cannot determine the individual transfer functions of the amplifier and the actuators.

In addition to $T_{\delta u}$, the empirical transfer function from the plant output (rotor hub normal force) to the controller output, denoted by T_{uy}, can also be examined. Ideally, T_{uy} should be identical to the baseline controller K used in the closed-loop wind tunnel test, implying that

$$\widehat{H} = T_{uy}K^{-1} \approx 1 \tag{5.25}$$

However, computing $\widehat{H} = T_{uy}K^{-1}$ results in the frequency response shown in Figure 5-8.

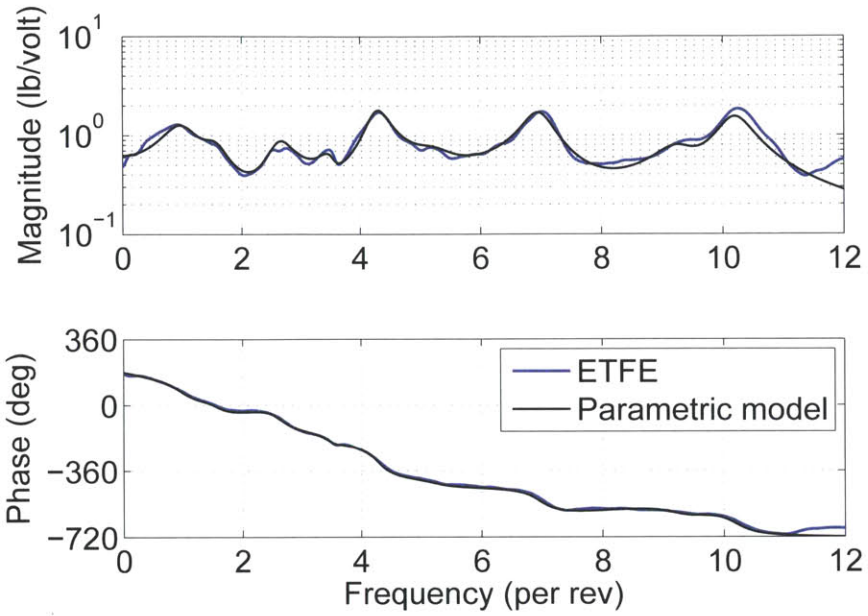

(a) Flight Condition 1

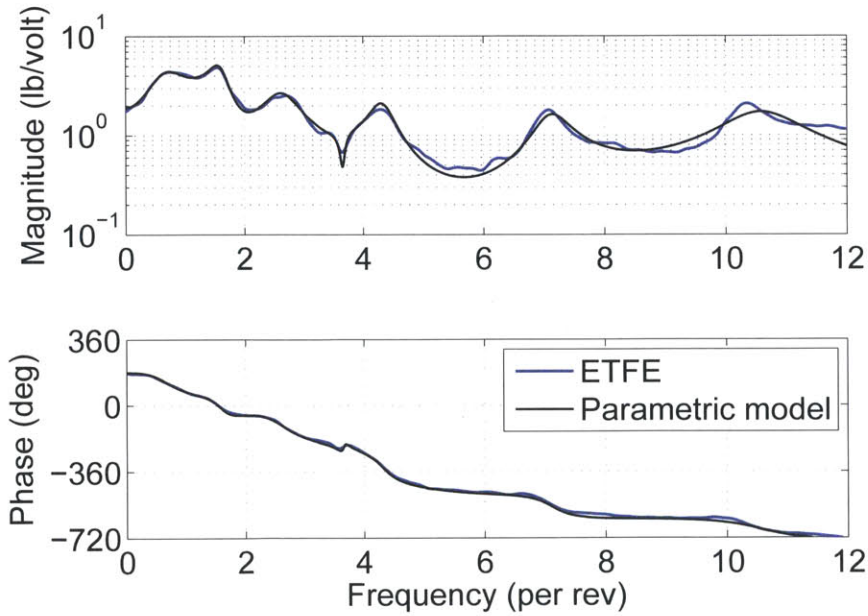

(b) Flight Condition 2

Figure 5-6: Comparison between ETFE and parametric model from wind tunnel data

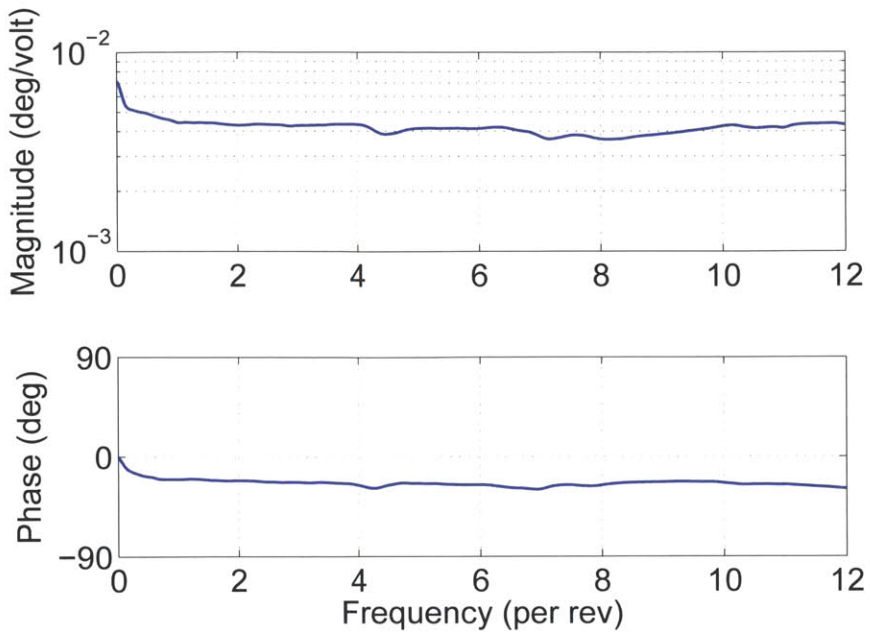

Figure 5-7: Frequency response of $T_{\delta u}$, the transfer function from controller output to averaged flap deflection

The magnitude response of $\widehat{H}$ is close to unity, with notches at the harmonic frequencies resulting from the poles of the baseline controller K at the harmonic frequencies, which also cause the spikes in the phase response plot. The phase can be seen to be linearly decreasing, indicative of a pure time delay element. The amount of time delay can be estimated by the slope of the phase response plot. A best fit line is superimposed on the phase plot, this line has a slope of 7.0° per rev. The time delay adversely affects the performance of the controller, so knowing the amount of time delay allows the design to account for it in order to achieve better performance. The estimated delay of 7.0° per rev in effect represents the total delay in the closed-loop system, including the amplifier, the actuator, the A/D converter, the sensors, and the computation time of the controller. However, it is surmised that the amplifier is the main contributor to the total delay.

5.3 CAMRAD Simulation

The wind tunnel test provided data for two different flight conditions, from which we obtained two different LTI models of the helicopter rotor for controller synthesis. Each of

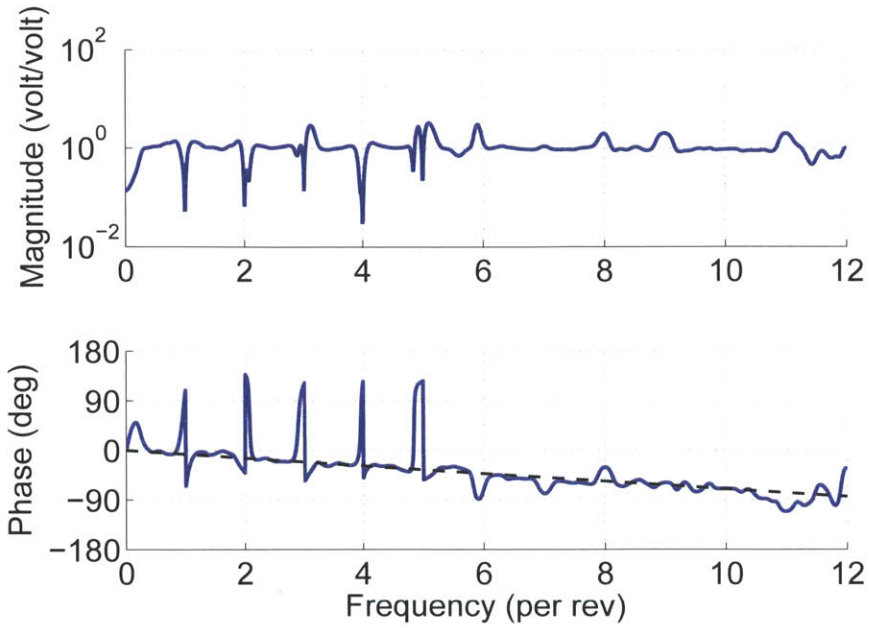

Figure 5-8: Frequency response of the transfer function $\widehat{H}$

our controllers is designed for a specific flight condition, and the performance will degrade when the flight condition changes. In order to design a harmonic disturbance rejection control law that is effective throughout the entire flight envelope, we need to know the behavior of the plant throughout the flight envelope. To obtain additional plant models at flight conditions that span most of the flight envelope, we use data generated by the Boeing Company using CAMRAD II from Johnson Aeronautics, a commercially available aeromechanical simulation program for helicopters [58].

5.3.1 Simulation Setup

The CAMRAD simulation is set up to replicate the wind tunnel system identification test of the SMART rotor, although for practical reasons, there are some differences. The input in the CAMRAD model is the collective flap displacement in degrees, instead of voltage to the amplifier. The output is the rotor normal force in lbs, which is consistent with the wind tunnel test. The data are produced at an interval of 0.001 sec, and the rotor frequency $\Omega = 392$ rpm is constant throughout the simulation. Due to limitations in the computer hardware and data resolution requirements, instead of using a continuous sinusoidal sweep from 0

Table 5.2: Sinusoidal sweep signal for CAMRAD simulation

Segment	1	2	3	4
Starting frequency (Hz)	0	18.7	38.7	58.7
Ending frequency (Hz)	21.307	41.3	61.3	79.998
Duration (sec)	21.308	22.6	22.6	21.299

Hz to 80 Hz, the simulation for each flight condition is performed in four segments. For each segment, the input data is a linear sinusoidal sweep with unit amplitude that starts at 1 second into the simulation. The starting frequency, ending frequency, and sweep duration of the input signal for each segment are shown in Table 5.2. The duration of each individual segment is 24.6 seconds. The overlaps in the starting and ending frequencies ensure the input signal contains enough power in the overlapped frequency ranges to properly excite the system.

5.3.2 CAMRAD Simulation Results

In our attempt to capture the plant behavior throughout the flight envelope, we used simulated rotor data at 21 different flight conditions that consisted of different combinations of the advance ratio (μ), the shaft angle α, and the blade loading coefficient C_T/σ, as shown in Table 5.3. For each flight condition, the simulation data from each individual segment are first regularized, and then the four segments are concatenated into one set of input-output data. The ETFE is then obtained by following the procedure outlined in Section 5.2.1.

To validate the CAMRAD model, simulations were conducted with the same flight conditions as the two flight conditions in the wind tunnel tests. The empirical transfer functions obtained from the wind tunnel data and the simulation data are shown in Figure 5-9. To be consistent with the simulation data, the wind tunnel empirical transfer functions were obtained using the measured flap deflection as the input. While the CAMRAD models have some qualitative similarity to the wind tunnel data generated models, the difference in magnitude and phase are significant, and we acknowledge that further development of the CAMRAD model is needed for better agreement with wind tunnel data.

The empirical transfer functions for all 21 flight conditions simulated in CAMRAD are shown in Figures 5-10, 5-11, 5-12, and 5-13. Within each figure, the empirical transfer

Table 5.3: CAMRAD simulation flight conditions

CAMRAD Case ID	μ	α (deg)	C_T/σ
F01D3C	0.15	-10.0	0.075
F01D3D	0.15	7.0	0.075
F01D3E	0.15	-3.7	0.075
F01D3F	0.15	-3.7	0.090
F01D3G	0.15	-10.0	0.040
F01D3H	0.15	-3.7	0.040
F01D5C	0.20	2.0	0.075
F01D7C	0.20	-5.5	0.075
F01D7D	0.20	-5.5	0.040
F01D7E	0.20	-5.5	0.090
F01D8C	0.20	-10.0	0.075
F01D6G	0.30	-9.1	0.040
F01D6E	0.30	-9.1	0.075
F01D6F	0.30	-9.1	0.090
F01D6H	0.30	-15.0	0.040
F01D6I	0.30	-15.0	0.070
F01D6J	0.30	-5.0	0.040
F01D6K	0.30	-5.0	0.100
F01D9C	0.375	-12.0	0.075
F01D9D	0.375	-12.0	0.040
F01D9E	0.375	-12.0	0.065

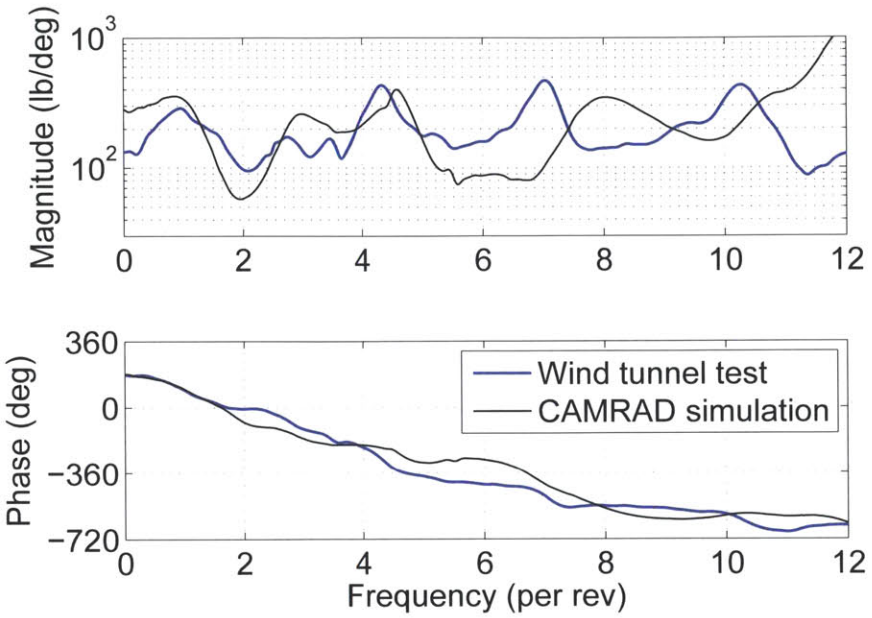

(a) Flight Condition 1

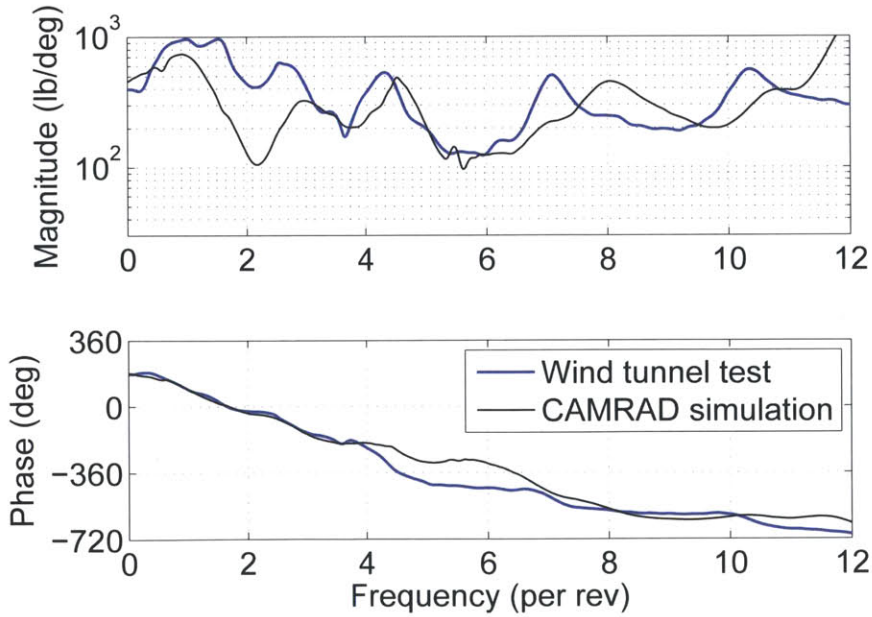

(b) Flight Condition 2

Figure 5-9: Comparison of ETFEs obtained from wind tunnel tests and CAMRAD simulations

functions represent flight conditions with different combinations of shaft angle α and blade loading coefficient C_T/σ, but the same value for the advance ratio μ. It can be seen that with the advance ratio μ fixed, there is not much variation in the transfer functions. However, there is a clear trend of increase in the magnitude of the transfer functions with increase in the advance ratio μ, which is consistent with the wind tunnel test result. Thus, the empirical transfer functions show that the behavior of the helicopter rotor is highly dependent on μ, and only weakly dependent on α and C_T/σ.

5.3.3 Parametric Models

For each flight condition simulated in CAMRAD, the simulation data were used to create a parametric model of the helicopter rotor. The parametric models are rational transfer functions obtained using the procedure described in Section 5.2.2. Four representative models, one for each value of the advance ratio μ used in the simulations, are shown in Figure 5-14. The plots show good agreement between the CAMRAD simulation results and the identified LTI parametric models, and are typical of all the parametric models obtained from the CAMRAD simulations.

5.4 Summary

In this chapter, we analyzed available wind tunnel test data of a full-scale rotor to identify the characteristics of the disturbance, quantify the effect of periodicity, and to obtain parametric models for control design. The data show that significant vibrations in the rotor normal direction exist at nearly all harmonic frequencies, not at just frequencies that are multiples of $N\Omega$, where N is the number of rotor blades, and Ω is the rotor frequency. Based on the magnitude of the empirical harmonic transfer functions, we conclude that the effect of periodicity on the dynamics of the rotor appears to be negligible, leading us to model the helicopter rotor as an LTI system, with the harmonic vibrations modeled as additive output disturbance. We obtained the parametric models of the helicopter rotor in the form of rational transfer functions. The parametric models enable us to apply our control synthesis methods developed in the previous chapters. Since the wind tunnel test data

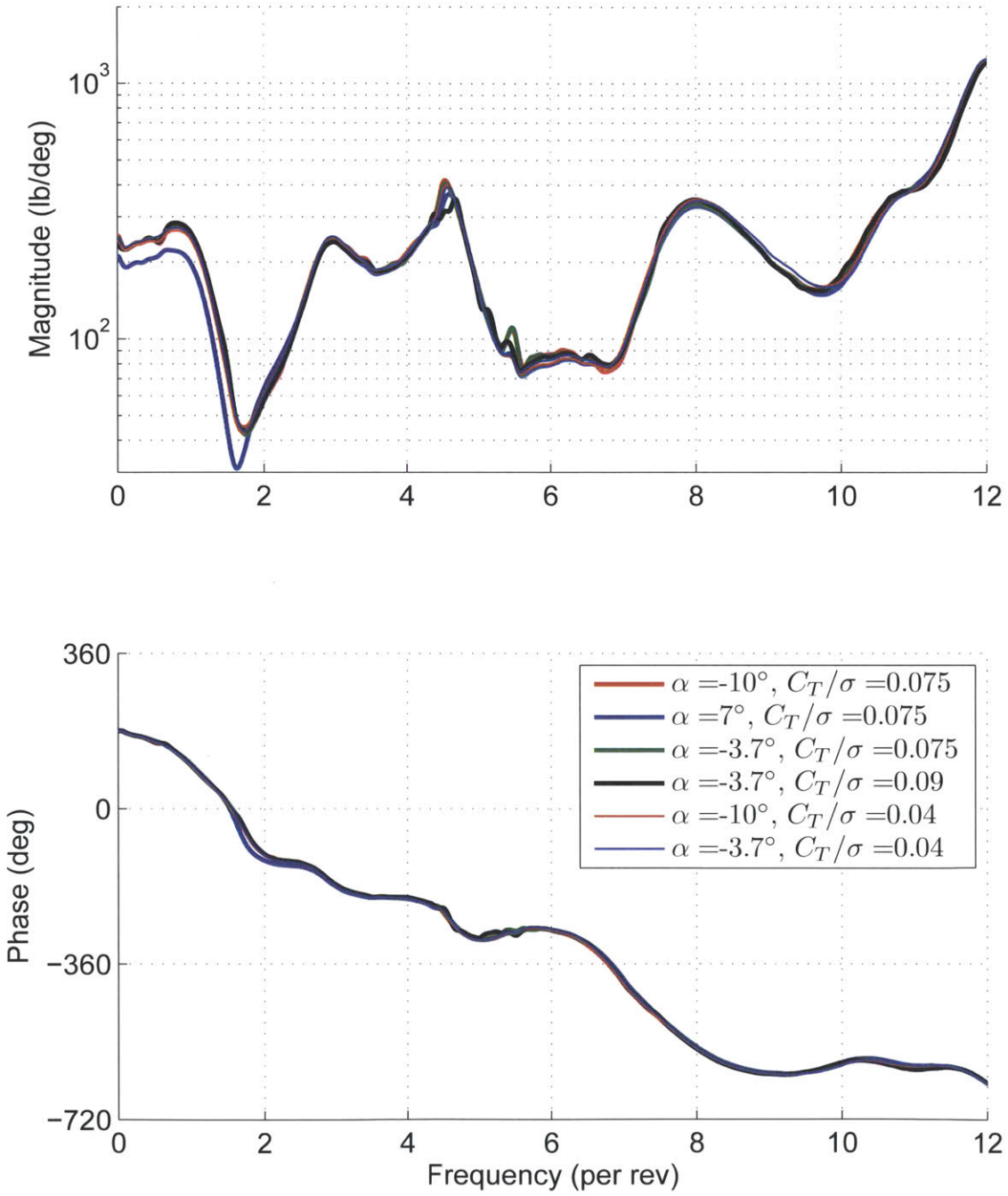

Figure 5-10: Empirical transfer functions with $\mu = 0.15$

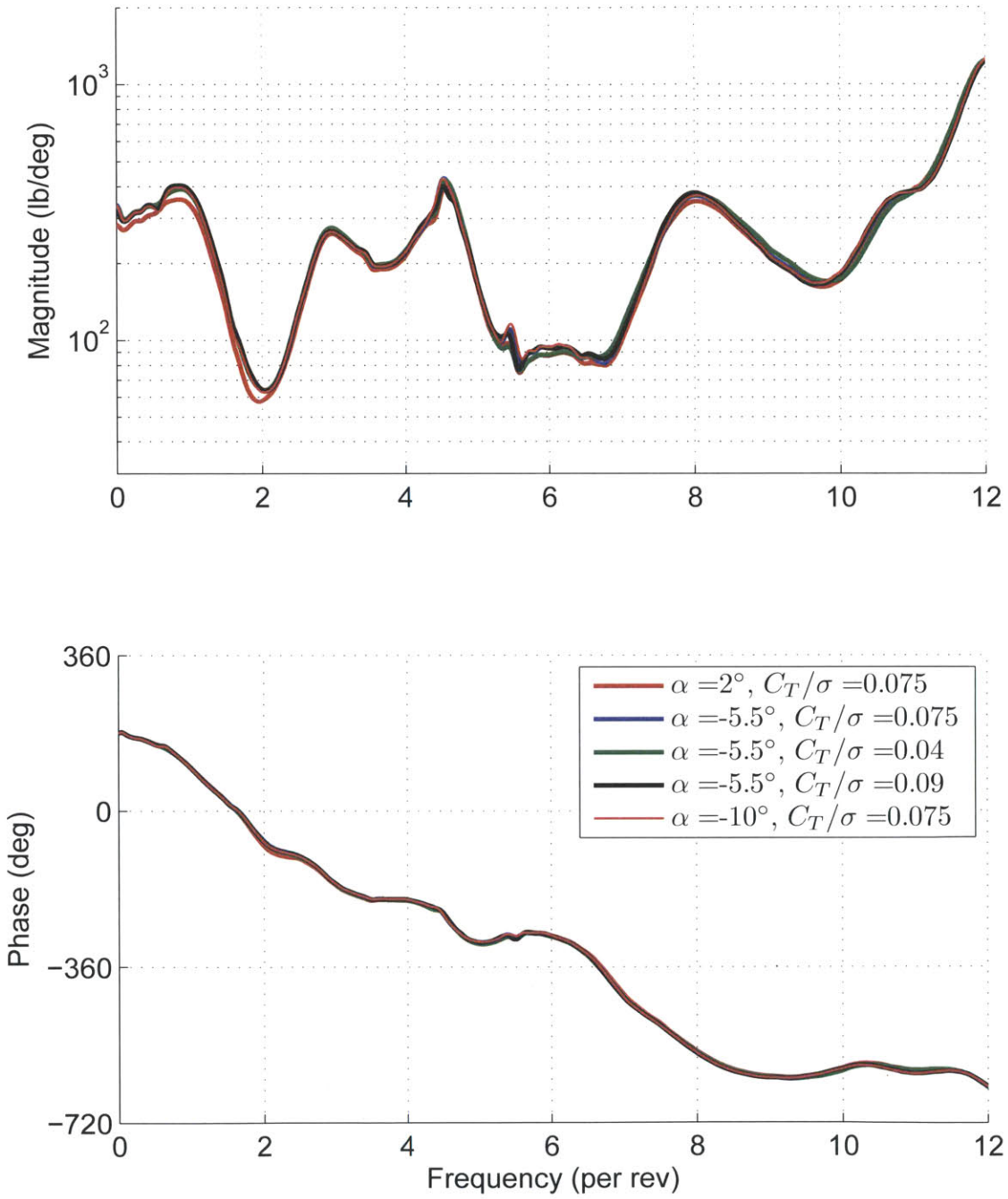

Figure 5-11: Empirical transfer functions with $\mu = 0.20$

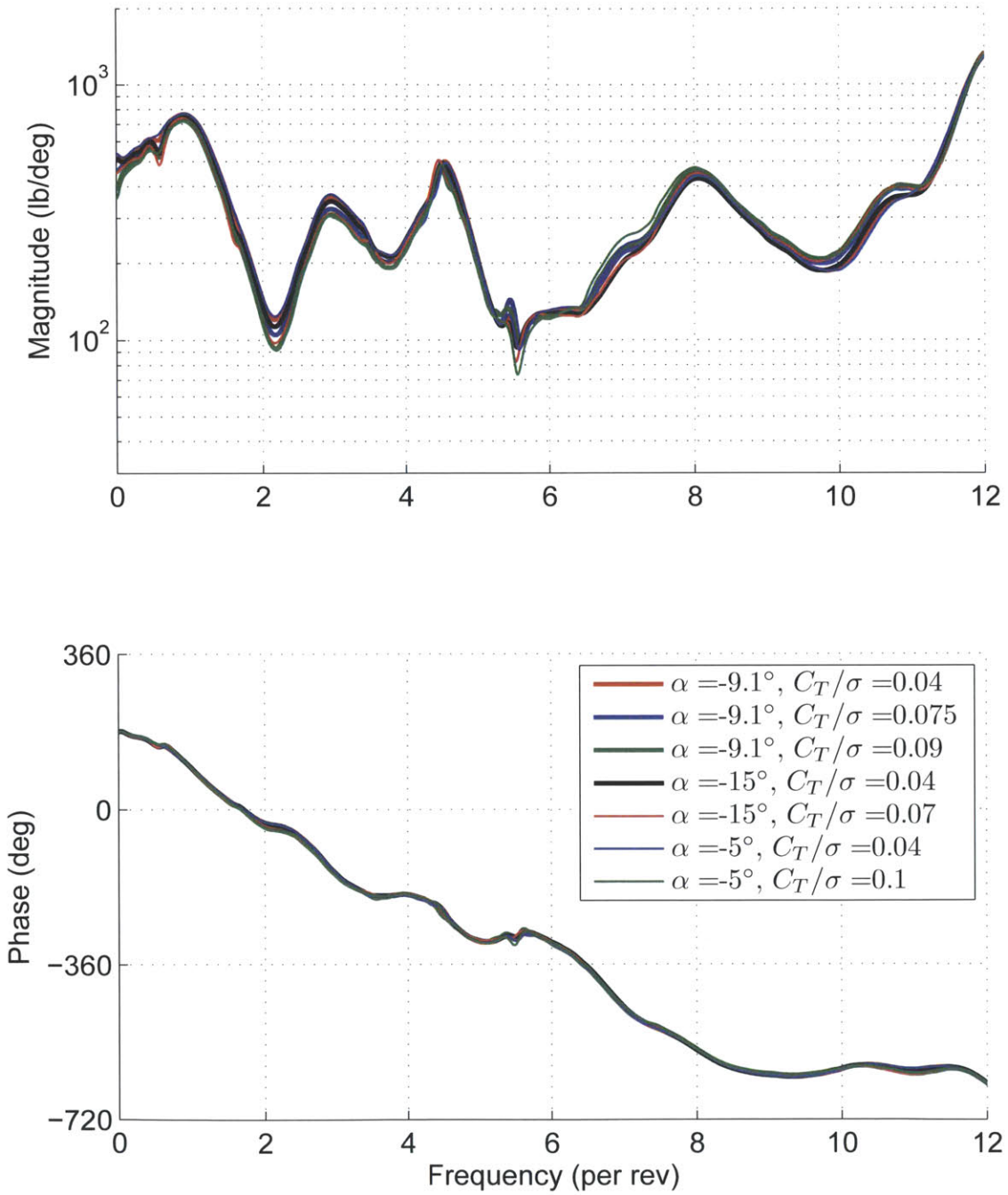

Figure 5-12: Empirical transfer functions with $\mu = 0.30$

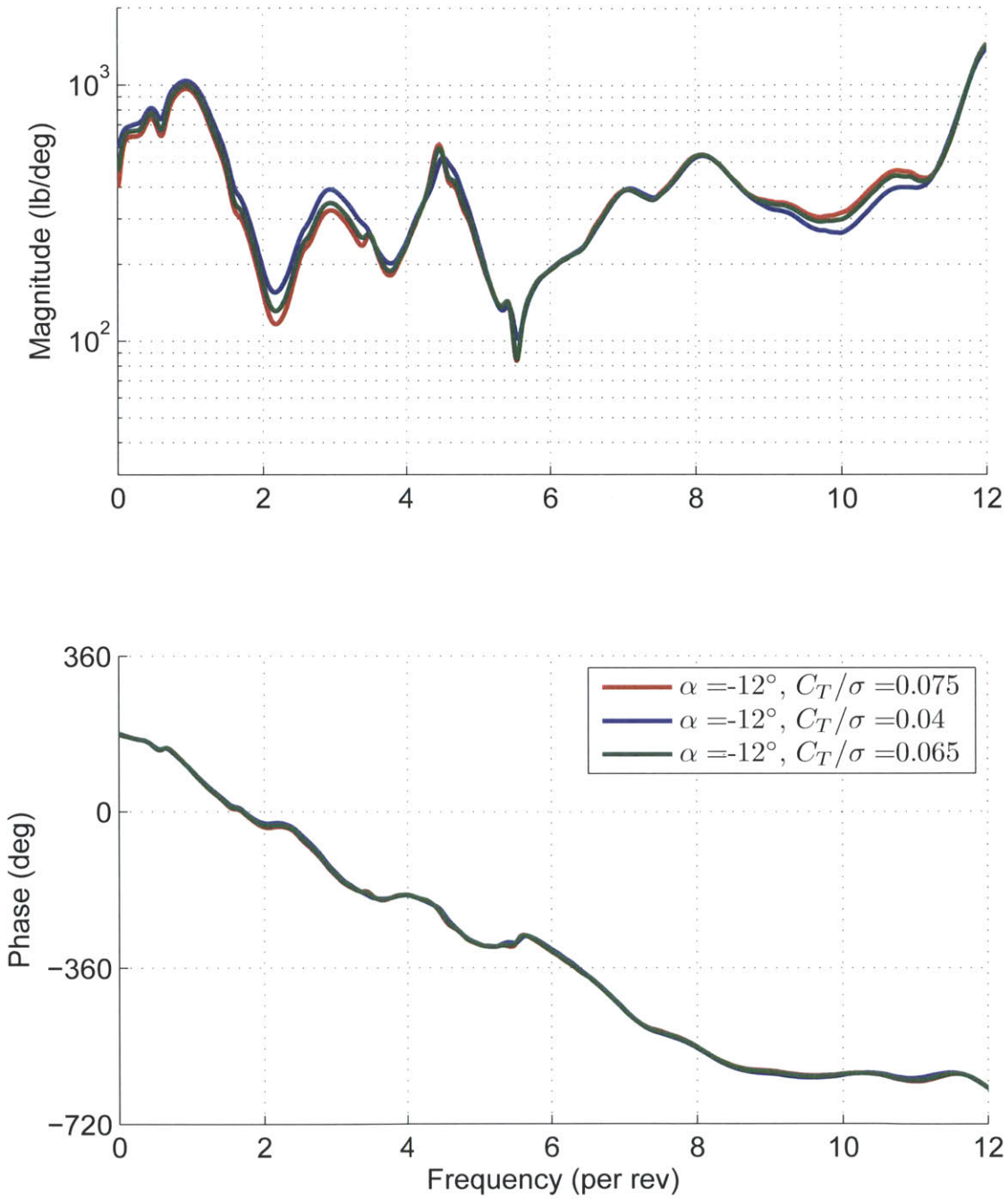

Figure 5-13: Empirical transfer functions with $\mu = 0.375$

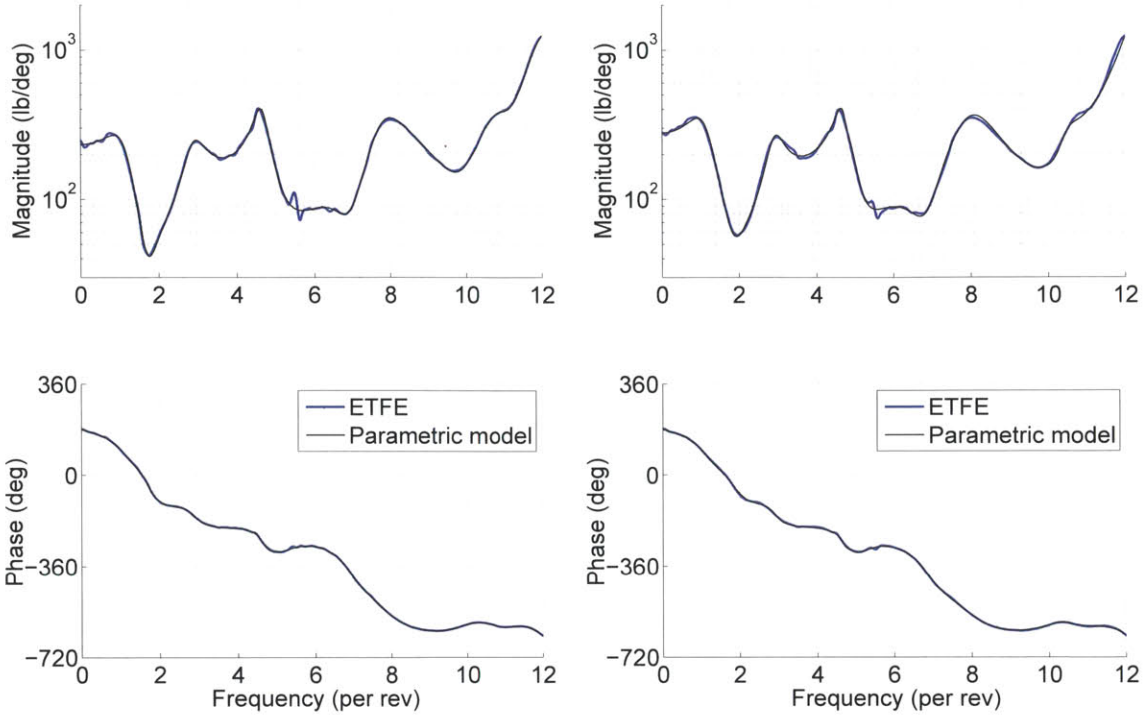

(a) CAMRAD Case ID F01D3E, $\mu = 0.15$, $\alpha = -3.7°$, $C_T/\sigma = 0.075$

(b) CAMRAD Case ID F01D5C, $\mu = 0.20$, $\alpha = 2.0°$, $C_T/\sigma = 0.075$

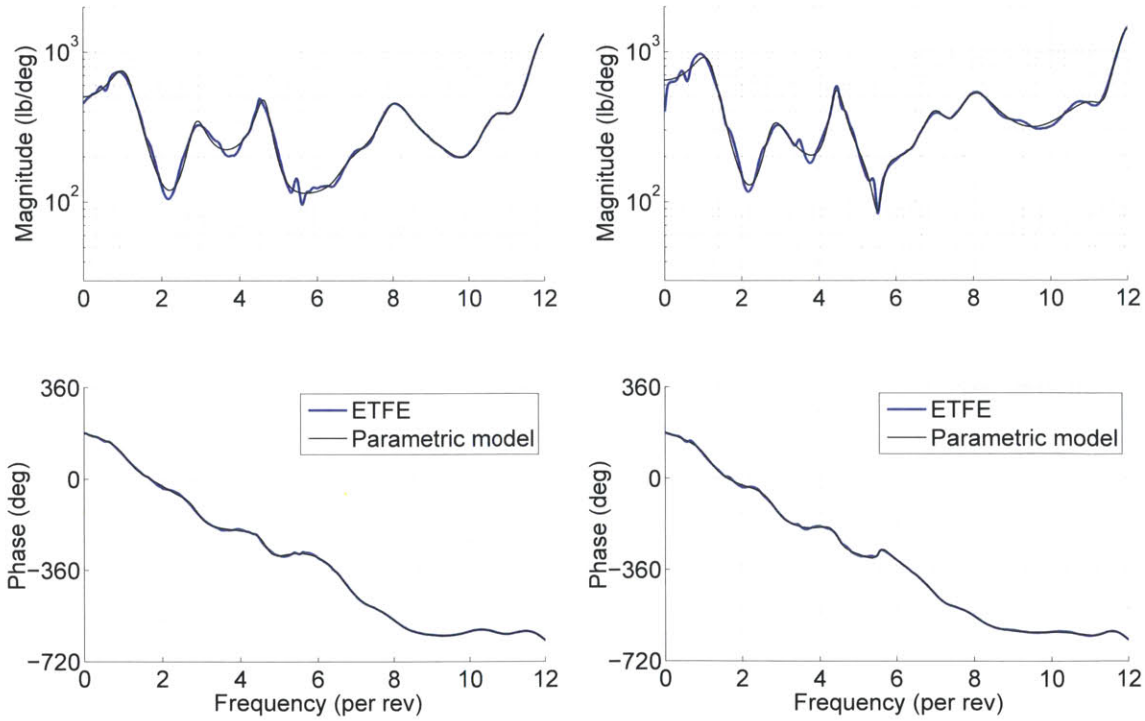

(c) CAMRAD Case ID F01D6E, $\mu = 0.30$, $\alpha = -9.1°$, $C_T/\sigma = 0.075$

(d) CAMRAD Case ID F01D9C, $\mu = 0.375$, $\alpha = -12.0°$, $C_T/\sigma = 0.075$

Figure 5-14: Comparison between ETFE and parametric model obtained from CAMRAD simulation data

were only for two flight conditions, in order to obtain models that span most of the flight envelope, we used nonlinear simulation data generated using CAMRAD. The CAMRAD simulation data span a range of advance ratio μ, rotor shaft angle α, and blade loading coefficient C_T/σ, and were processed and analyzed in a similar manner as the wind tunnel data. The analysis shows that the plant behavior is only weakly dependent on α and C_T/σ, but highly dependent on μ, which is in agreement with the wind tunnel results. In the next chapter, we use the LTI models identified from CAMRAD simulation data to develop a harmonic disturbance rejection control law for the entire flight envelope that is scheduled on μ only.

Chapter 6

Full Flight Envelope Harmonic Disturbance Rejection

The full-order and the fixed-order $\mathcal{H}_\infty$ higher harmonic control (HHC) methods developed in Chapters 3 and 4 are linear control methods intended for harmonic disturbance rejection at a fixed flight condition. In Chapter 5, we provided justification for using the linear control methods to suppress harmonic disturbances by showing that it is reasonable to model the helicopter rotor at a fixed flight condition as a linear time-invariant (LTI) system. However, a helicopter operates in varying flight condition, and the LTI models are in effect snapshots of a linear time-varying (LTV) plant at specific flight conditions, and offer no information on the dynamics of the plant in the transition between different flight conditions. Instead of developing an LTV model and employ LTV control techniques, we extend the fixed-order $\mathcal{H}_\infty$ control method to account for the variations in the plant dynamics at different flight conditions. In this chapter, we first present a simple extension of the fixed-order $\mathcal{H}_\infty$ controller synthesis for multiple plants, then we describe a gain-scheduled harmonic disturbance rejection control law for the entire flight envelope. The full flight envelope control law schedules the fixed-order $\mathcal{H}_\infty$ controllers designed for different values of the advance ratio μ, since the dynamics of the helicopter is most sensitive to μ. The gain-scheduled full flight envelope control law is implemented in two different nonlinear simulations to demonstrate its effectiveness in harmonic disturbance rejection during the transitions between different flight conditions.

6.1 Harmonic Disturbance Rejection for Multiple Plants

The metrics we used to define performance in harmonic disturbance rejection, the bandwidth ω_B and peak sensitivity $S_{\max}$, are in effect also measures of robustness of the controller. The controller's robustness to changes in the harmonic disturbance is addressed by the controller bandwidth ω_B. The peak sensitivity $S_{\max}$ is an indicator of the controller's stability robustness to plant variation, since it is related to both gain margin and phase margin. However, gain and phase margins do not address the robustness of the controller performance with respect to changes in the plant dynamics. In this section, we use the fixed-order $\mathcal{H}_\infty$ control method to design a controller for multiple plants, and examine the achievable performance using a single controller for different flight conditions.

6.1.1 Simultaneous Harmonic Disturbance Rejection

The controller synthesis methods developed in Chapter 3 and Chapter 4 are only applicable to a single LTI plant model, so they are suitable for any one of the plant models obtained in the previous chapter. In this section, we demonstrate a method to design a single fixed-order harmonic disturbance controller based on multiple LTI plant models of the helicopter rotor. The method is based on the fixed-order $\mathcal{H}_\infty$ controller synthesis procedure described in Chapter 4, with the main difference being a simple modification to the cost function, and the associated changes to the gradient.

Denoting the available LTI plant models for control design by $G_k(s)$, $k = 1, 2, \ldots, N$, the objectives of a single controller $K(s)$ for multiple plant models are to maximize the bandwidth and minimize the peak sensitivity in all the sensitivity functions

$$S_k(s) = (1 - G_k(s)K(s))^{-1}, \quad k = 1, 2, \ldots, N \tag{6.1}$$

The bandwidth ω_B and peak sensitivity $S_{\max}$ achieved by the single controller $K(s)$ is quantified by a weighting filter $W(s)$ for all plant models as in

$$S_k(s) \leq W(s), \quad k = 1, 2, \ldots, N \tag{6.2}$$

The controller $K(s)$ is obtained by modifying the fixed-order $\mathcal{H}_\infty$ control synthesis procedure described in Chapter 4. The main modification is that the cost function is a summation of the cost functions for individual plant models

$$J = \sum_{k=1}^{N} J_k \tag{6.3}$$

where J_k is the fixed-order $\mathcal{H}_\infty$ synthesis cost function for the plant $G_k(s)$ with weighting filter $W(s)$, and controller $K(s)$. The gradient of the cost function J is similarly modified as

$$\frac{\partial J}{\partial \Theta} = \sum_{k=1}^{N} \frac{\partial J_k}{\partial \Theta} \tag{6.4}$$

where Θ is a vector containing the parameter of the fixed-order controller $K(s)$. The optimization procedure for obtaining the fixed-order controller is essentially the same as described in Chapter 4, with the cost function given by Equation (6.3), and the gradient given by Equation (6.4).

The initial parameter vector Θ is obtained from the baseline HHC controller for any $G_k(s),\ k = 1, 2, \ldots, N$, or from the baseline controller for the average plant

$$G_{\text{avg}} = \frac{1}{N} \sum_{k=1}^{N} G_k(s) \tag{6.5}$$

For our optimization procedure, the initial controller must stabilize each $G_k(s),\ k = 1, 2, \ldots, N$. For the low bandwidth cases, the baseline HHC algorithm can typically be used to generate the initial controller. In the case that the initial controller does not offer sufficient bandwidth, the weighting filter can be updated on bandwidth instead of peak sensitivity within each iteration step of the optimization. Once the desired bandwidth is reached, the optimization procedure can be repeated with weighting filter updated on peak sensitivity to further improve controller performance.

The feasibility of the problem can be determined from the phase of the plants at the harmonic frequencies. Since HHC can be interpreted as phase stabilization at the harmonic frequencies to be attenuated, the phases of all the plant models at these harmonic frequen-

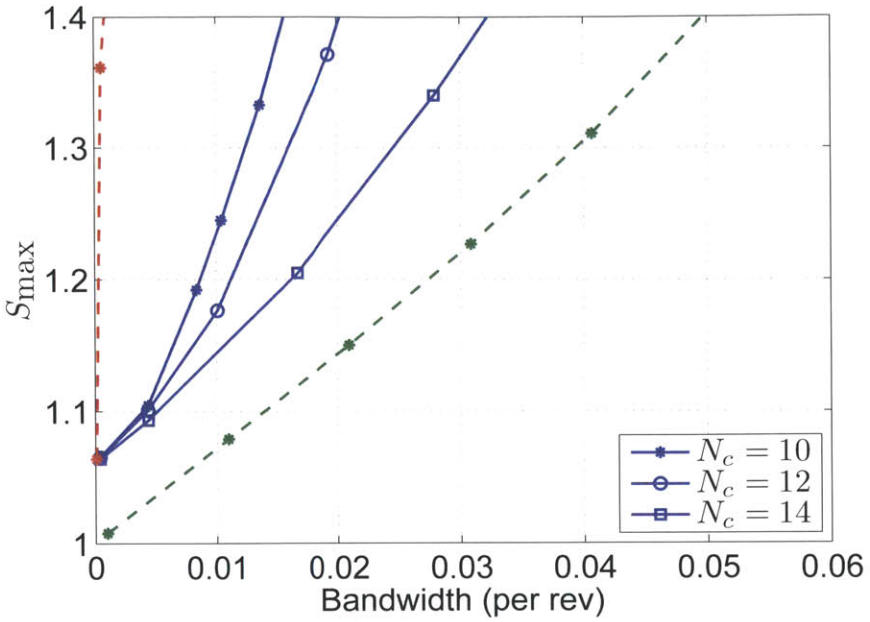

Figure 6-1: Performance of a single fixed-order $\mathcal{H}_\infty$ controller for both Flight Condition 1 and Flight Condition 2

cies must be in a 180° sector. Of course, feasibility does not imply any performance guarantees, and the performance of the single controller would degrade with larger variation in phases at the harmonic frequencies.

6.1.2 Simultaneous Harmonic Disturbance Rejection Performance

The achievable performance of a single fixed-order $\mathcal{H}_\infty$ controller of various orders N_c designed for both Flight Condition 1 and Flight Condition 2 is shown in Figure 6-1. The Pareto frontier for Flight Condition 1 using a 10th order fixed-order $\mathcal{H}_\infty$ controller is shown in a green dashed line for comparison. The performance achieved by using the same 10th order fixed-order $\mathcal{H}_\infty$ controller for Flight Condition 2 is shown in a red dashed line. Considering the performance for Flight Condition 1 only, the fixed-order controller designed specifically for Flight Condition 1 offers much better performance than the single fixed-order $\mathcal{H}_\infty$ controller designed for both flight conditions. However, as shown by the red dashed line, the fixed-order $\mathcal{H}_\infty$ controller designed for Flight Condition 1 is not a viable controller for Flight Condition 2.

Although the single fixed-order $\mathcal{H}_\infty$ controller offers better performance than the case

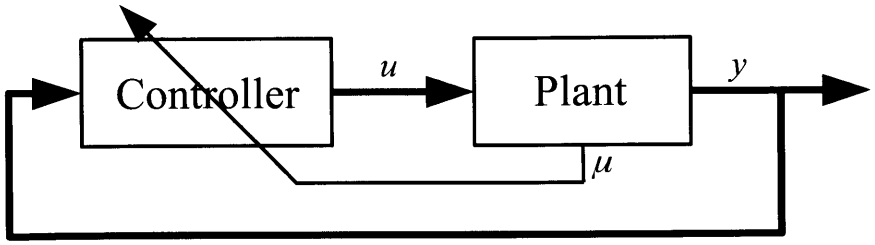

Figure 6-2: Feedback structure for gain-scheduled controller

of controller and plant mismatch, it nevertheless compromises the performance. The reduced performance of the single fixed-order harmonic disturbance rejection controller is a direct result of the large variation in rotor dynamics between Flight Condition 1 and Flight Condition 2. In the next section, we use the single fixed-order controller approach to cover the small variations in the dynamics at a constant advance ratio, while accounting for the large variations in the dynamics by scheduling a series of fixed-order controllers designed for different values of advance ratios.

6.2 Gain-Scheduled Harmonic Disturbance Rejection Controller

In this section, we develop a gain-scheduled approach to achieve harmonic disturbance rejection for the entire flight envelope using the plant models obtained from the CAMRAD simulations. We use the advance ratio μ as the scheduling variable, since the dynamics of the helicopter rotor is most sensitive to variations in μ. We account for the slight variations in the plant dynamics due to variations in α and C_T/σ at a fixed μ by using the single fixed-order $\mathcal{H}_\infty$ controller for multiple plants approach of Section 6.1. As in the previous chapters, the gain-scheduled controller is designed to reject the first five harmonics, *i.e.*, $n_i = i, i = 1, 2, 3, 4, 5$.

The block diagram of the gain-scheduled feedback control system is shown in Figure 6-2. In addition to the measured hub normal force y, the controller requires the value of the advance ratio μ. We exploit the inherent structure of the higher harmonic controller embedded in the fixed-order $\mathcal{H}_\infty$ controller to obtain a decomposition suitable for

Table 6.1: Advance ratios used for control design

j	μ_j
1	0.15
2	0.20
3	0.30
4	0.375

controller scheduling. The decomposition also allows the implementation of the demodulation/modulation scheme developed by Hall and Wereley [44], and the associated anti-windup algorithm developed by Shin, Cesnik and Hall [88]. The demodulation/modulation implementation is necessary in the case that azimuthal position of the rotor is used as the independent variable in our controller synthesis procedure. A benefit of using the azimuthal position as the independent variable is that the disturbance frequency will always be at integral multiples of the fundamental rotor frequency.

6.2.1 Fixed-Order Controllers at Constant Advance Ratios

The analysis of the simulation data shows that while the helicopter rotor dynamics is most sensitive to variations in the advance ratio μ, it is not completely independent of the rotor shaft angle α, and the blade loading coefficient C_T/σ. We address the variations due to changes in μ by scheduling the controller on μ. In this section, we account for the variations in α and C_T/σ by designing a controller based on all available models for a fixed value of μ.

For each value of μ in Table 6.1, LTI plant models obtained from CAMRAD simulations are available at different values of rotor shaft angle α, and blade loading coefficient C_T/σ. Instead of selecting the controller for a specific plant model to be used in the gain-scheduled controller, we use a single fixed-order $\mathcal{H}_\infty$ controller designed using all available models at the specific value of μ. Denoting the LTI plant models available at $\mu = \mu_j$ by G_{jk}, $k = 1, 2, \ldots, N_j$, where N_j is the total number of LTI plant models at $\mu = \mu_j$, the cost function and the gradient for the single fixed-order $\mathcal{H}_\infty$ controller, as given in Section 6.1,

are

$$J_j = \sum_{k=1}^{N_j} J_{jk} \tag{6.6}$$

$$\frac{\partial J_j}{\partial \Theta} = \sum_{k=1}^{N_j} \frac{\partial J_{jk}}{\partial \Theta} \tag{6.7}$$

The procedure to optimize the cost function in Equation (6.6) using the gradient in Equation (6.7) is discussed in Section 6.1, and in Chapter 4. The resulting Pareto frontiers for the fixed-order controllers designed for $\mu = 0.15, 0.20, 0.30, 0.375$, are shown in Figure 6-3 and Figure 6-4. The fixed-order $\mathcal{H}_\infty$ controller for $\mu = \mu_j$ provides adequate performance for all plant models with $\mu = \mu_j$, regardless of the values for α and C_T/σ, since the dynamics of the helicopter rotor is only strongly dependent on the advance ratio μ.

6.2.2 Controller Blending

In this section, we incorporate the fixed-order $\mathcal{H}_\infty$ controllers designed for different values of μ into a gain-scheduled control law to attenuate harmonic disturbances for the entire flight envelope. We schedule the controller by blending the outputs of the fixed-order controllers based on the value of μ. For the current value of μ, with $\mu_j \leq \mu < \mu_{j+1}$, the control signal from the gain-scheduled controller is obtained as

$$U(s;\mu) = (1 - \alpha(\mu))\, U_j(s) + \alpha(\mu) U_{j+1}(s) \tag{6.8}$$

where $U_j(s)$ is the output of the controller $K_j(s)$ designed for $\mu = \mu_j$, $U_{j+1}(s)$ is the output of the controller $K_{j+1}(s)$ designed for $\mu = \mu_{j+1}$, and the blending function α is given by

$$\alpha(\mu) = \frac{\mu - \mu_j}{\mu_{j+1} - \mu_j}, \quad \mu_j \leq \mu < \mu_{j+1} \tag{6.9}$$

When the value of μ in Equation (6.8) moves out of the interval $[\mu_j,\ \mu_{j+1})$, another control signal must be available for the blending of controller output to continue. Instead of switching on the individual controller $K_{j-1}(s)$ or $K_{j+2}(s)$ as needed, we keep all individual

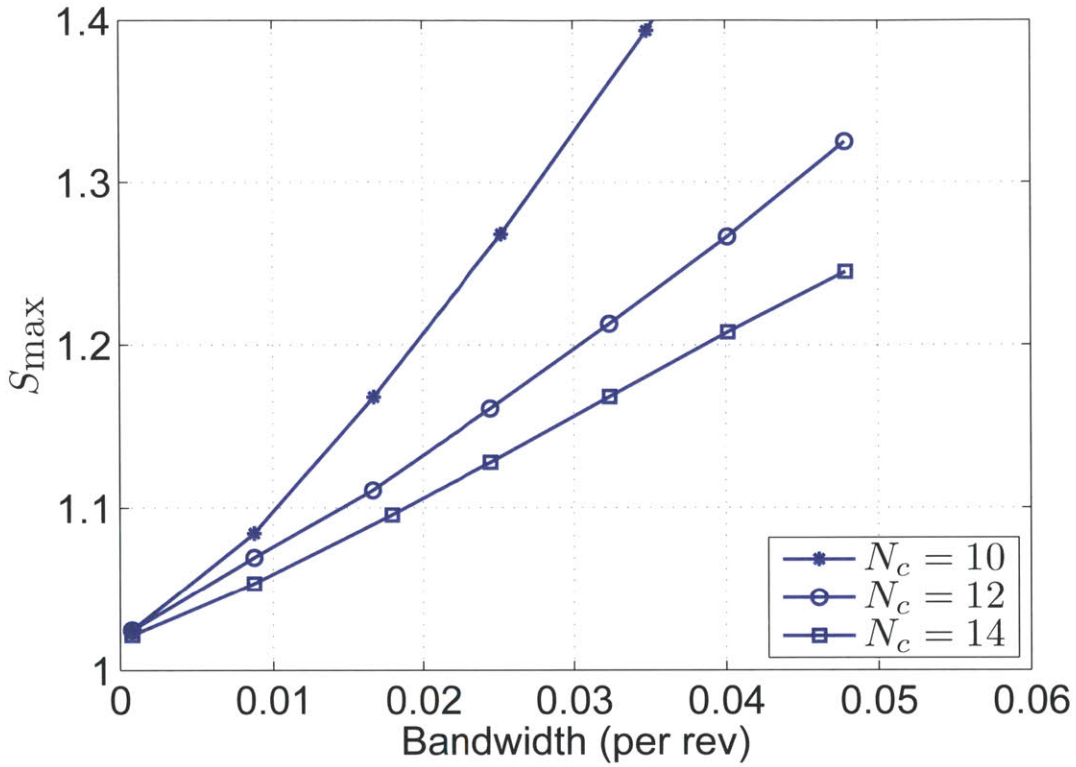

(a) $\mu = 0.15$

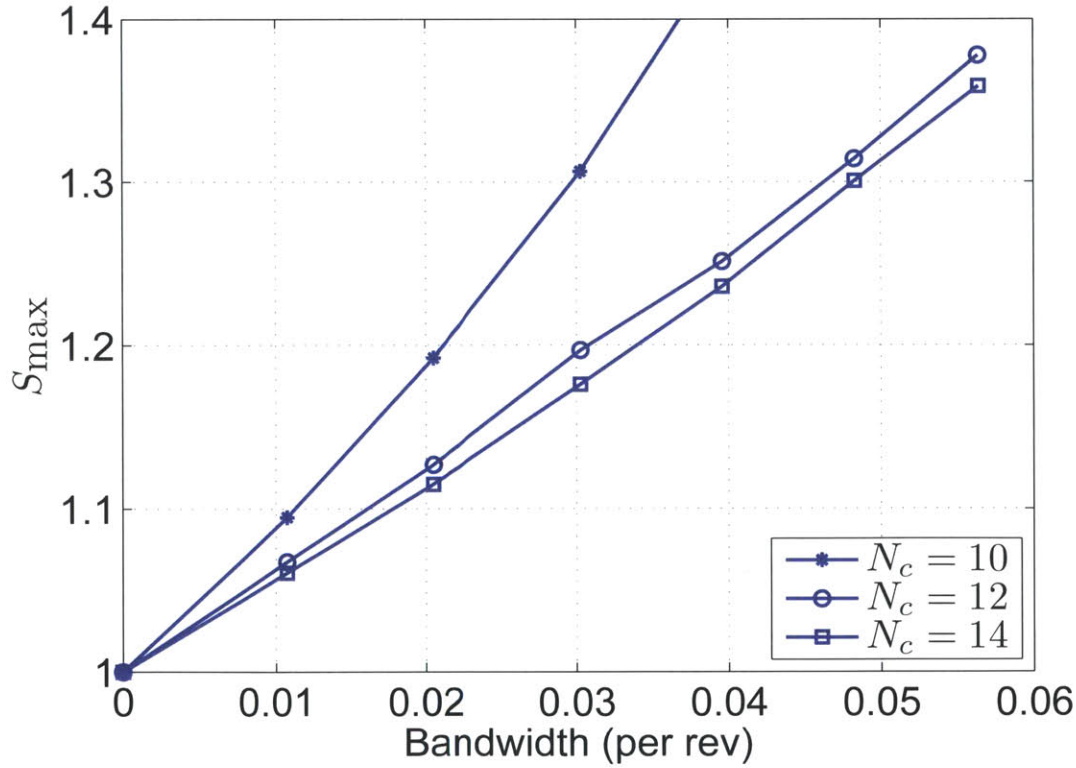

(b) $\mu = 0.20$

Figure 6-3: Pareto frontiers for single fixed-order $\mathcal{H}_\infty$ controller designed for various values of μ

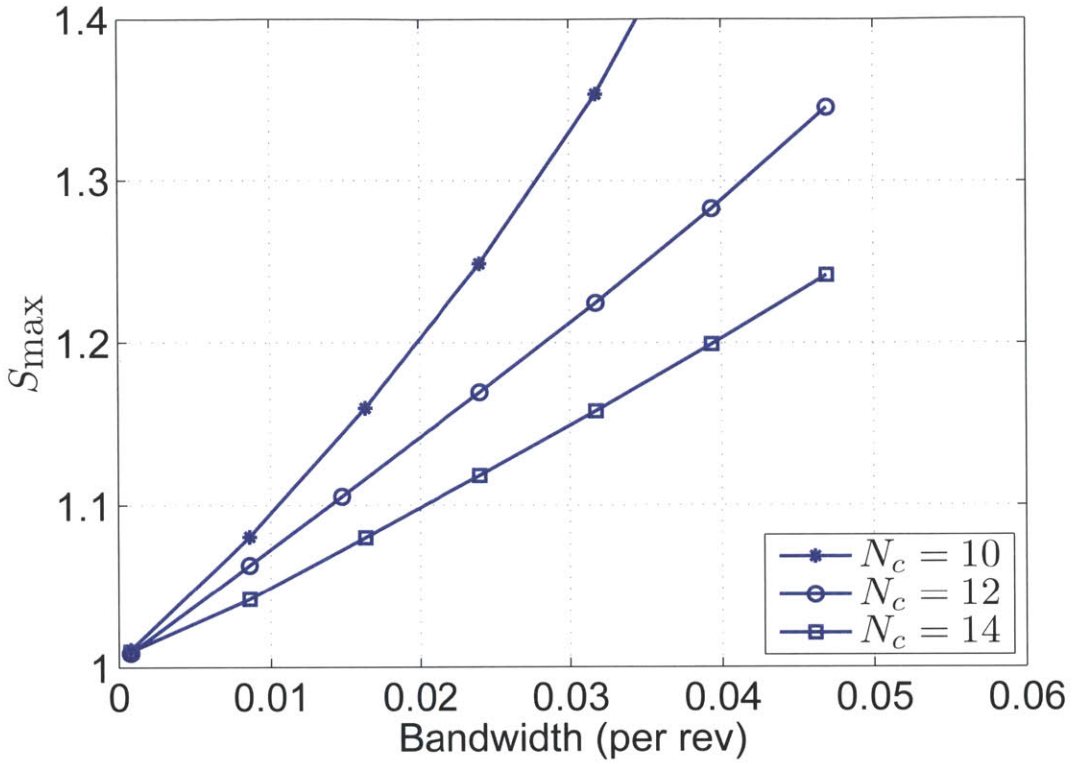

(a) $\mu = 0.30$

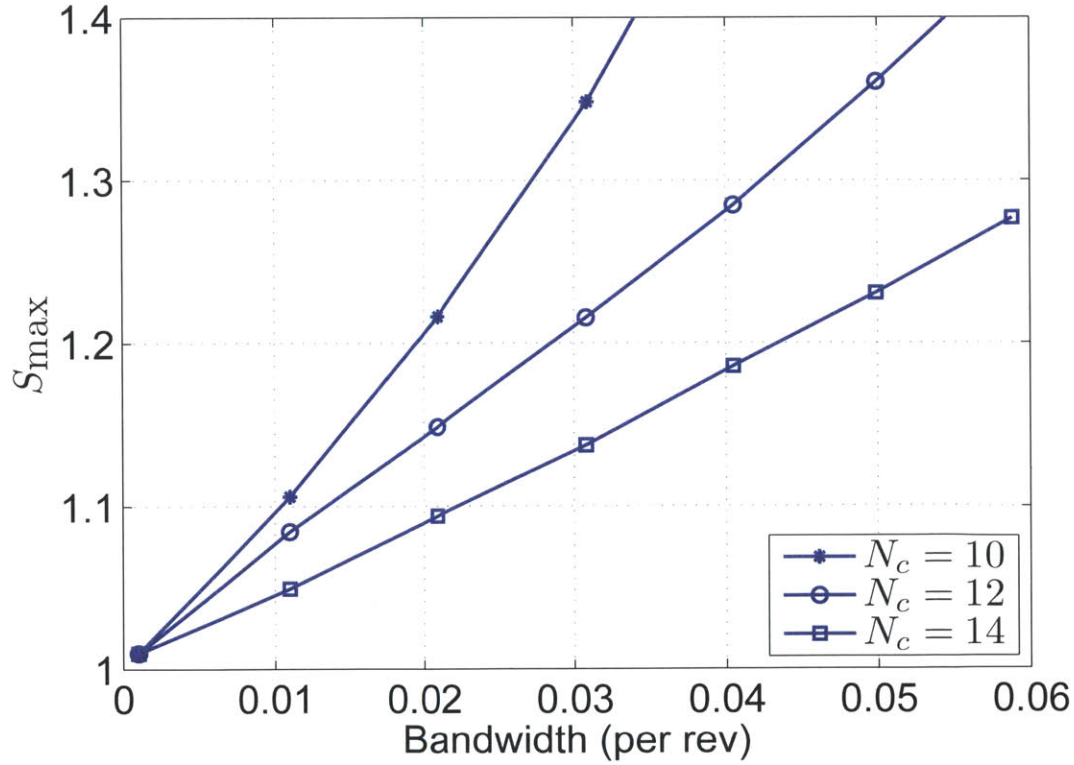

(b) $\mu = 0.375$

Figure 6-4: Pareto frontiers for single fixed-order $\mathcal{H}_\infty$ controller designed for various values of μ

controllers online and blend their control signals. In the case that controllers $K_j(s)$ are designed for $\mu_j,\ j = 1, 2, \ldots, N_\mu$, the blending rule is

$$U(s;\mu) = \sum_{j=1}^{N_\mu} \alpha_j(\mu) U_j(s) \tag{6.10}$$

where the blending functions are given by

$$\alpha_1(\mu) = \begin{cases} 1 & \mu < \mu_1 \\ \frac{\mu_2 - \mu}{\mu_2 - \mu_1} & \mu_1 \leq \mu < \mu_2 \\ 0 & \mu \geq \mu_2 \end{cases} \tag{6.11}$$

$$\alpha_j(\mu) = \begin{cases} 0 & \mu < \mu_{j-1} \\ \frac{\mu - \mu_{j-1}}{\mu_j - \mu_{j-1}} & \mu_{j-1} \leq \mu < \mu_j \\ \frac{\mu_{j+1} - \mu}{\mu_{j+1} - \mu_j} & \mu_j \leq \mu < \mu_{j+1} \\ 0 & \mu \geq \mu_{j+1} \end{cases} \quad j = 2, 3, \ldots, N_\mu - 1 \tag{6.12}$$

$$\alpha_{N_\mu}(\mu) = \begin{cases} 0 & \mu < \mu_{N_\mu - 1} \\ \frac{\mu - \mu_{N_\mu}}{\mu_{N_\mu} - \mu_{N_\mu - 1}} & \mu_{N_\mu - 1} \leq \mu < \mu_{N_\mu} \\ 1 & \mu \geq \mu_{N_\mu} \end{cases} \tag{6.13}$$

The blending of all the individual fixed-order controllers ensures the control signal is continuous, resulting in bumpless transfers between the different intervals of μ during operation. In our case, we use four values of μ that are given in Table 6.1 to span the entire flight envelope, and the four blending functions are shown in Figure 6-5,

6.2.3 Blended Model and Blended Controller

The controller blending outlined above linearly interpolates the output of the fixed-order controllers designed for specific values of μ. Ideally, stability and performance of the gain-scheduled controller should be verified with a suitable model of the helicopter rotor that captures the dynamics as a function of μ. Because we do not have a nonlinear model that

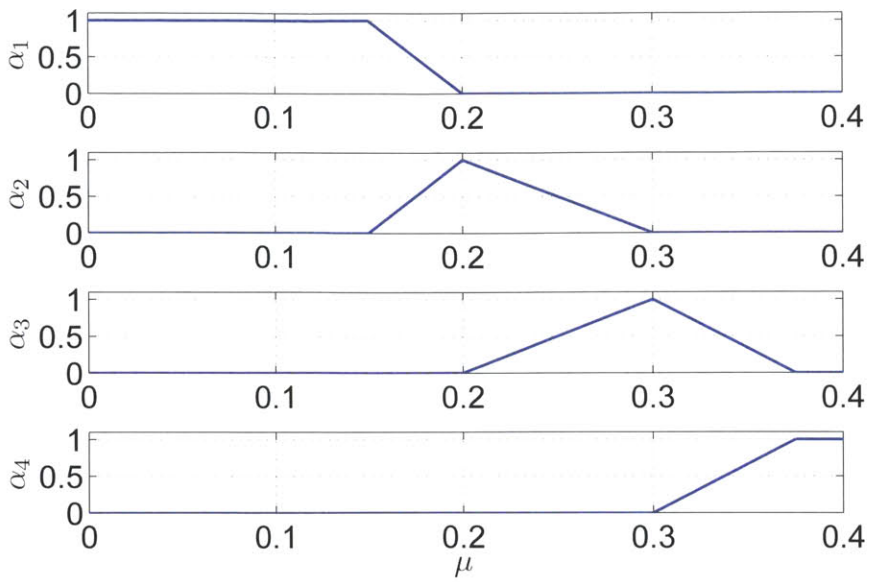

Figure 6-5: Blending functions for gain-scheduling control law

describes the helicopter rotor as it performs a maneuvering flight with a change in μ, we cannot verify whether the gain-scheduled controller even stabilizes the closed-loop system, much less provide the level of performance that can be achieved .

From a practical perspective, the blended controller at an intermediate value of μ should at a minimum not destabilize the LTI plant at the same value of μ. Since we do not have any additional LTI plant models of the helicopter rotor at values of μ besides those shown in Table 6.1, a possible method to obtain additional LTI models at intermediate values of μ is to apply the blending rule

$$G(s;\mu) = \sum_{j=1}^{4} \alpha_j(\mu) G(s;\mu_j) \tag{6.14}$$

where $\alpha_j(\mu),\ j = 1,2,3,4$, are given by Equations (6.11), (6.12), (6.13), and $G(s;\mu_j)$ is the LTI model of the helicopter rotor at $\mu = \mu_j$. As shown if Figure 6-6a, the transfer function of the blended plant at $\mu = 0.20$ is relatively close to the plant model at $\mu = 0.20$ identified from the CAMRAD simulation. However, the blended plant for $\mu = 0.30$, shown in Figure 6-6b, is not very close to the actual plant models identified from the CAMRAD simulations.

Since we have the LTI models of the helicopter rotor at values of $\mu = \mu_j$ shown in Table

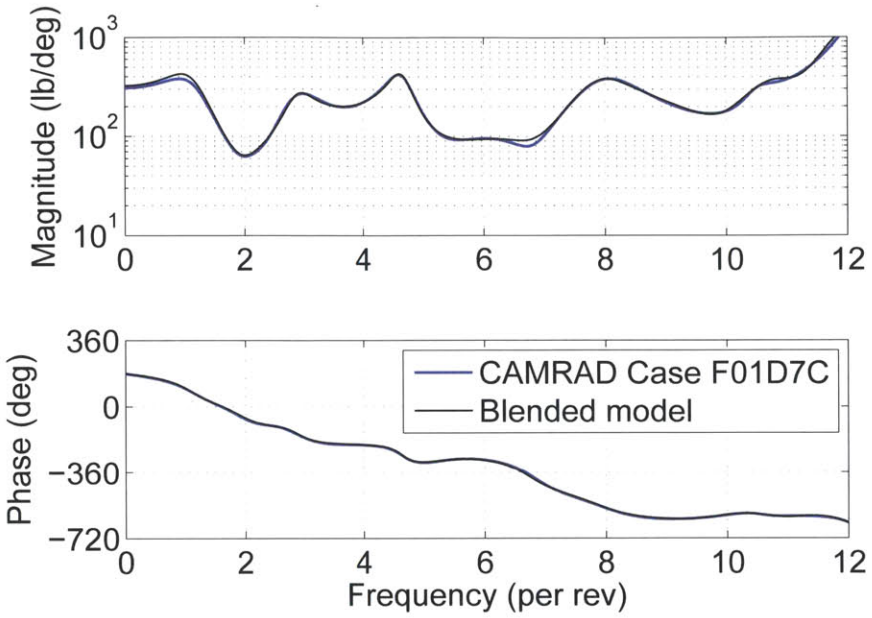

(a) Flight condition with $\mu = 0.20$

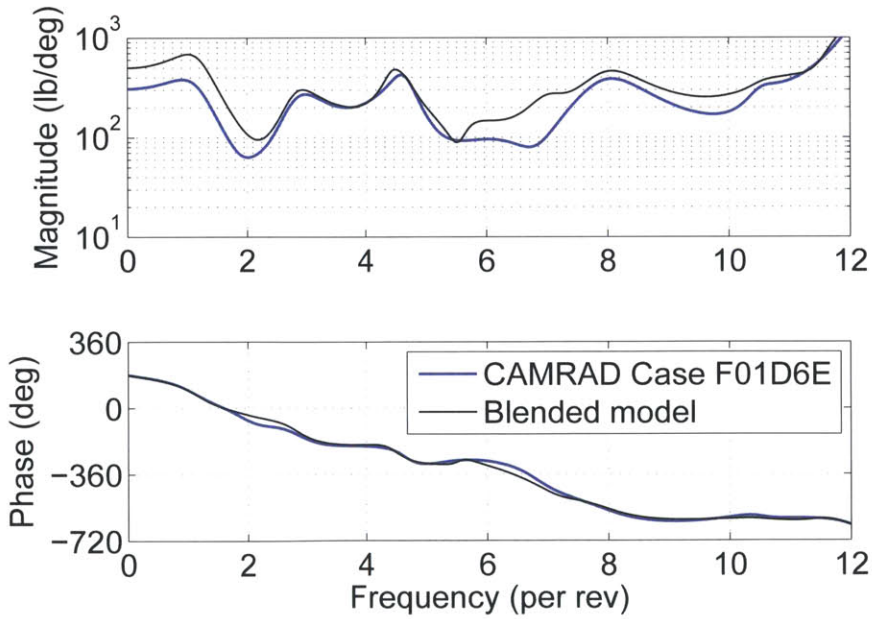

(b) Flight condition with $\mu = 0.30$

Figure 6-6: Transfer function comparisons between blended model and model directly identified from CAMRAD simulations

6.1, we can check the performance of the closed-loop system at $\mu = 0.20$ by blending the controllers designed for $\mu = 0.15$ and $\mu = 0.30$. Similarly, the performance at $\mu = 0.30$ can be checked by blending the controllers designed for $\mu = 0.20$ and $\mu = 0.375$. Figures 6-7a and 6-7b show the performance of the blended controller on the helicopter plant for $\mu = 0.20$ (CAMRAD Case F01D7C) and $\mu = 0.30$ (CAMRAD Case F01D6E), respectively. The blending was accomplished by using the corresponding fixed-order controllers used to generate the Pareto frontiers in Equation (6.8). Note that blending fixed-order controllers of higher order did not necessarily produce improved performance.

The discrepancy between the blended model and identified model at $\mu = 0.30$ indicates that additional plant models at smaller intervals of μ are required for accurate model blending. The relatively poor performance of the blended controllers suggests that the controller used for interpolation must have adequate performance at the intermediate values of μ where plant models are not available.

6.2.4 Gain-Scheduled Controller Structure

The structure of the controller in the fixed-order $\mathcal{H}_\infty$ synthesis procedure of Chapter 4 consists of a dynamic filter in parallel with a harmonic disturbance rejection filter. The parallel structure allows us to use the baseline HHC algorithm to generate an initial controller for the optimization. For the purpose of implementation in the gain-scheduled controller, the fixed-order $\mathcal{H}_\infty$ controllers for $\mu = \mu_j$, $j = 1, 2, 3, 4$, are decomposed in series as

$$K_j(s) = \frac{B_j(s)}{A_j(s)} = \frac{B_{\mathrm{h}_j}(s)}{A_{\mathrm{h}_j}(s)} \frac{B_{\mathrm{d}_j}(s)}{A_{\mathrm{d}_j}(s)} = K_{\mathrm{h}_j}(s) K_{\mathrm{d}_j}(s), \quad j = 1, 2, 3, 4 \tag{6.15}$$

where the harmonic disturbance rejection filter $K_{\mathrm{h}_j}(s)$ contains all the $j\omega$-axis poles of $K_j(s)$ that correspond to the frequencies of the harmonic disturbances to be attenuated, and the dynamic filter $K_{\mathrm{d}_j}(s)$ contains the remaining poles of $K_j(s)$. The zeros of $K_{\mathrm{h}_j}(s)$ and $K_{\mathrm{d}_j}(s)$ are chosen so that the polynomials $B_{\mathrm{h}_j}(s)$ and $B_{\mathrm{d}_j}(s)$ have real coefficients. In

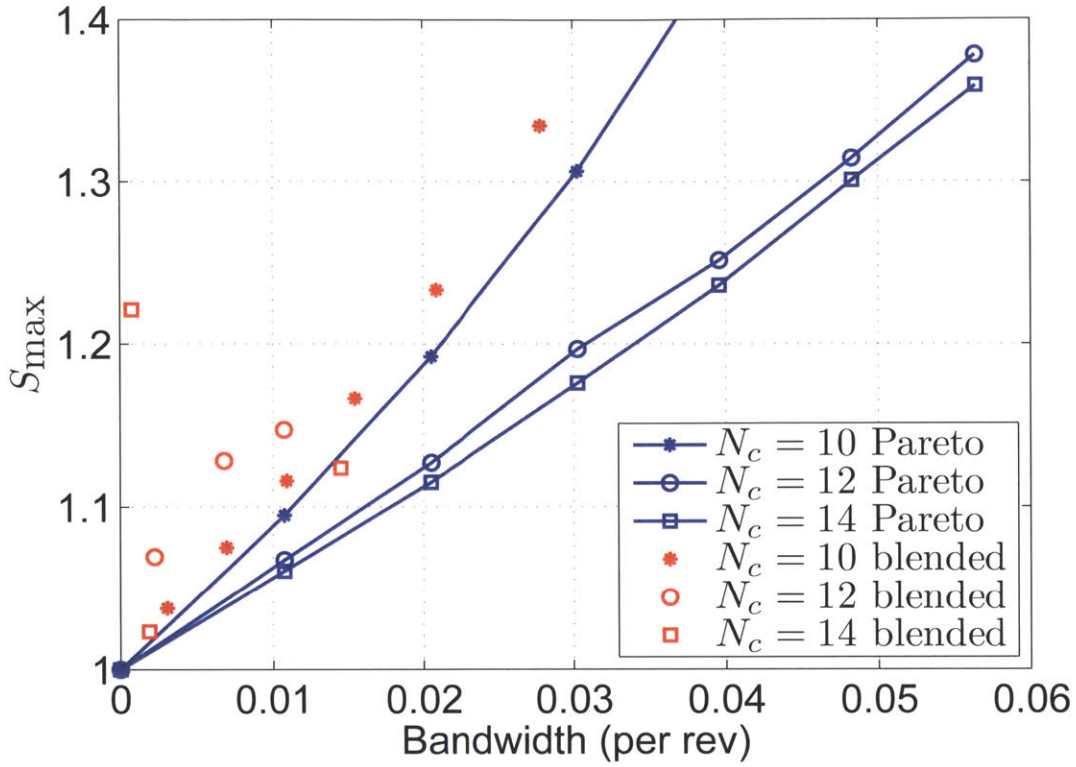

(a) $\mu = 0.20$

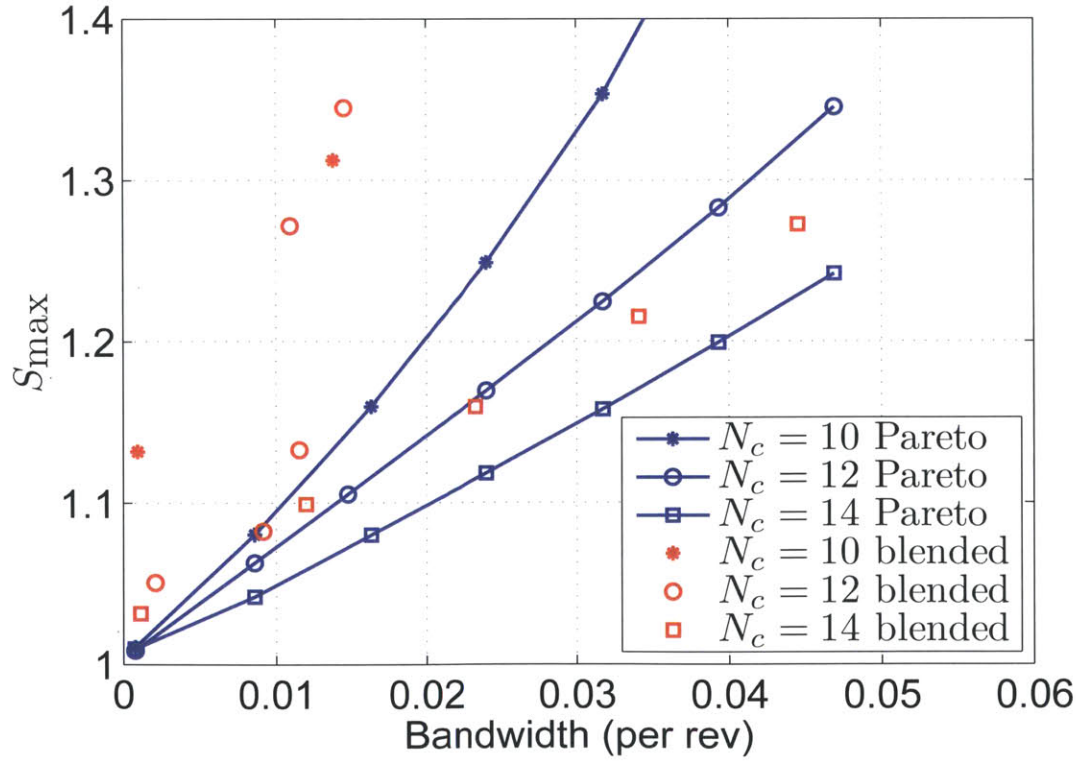

(b) $\mu = 0.30$

Figure 6-7: Performance of blended controller compared to Pareto frontiers

addition, $K_{h_j}(s)$ is strictly proper, with the general form

$$K_{h_j}(s) = \sum_{i=1}^{5} \frac{a_{ij}s + b_{ij}n_i\Omega}{s^2 + (n_i\Omega)^2}, \quad j = 1, 2, 3, 4 \tag{6.16}$$

which resembles the form of the baseline controller. The state-space realizations of $K_{h_j}(s)$ for gain-schedule control law implementation can readily be obtained from the transfer function in Equation (6.16) as

$$K_{h_j}(s) \sim \left(\begin{array}{c|c} A_h & B_{h_j} \\ \hline C_h & 0 \end{array}\right) \tag{6.17}$$

where

$$A_h = \begin{bmatrix} 0 & 1\Omega & 0 & 0 & 0 & 0 & 0 & 0 & 0 & 0 \\ -1\Omega & 0 & 0 & 0 & 0 & 0 & 0 & 0 & 0 & 0 \\ 0 & 0 & 0 & 2\Omega & 0 & 0 & 0 & 0 & 0 & 0 \\ 0 & 0 & -2\Omega & 0 & 0 & 0 & 0 & 0 & 0 & 0 \\ 0 & 0 & 0 & 0 & 0 & 3\Omega & 0 & 0 & 0 & 0 \\ 0 & 0 & 0 & 0 & -3\Omega & 0 & 0 & 0 & 0 & 0 \\ 0 & 0 & 0 & 0 & 0 & 0 & 0 & 4\Omega & 0 & 0 \\ 0 & 0 & 0 & 0 & 0 & 0 & -4\Omega & 0 & 0 & 0 \\ 0 & 0 & 0 & 0 & 0 & 0 & 0 & 0 & 0 & 5\Omega \\ 0 & 0 & 0 & 0 & 0 & 0 & 0 & 0 & -5\Omega & 0 \end{bmatrix} \tag{6.18}$$

$$B_{h_j} = \begin{bmatrix} a_{1j} & b_{1j} & a_{2j} & b_{2j} & a_{3j} & b_{3j} & a_{4j} & b_{4j} & a_{5j} & b_{5j} \end{bmatrix}^T \tag{6.19}$$

$$C_h = \begin{bmatrix} 1 & 0 & 1 & 0 & 1 & 0 & 1 & 0 & 1 & 0 \end{bmatrix} \tag{6.20}$$

Since the disturbance rejection filters $K_{h_j}(s)$, $j = 1, 2, 3, 4$, all have the same state-space matrices A_h and C_h, they can be replaced by a single gain-scheduled disturbance

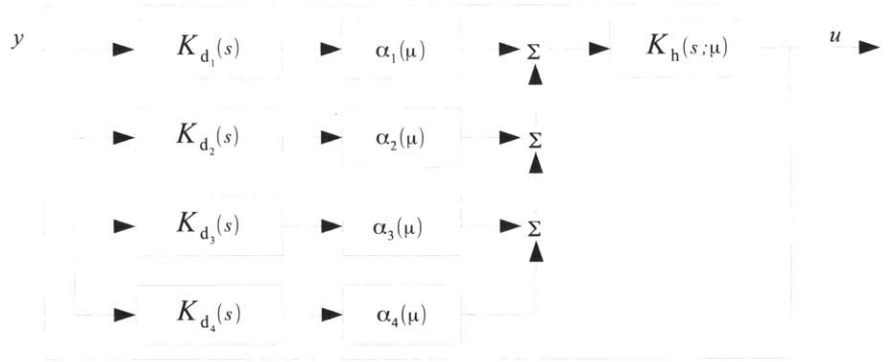

Figure 6-8: Block diagram of the gain-scheduled controller

rejection filter with the state-space realization

$$K_{\mathrm{h}}(s;\mu) \sim \left(\begin{array}{c|c} A_{\mathrm{h}} & B_{\mathrm{h}}(\mu) \\ \hline C_{\mathrm{h}} & 0 \end{array}\right) \tag{6.21}$$

The state-space matrices A_{h} and C_{h} in Equation (6.21) are given, respectively, by Equations (6.18) and (6.20), and the matrix $B_{\mathrm{h}}(\mu)$ is given by

$$B_{\mathrm{h}}(\mu) = \left[\begin{array}{cccccccc} a_1(\mu) & b_1(\mu) & a_2(\mu) & b_2(\mu) & \cdots & a_5(\mu) & b_5(\mu) \end{array}\right]^T \tag{6.22}$$

where

$$a_i(\mu) = \sum_{j=1}^{4} \alpha_j(\mu) a_{ij}, \quad i = 1,2,3,4,5 \tag{6.23}$$

$$b_i(\mu) = \sum_{j=1}^{4} \alpha_j(\mu) b_{ij}, \quad i = 1,2,3,4,5 \tag{6.24}$$

with $\alpha_j(\mu)$ given by Equations (6.11), (6.12), and (6.13). The block diagram of the implementation is shown in Figure 6-8.

6.3 Simulation Results

In order to evaluate the effectiveness of the gain-scheduled controller, we used both Simulink and CAMRAD to simulate the vibration levels under different flight profiles. In this sec-

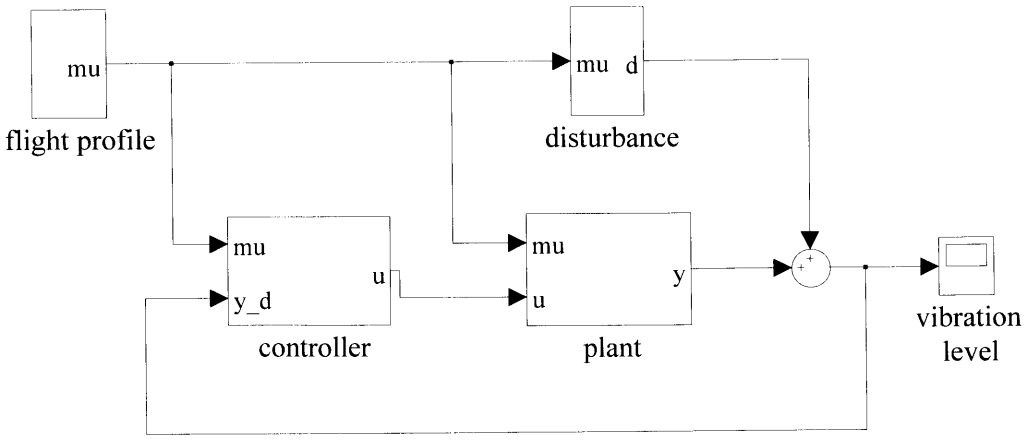

Figure 6-9: Simulink model for nonlinear simulation

tion, we describe the nonlinear simulation setups and present the results.

6.3.1 Simulink Model

The closed-loop Simulink model is composed of four main parts, the plant model, the disturbance model, the controller, and the flight profile, it is shown in Figure 6-9. The blending functions $\alpha_j(\mu),\ j = 1, 2, 3, 4$, defined by Equations (6.11) – (6.13) are used in the plant model, the disturbance model, and the controller.

The plant is obtained by blending the output of the LTI models identified from the CAMRAD simulation data as

$$G(s;\mu) = \sum_{j=1}^{4} \alpha_j(\mu) G_j(s) \tag{6.25}$$

where $G_j(s)$ is a plant model that corresponds to $\mu = \mu_j$. For the simulation results discussed in the next section, we used $G_j(s),\ j = 1, 2, 3, 4$, identified from the CAMRAD simulations performed with parameters shown in Table 6.2.

The disturbance is modeled by blending the harmonic disturbances obtained from the CAMRAD simulation data. Because the CAMRAD rotor model is symmetric, the data from CAMRAD simulation only contain harmonic disturbances with frequencies that are multiples of $N\Omega$, where $N = 5$ is the number of rotor blades, and Ω is the rotor frequency. For the Simulink model, we only included the harmonic disturbance with frequency 5Ω.

Table 6.2: CAMRAD simulation parameters of the identified models used in Simulink

j	μ_j	α(deg)	C_T/σ
1	0.15	-3.7	0.075
2	0.20	-5.5	0.075
3	0.30	-9.1	0.075
4	0.375	-12.0	0.075

The harmonic disturbance is modeled as

$$d(t;\mu) = \sum_{j=1}^{4} \alpha_j(\mu) d_j(t) \tag{6.26}$$

where

$$d_j(t) = \left(a_j \cos(5\Omega t) + b_j \sin(5\Omega t)\right), \; j = 1,2,3,4 \tag{6.27}$$

are the harmonic components, with a frequency of 5Ω, of the hub normal force from CAMRAD simulation performed with parameters shown in Table 6.2. The coefficients a_j and b_j are, respectively, the magnitude of the cosine and sine components of the disturbance at the fifth harmonic. With the CAMRAD simulation data regularized as discussed in Chapter 5, a_j is the real part of the FFT of the output data at the harmonic frequency 5Ω, and b_j is the negative of the imaginary part of the FFT of the output data at the harmonic frequency 5Ω.

For the closed-loop Simulink model, the controller is given by

$$K(s;\mu) = \sum_{j=1}^{4} \alpha_j(\mu) K_j(s) \tag{6.28}$$

where $K_j(s), \; j = 1,2,3,4$, are the fixed-order $\mathcal{H}_\infty$ controller designed for the different values of μ as discussed in Section 6.2.1. We used fixed-order $\mathcal{H}_\infty$ controllers of orders 10, 12, and 14 in the gain-scheduled controllers. Each individual fixed-order $\mathcal{H}_\infty$ controller was designed to have $S_{\max} \approx 1.2$, so in effect, the higher order fixed-order $\mathcal{H}_\infty$ controllers have larger bandwidths. Note that the blending of the output signals allows different orders of controllers to be used in the gain-scheduled controller, so it is possible to fix both the bandwidths and peak sensitivities for all the fixed-order $\mathcal{H}_\infty$ controllers. The baseline levels of vibrations were obtained from the same Simulink model, except the controller

was disconnected from the plant.

6.3.2 Simulink Simulation Results

The simulations were performed with two different flight profiles. The flight profiles we considered only varied μ linearly as a function of time. The flight profiles are shown in Figure 6-10a and Figure 6-11a, both start at $\mu = 0.10$, and increase linearly to $\mu = 0.40$. The duration of Flight Profile 1 is 30 seconds, the duration of Flight Profile 2 is 60 seconds, and they were initiated after the initial transient responses have died out. Note that the blending functions $\alpha_j(\mu)$ used in the Simulink simulation effectively limited the range of the model to be between $\mu = 0.15$ and $\mu = 0.375$.

The open-loop vibration levels for Flight Profiles 1 and 2 are shown in Figures 6-10b and 6-11b, respectively. The root-mean-square (RMS) values of the open-loop vibrations at the fifth harmonic frequency within the duration of the flight profiles are tabulated in Table 6.3, and serve as the baseline for comparing the effectiveness of the gain-scheduled controller. The closed-loop responses of system with the gain-scheduled controller composed of 10th order fixed-order $\mathcal{H}_\infty$ controllers for Flight Profile 1 and Flight Profile 2 are shown in Figure 6-10c and Figure 6-11c, respectively. The RMS vibration level was reduced by 94.6% for Flight Profile 1, and 97.2% for Flight Profile 2. Slightly larger reductions in the fifth harmonic vibration levels were achieved with higher order controllers, since these controllers have larger bandwidths, and thus respond more quickly to changes in the disturbance. For the gain-scheduled controllers composed of 12th and 14th order fixed-order $\mathcal{H}_\infty$ controllers, the amount of vibration reductions, tabulated in Table 6.3, exceeded 96% for both flight profiles. The closed-loop responses of the gain-scheduled controllers composed of 12th and 14th order fixed-order $\mathcal{H}_\infty$ controllers are shown in Figures 6-12 and 6-13. The control signals for all cases examined are plotted in Figures 6-10d, 6-11d, 6-12d, and 6-13d, the magnitudes of the commanded flap deflections were all less than 1 degree, so no saturation occurred in the simulations. However, the Simulink simulation only contained disturbances at the fifth harmonic frequency, while wind tunnel tests showed the helicopter experiences disturbances at almost all harmonic frequencies, thus actuator saturation may

Table 6.3: RMS vibration levels at the fifth harmonic frequency with gain-scheduling of controllers of various orders from Simulink simulations

	Flight Profile 1		Flight Profile 2	
	RMS (lb)	Reduction (%)	RMS (lb)	Reduction (%)
Baseline (no control)	57.24	-	57.24	-
10th order	3.08	94.6	1.60	97.2
12th order	2.15	96.2	1.09	98.1
14th order	1.20	97.9	0.61	98.9

occur in real applications. To mitigate the effects of saturation, the fixed-order $\mathcal{H}_\infty$ controllers should be implemented as discussed in Section 6.2.4, which allows the use of the anti-windup scheme developed by Shin, Cesnik and Hall [88].

6.3.3 CAMRAD Closed-Loop Simulation

The closed-loop CAMRAD simulations were conducted by the Boeing Company. The helicopter rotor model used for the closed-loop simulation was the same model used for plant identification in the previous chapter. The hub normal force was used as the feedback signal. Since the controllers were designed for the linearized plant with the deviation of the hub normal force from the nominal value as the feedback signal, direct implementation of the controller described above resulted in a static offset of the trailing-edge flaps. A direct feed-through term was used for each controller to ensure the controller's DC gain was zero to negate the static offset. The fixed-order $\mathcal{H}_\infty$ controller designed for the advance ratio $\mu = \mu_j$ with the direct feed-through term has the state-space realization

$$\widehat{K}_j(s) \sim \left(\begin{array}{c|c} A_{k_j} & B_{k_j} \\ \hline C_{k_j} & D_{k_j} \end{array}\right), \quad j = 1, 2, 3, 4 \tag{6.29}$$

where A_{k_j}, B_{k_j}, C_{k_j} are the state-space matrices of the fixed-order $\mathcal{H}_\infty$ controller $K_j(s)$, and the direct feed-through term D_{k_j} is obtained as

$$D_{k_j} = -K_j(0) \tag{6.30}$$

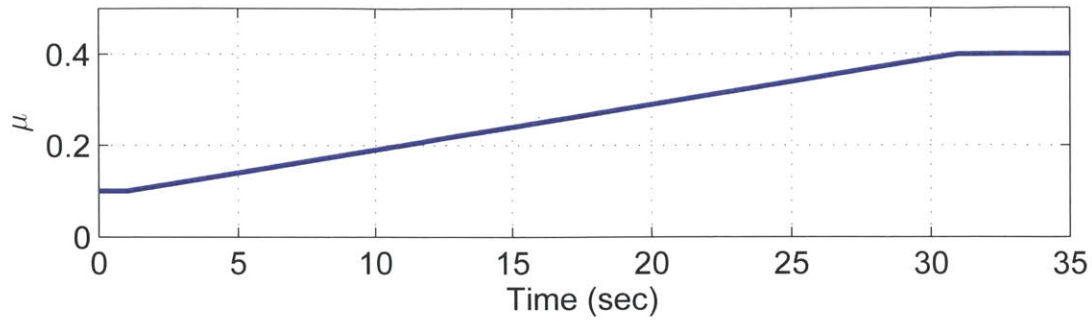

(a) Profile of advance ratio μ

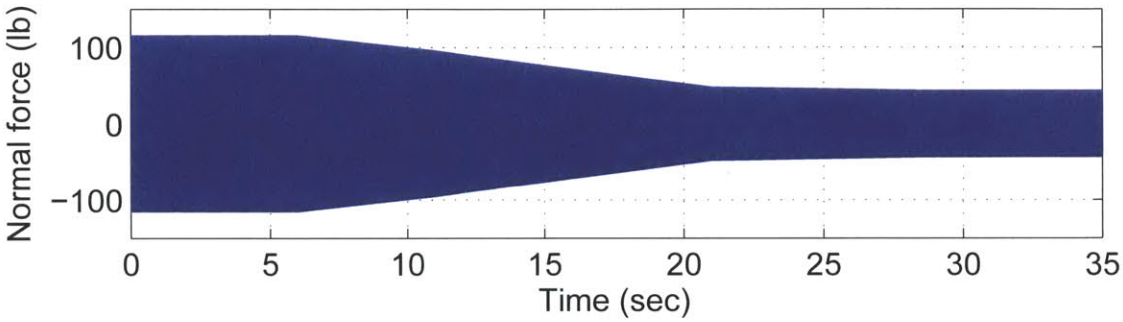

(b) Open-loop vibration

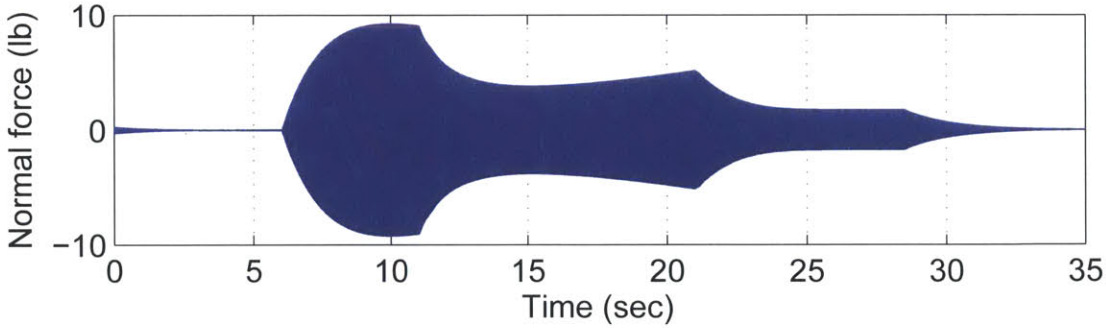

(c) Closed-loop vibration

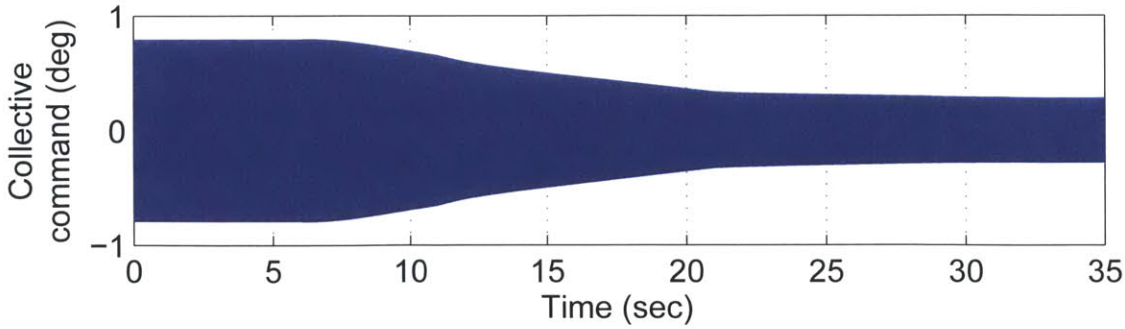

(d) Collective flap command

Figure 6-10: Simulation results from Simulink for Flight Profile 1, gain-scheduled control law using 10th order controllers

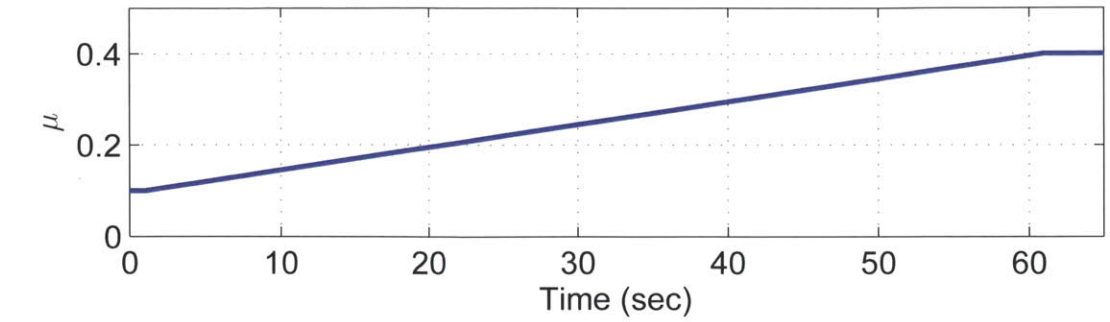

(a) Profile of advance ratio μ

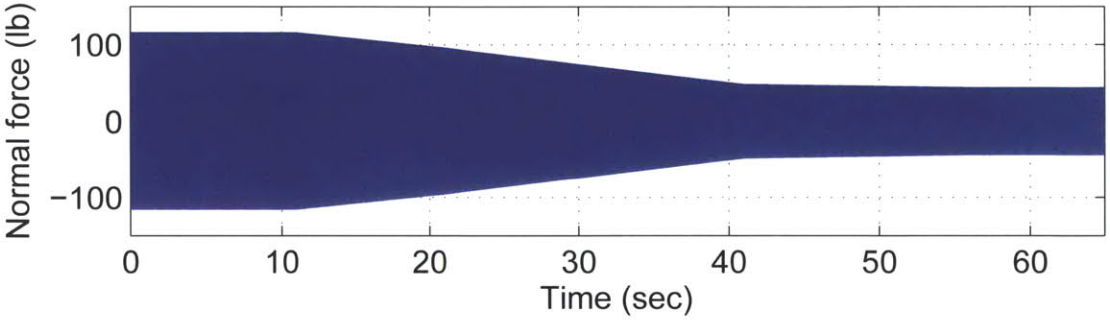

(b) Open-loop vibration

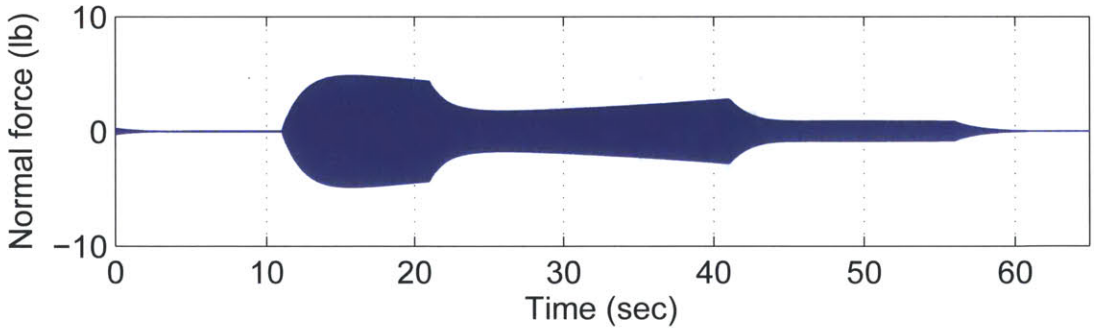

(c) Closed-loop vibration

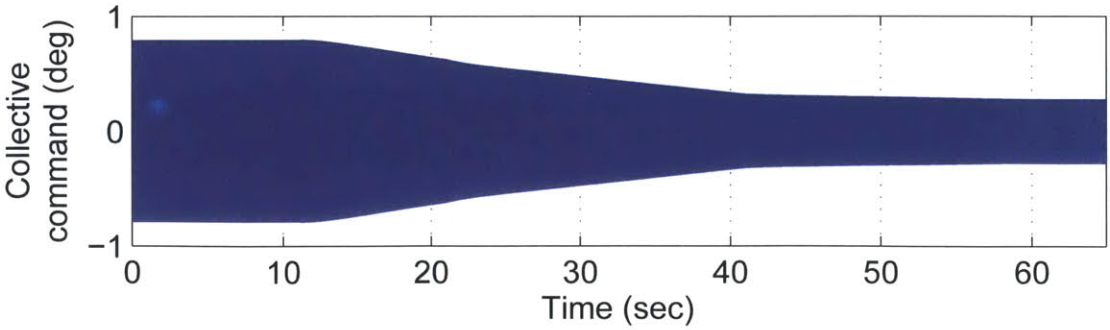

(d) Collective flap command

Figure 6-11: Simulation results from Simulink for Flight Profile 2, gain-scheduled control law using 10th order controllers

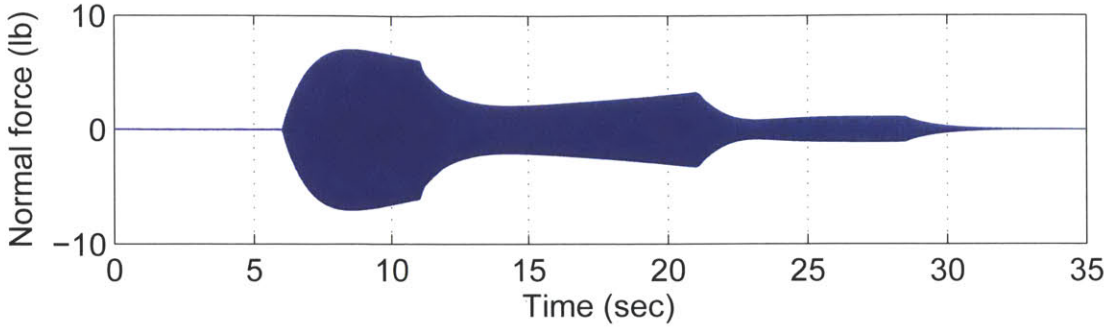

(a) Closed-loop vibration for Flight Profile 1

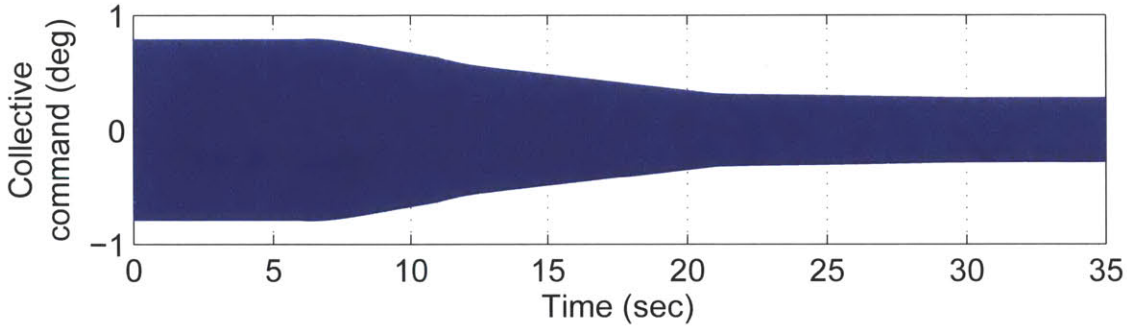

(b) Collective flap command for Flight Profile 1

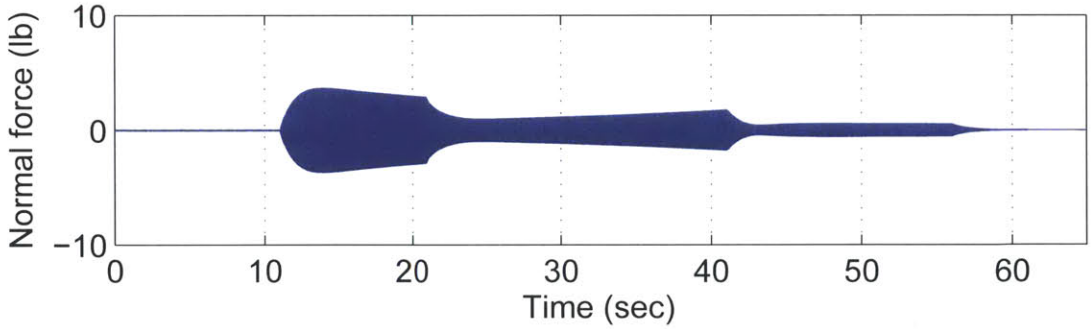

(c) Closed-loop vibration for Flight Profile 2

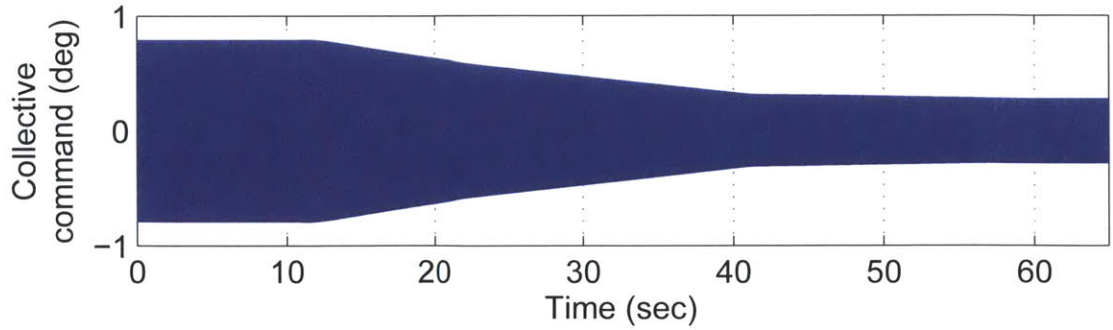

(d) Collective flap command for Flight Profile 2

Figure 6-12: Simulation results with gain-scheduled control law using 12th order controllers

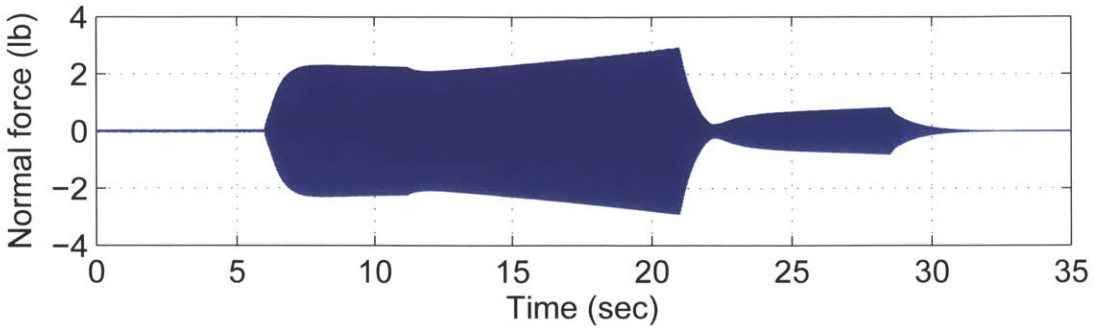

(a) Closed-loop vibration for Flight Profile 1

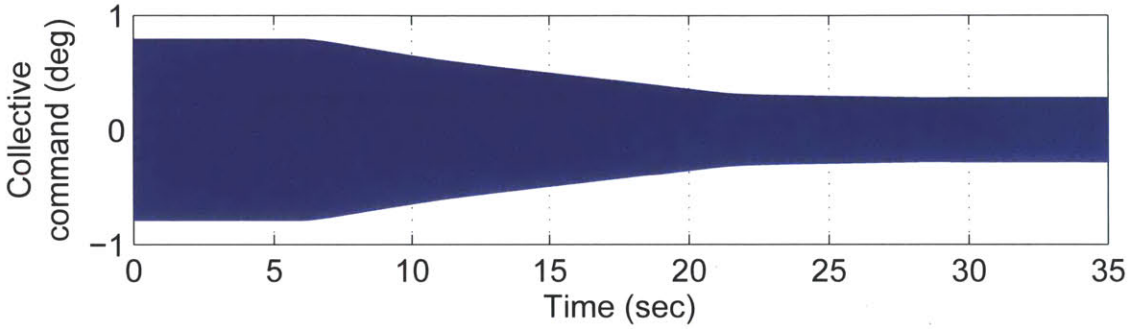

(b) Collective flap command for Flight Profile 1

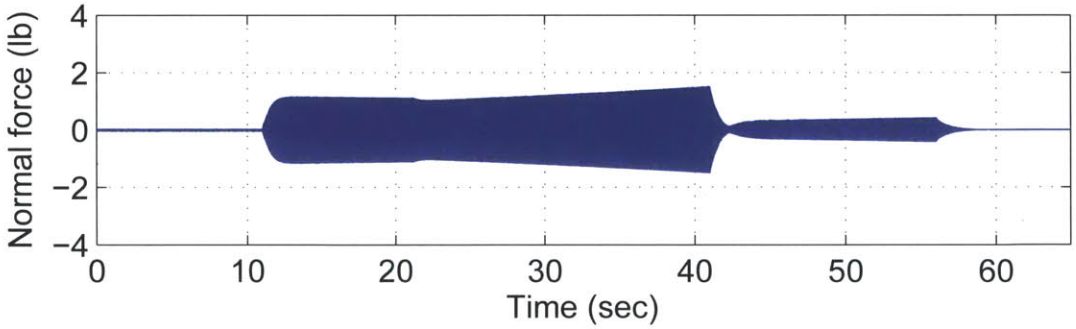

(c) Closed-loop vibration for Flight Profile 2

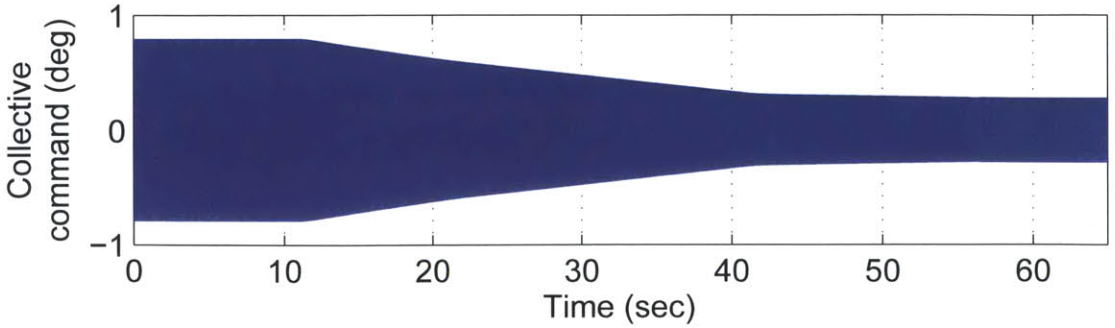

(d) Collective flap command for Flight Profile 2

Figure 6-13: Simulation results with gain-scheduled control law using 14th order controllers

Table 6.4: μ schedules for the CAMRAD simulations

Flight Schedule	Starting μ	Final μ	Duration (sec)
1	0.15	0.2	4
2	0.15	0.3	12
3	0.15	0.375	18

The D_{k_j} terms are interpolated in the gain-scheduled controller using the blending functions given by Equations (6.11), (6.12), and (6.13). Alternative ways to eliminate the flap static offset are to incorporate a high-pass filter in the control loop, or feedback the deviation of the hub normal force from the nominal hub normal force.

To verify the implementation of the controller in CAMRAD, the fixed-order controller $\widehat{K}_j(s)$ was first implemented using Fortran subroutines in the CAMRAD simulation with fixed $\mu = \mu_j$. The input and output of the controller $\widehat{K}_j(s)$, which are the hub normal force and the flap displacement, respectively, were used in a linear regression to validate that the coefficients of $\widehat{K}_j(s)$ were correctly implemented. It was determined that the integration routine used by CAMRAD caused frequency warping that affected the performance of the controller. The harmonic poles of $\widehat{K}_j(s)$ were prewarped to cancel the effect of the integration routine. Once the Fortran subroutines were verified to implement the fixed-order controller correctly, they were extended to incorporate the blending functions for gain-scheduling.

Simulations of the helicopter rotor controlled by the gain-scheduled controller were conducted for three different Flight Schedules shown in Table 6.4. The gain-scheduling was accomplished by using the 10th order fixed-order $\mathcal{H}_\infty$ controllers. The advance ratio μ was varied linearly in the CAMRAD simulations starting after four seconds, which allowed the large initial transient hub normal force caused by the direct feed-through term D_{k_j} to dissipate. The CAMRAD simulations also continued for three seconds after the final value of μ was reached. The baseline levels were obtained by running the simulations with the controller disconnected from the helicopter rotor model. For Flight Schedule 1, the open-loop hub normal force is shown in Figure 6-14a. Because the inflow in the CAMRAD simulations was not set up to vary with the advance ratio μ, the average hub normal force varied as μ increased. The hub normal force for the entire closed-loop simulation of Flight

Table 6.5: RMS vibration levels of the band-pass filtered hub normal force from CAMRAD simulations

Flight Schedule	Baseline (lb)	Closed-loop (lb)	Reduction (%)
1	104.96	3.04	97.1
2	113.57	2.26	98.0
3	110.59	2.37	97.9

Schedule 1 is shown in Figure 6-14b. Figure 6-14c shows the details of the hub normal force between $t = 3.8$ sec and $t = 4.2$ sec, note that the dominant vibration is at 10 per rev, which is equivalent to 65.3 Hz. A band-pass filter was used to examine the effectiveness of the gain-scheduled controller at 5 per rev. The band-pass filter consisted of a high-pass Butterworth filter in series with a low-pass Butterworth filter. The high-pass filter had a cutoff frequency of 4.5 per rev, and the low-pass filter had a cutoff frequency of 5.5 per rev. The filtered open-loop hub normal force for Flight Schedule 1 starting at $t = 3$ sec is shown in Figure 6-15a. The closed-loop case is shown in Figure 6-15b with Figure 6-15c showing the details between $t = 3.8$ sec and $t = 4.2$ sec.

For Flight Schedule 2 and Flight Schedule 3, the CAMRAD simulation results are shown in Figure 6-16 and Figure 6-17, respectively. The performance of the gain-scheduled controller is tabulated in Table 6.5, which shows over 97% reduction in the RMS value of the band-pass filtered hub normal force during the time span in which the advance ratio μ was increasing.

A second set of CAMRAD simulations were conducted with the swashplate collective adjusted at the end of the simulations to provide the same level of nominal hub normal force. The open-loop and closed-loop simulation results for Flight Schedule 1 are shown in Figure 6-18. The average hub normal force still varied as μ was increased, but the adjustment of the swashplate collective ensured the final average hub normal force matched the nominal value. The band-pass filtered results for the reduction of the 5 per rev vibration are shown for the three different Flight Schedules in Figures 6-19, 6-20, and 6-21. The RMS values are tabulated in Table 6.6, with similar levels of reduction as in the case without the collective adjustment.

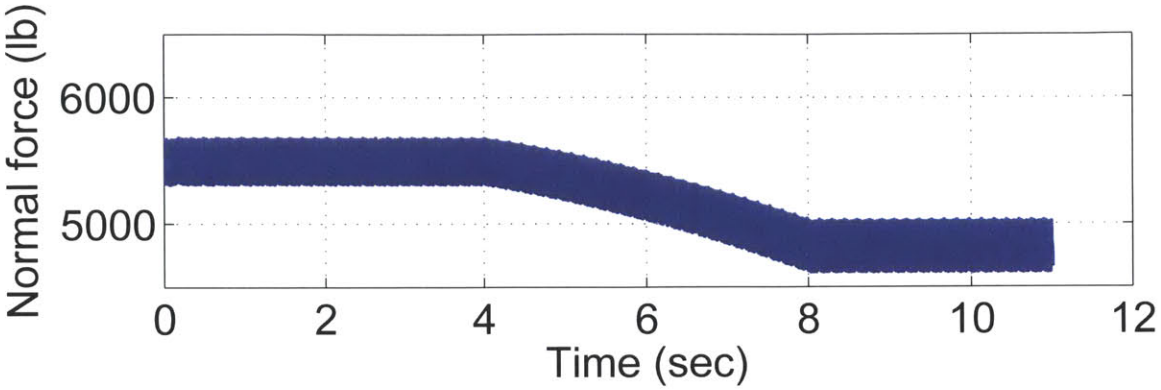

(a) Open-loop simulation result

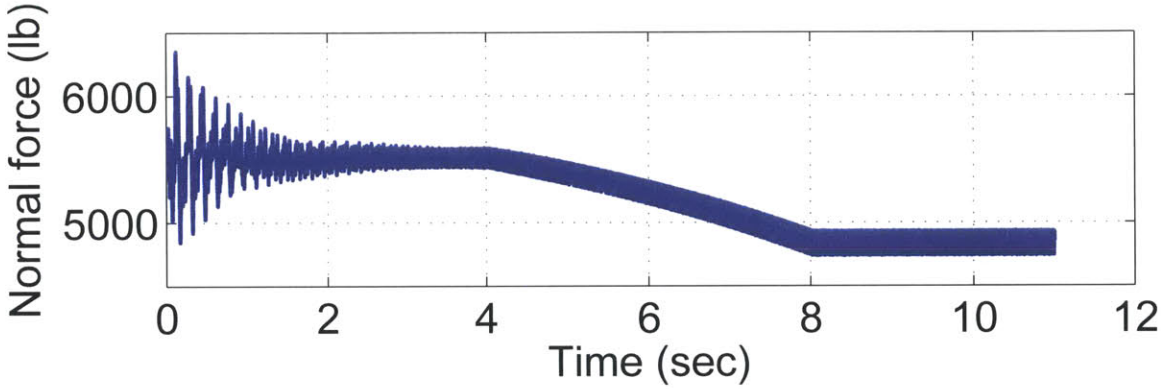

(b) Entire closed-loop simulation result

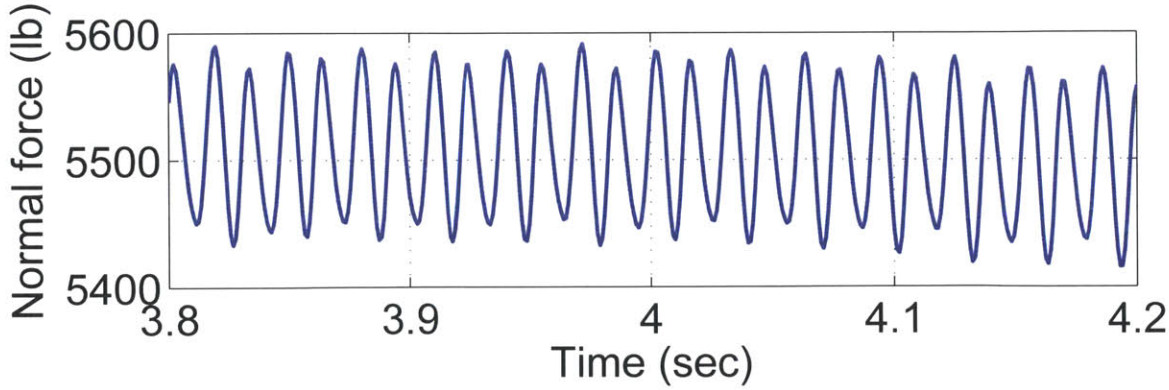

(c) Closed-loop simulation result between $t = 3.8$ sec and $t = 4.2$ sec

Figure 6-14: Open-loop and closed-loop CAMRAD simulation result for Flight Schedule 1

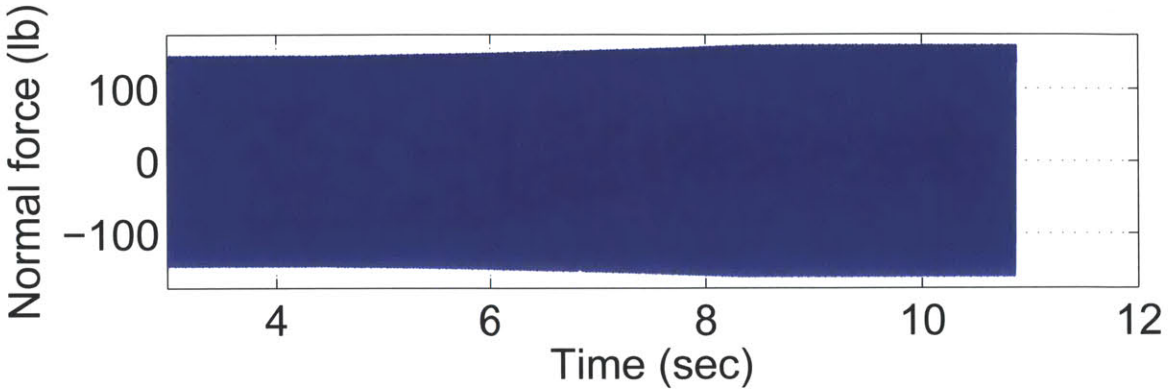

(a) Filtered open-loop simulation result

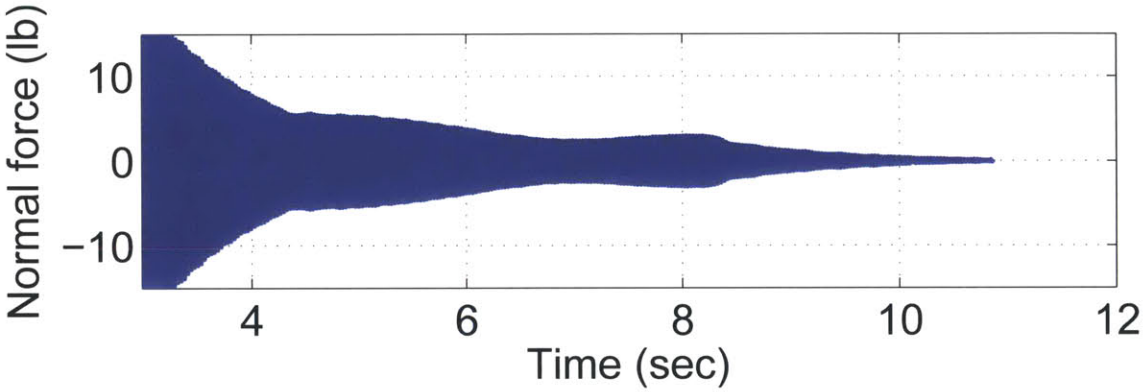

(b) Filtered closed-loop simulation result

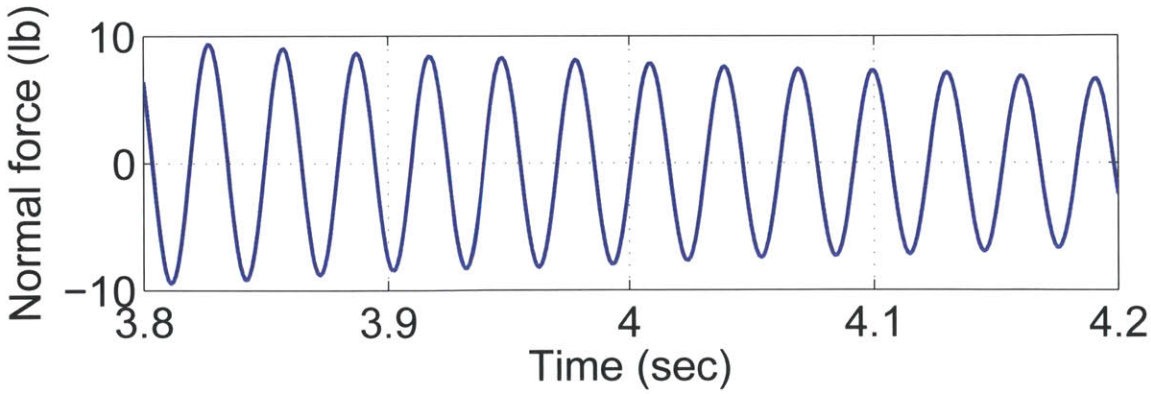

(c) Filtered closed-loop simulation result between $t = 3.8$ sec and $t = 4.2$ sec

Figure 6-15: Band-pass filtered open-loop and closed-loop CAMRAD simulation result for Flight Schedule 1

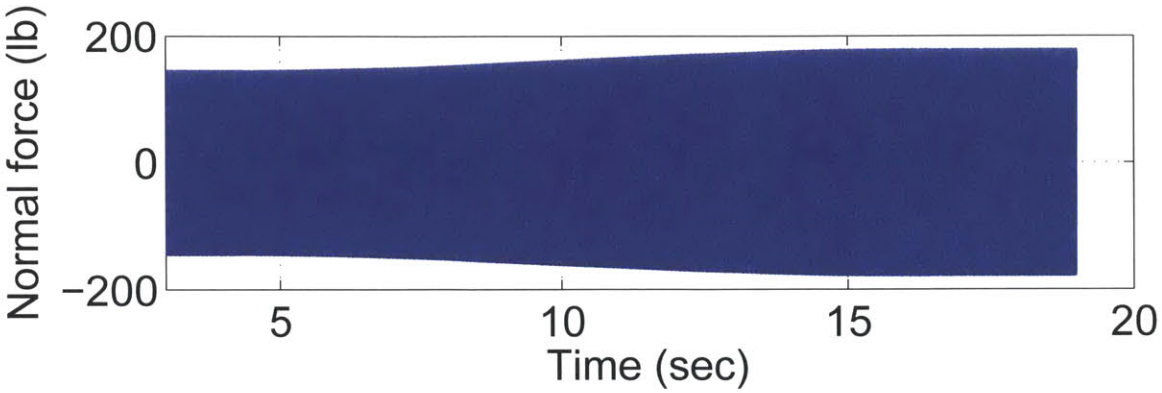

(a) Filtered open-loop simulation result

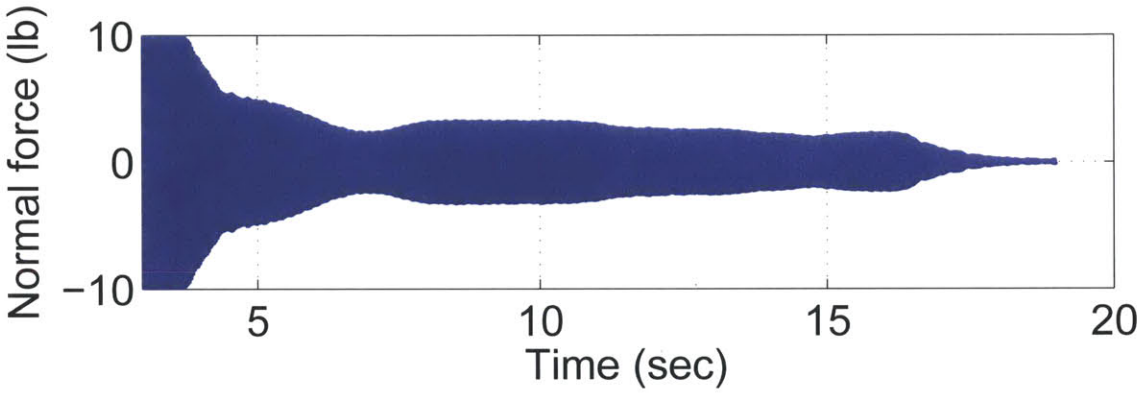

(b) Filtered closed-loop simulation result

Figure 6-16: Band-pass filtered open-loop and closed-loop CAMRAD simulation result for Flight Schedule 2

Table 6.6: RMS vibration levels of the band-pass filtered hub normal force from CAMRAD simulations with collective adjustment

Flight Schedule	Baseline (lb)	Closed-loop (lb)	Reduction (%)
1	103.84	2.99	97.1
2	110.01	2.53	97.7
3	104.88	2.52	97.6

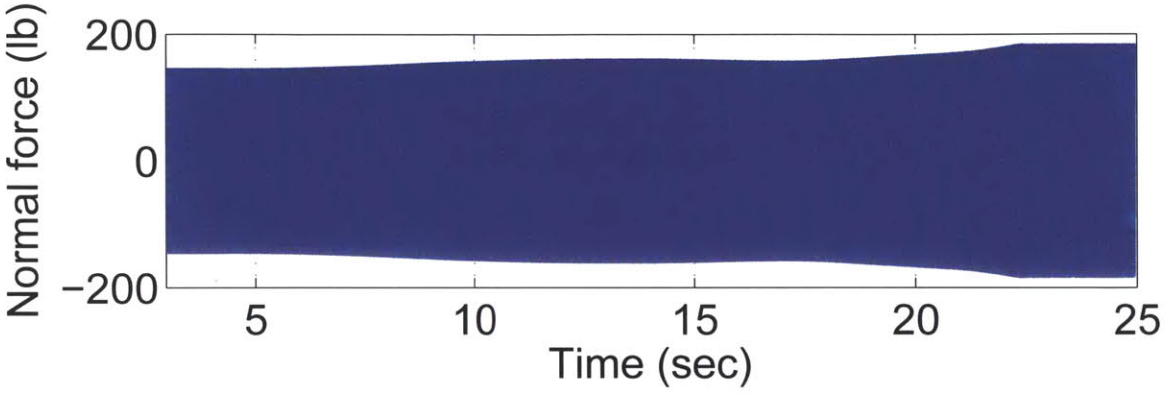

(a) Filtered open-loop simulation result

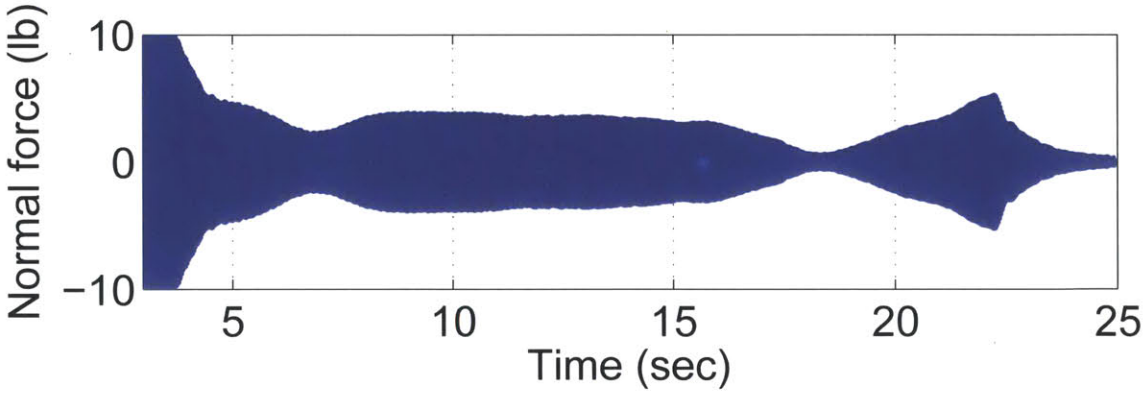

(b) Filtered closed-loop simulation result

Figure 6-17: Band-pass filtered open-loop and closed-loop CAMRAD simulation result for Flight Schedule 3

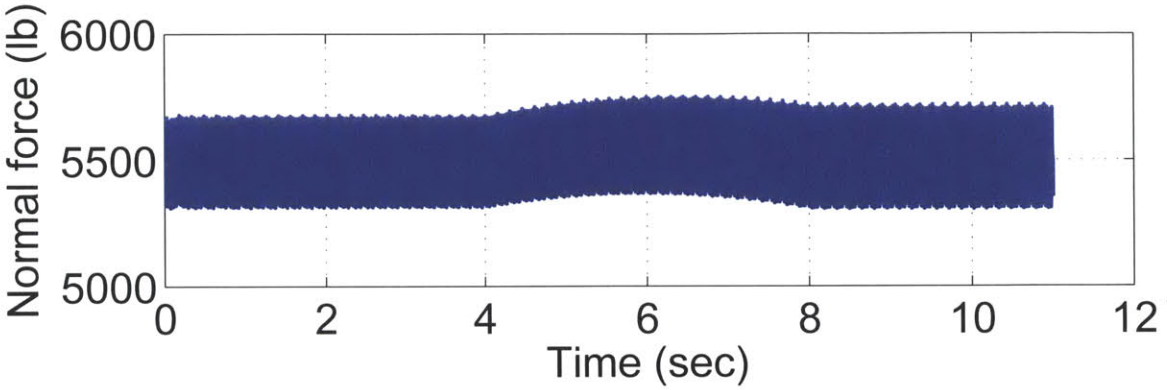

(a) Open-loop simulation result

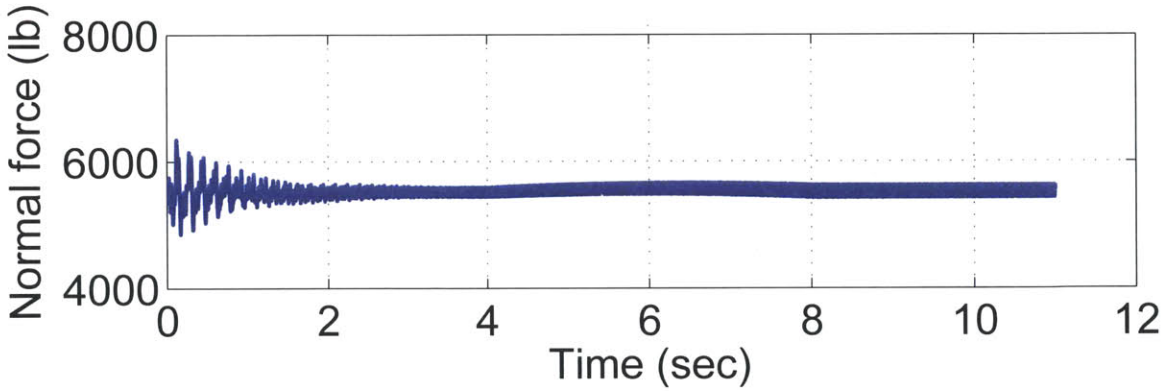

(b) Closed-loop simulation result

Figure 6-18: Open-loop and closed-loop CAMRAD simulation result for Flight Schedule 1. Simulations conducted with swashplate collective adjustment

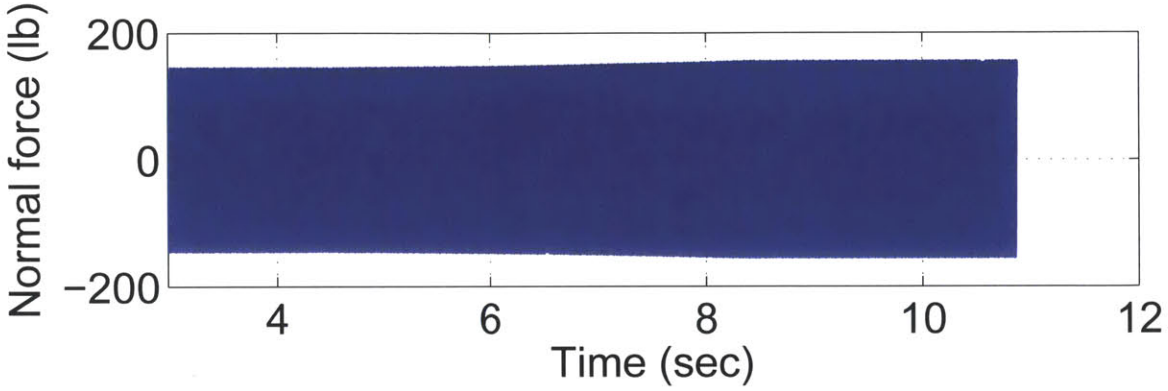

(a) Filtered open-loop simulation result

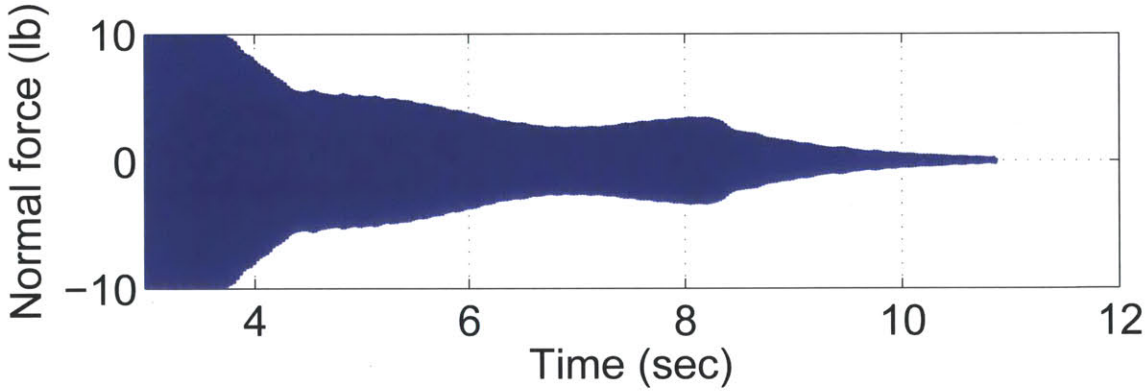

(b) Filtered closed-loop simulation result

Figure 6-19: Band-pass filtered open-loop and closed-loop CAMRAD simulation result for Flight Schedule 1. Simulations conducted with swashplate collective adjustment

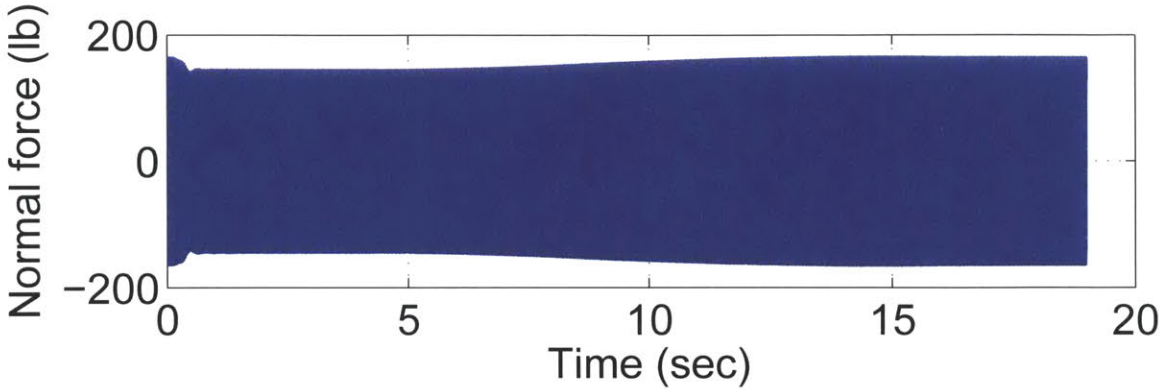

(a) Filtered open-loop simulation result

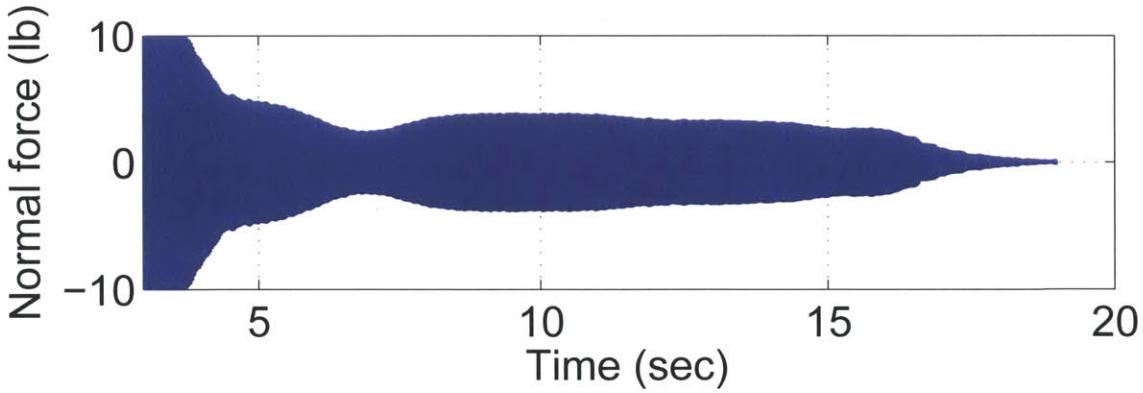

(b) Filtered closed-loop simulation result

Figure 6-20: Band-pass filtered open-loop and closed-loop CAMRAD simulation result for Flight Schedule 2. Simulations conducted with swashplate collective adjustment

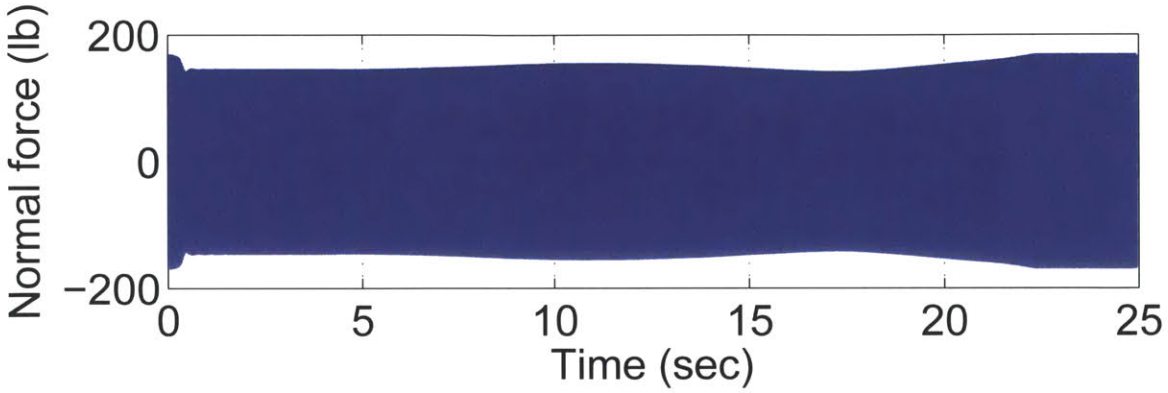

(a) Filtered open-loop simulation result

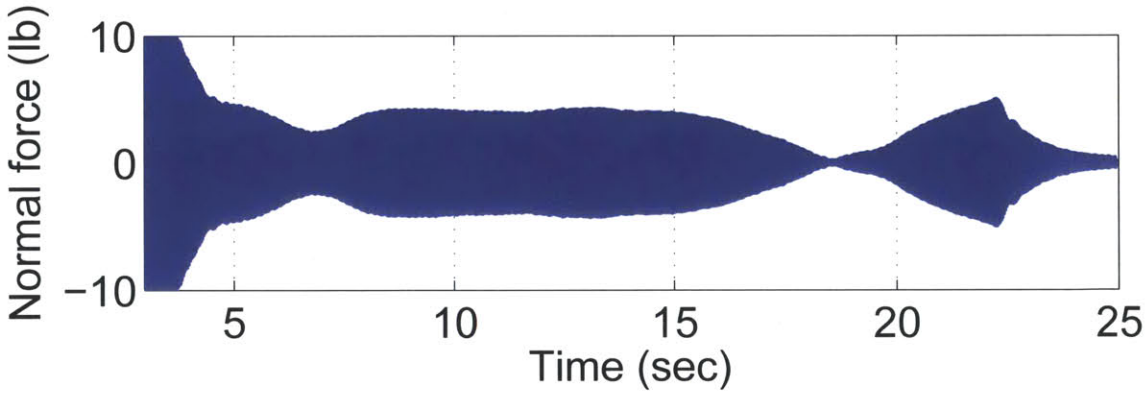

(b) Filtered closed-loop simulation result

Figure 6-21: Band-pass filtered open-loop and closed-loop CAMRAD simulation result for Flight Schedule 3. Simulations conducted with swashplate collective adjustment

6.4 Summary

In this chapter, we first applied the fixed-order $\mathcal{H}_\infty$ control synthesis method developed in Chapter 4 to design a single controller for multiple LTI plant models. Due to the large variations in the plant dynamics, the single fixed-order $\mathcal{H}_\infty$ controller is not a viable option for both flight conditions used in wind tunnel testing. However, for multiple plants with similar dynamics, such as the case in CAMRAD simulations with a constant advance ratio μ, but different rotor shaft angle α, and blade loading coefficient C_T/σ, the single fixed-order controller achieves some performance improvement over the controller designed for just one particular plant model. For full flight envelope harmonic disturbance rejection, we proposed using a gain-scheduled controller that is based on the fixed-order $\mathcal{H}_\infty$ controllers designed for different values of the scheduling variable μ. We developed a structure for the gain-scheduled controller that allows the implementation of a previously developed anti-windup algorithm. The performance of the gain-scheduled control law was analyzed using nonlinear simulations. In the relatively simple Simulink simulations with flight profiles that consisted of linearly increasing μ, reductions of greater than 94% were achieved. The more sophisticated CAMRAD simulations with linearly varying μ showed over 97% reduction in the 5 per rev vibration.

Chapter 7

Conclusions and Future Work

The subject of this thesis is the analysis and design of controllers for vibration reduction in helicopters. The controllers are based on Shaw's higher harmonic control (HHC) algorithm, and are designed to attenuate the main source of vibration in helicopters, namely the harmonic disturbance originating from the main rotor. As a first step towards designing effective controllers, we examined the dynamics of the helicopter rotor relevant to control design, and the characteristics of the harmonic disturbance. Our analysis of both wind tunnel test data and aeromechanical simulation results showed that the effect of periodicity on the rotor dynamics is small at various constant flight conditions within the flight envelope. The lack of significant effects from periodicity allows us to model the rotor at a constant flight condition by a linear time-invariant (LTI) system. However, the dynamics of the helicopter rotor is dependent on the advance ratio. Hence, models of the helicopter rotor at different advance ratios must be represented by different LTI models.

In order to quantify the performance of a harmonic disturbance rejection controller, we defined the bandwidth and peak sensitivity of the closed-loop system in the context of harmonic disturbance rejection. The bandwidth and peak sensitivity are incorporated into the specifications of a notch filter, which allows us to analyze the performance of harmonic disturbance rejection controllers using a method from $\mathcal{H}_\infty$ control theory. Two new optimization based control design methodologies for harmonic disturbance rejection were presented, using notch filter as weighting functions. The full-order $\mathcal{H}_\infty$ methodology produces controllers that achieve the maximum performance possible for the given plant dynamics, if

bandwidth and peak sensitivity are used as measures of performance. The fixed-order $\mathcal{H}_\infty$ methodology yields controllers that have performance still significantly better than baseline HHC controllers, but with lower controller order than the full-order $\mathcal{H}_\infty$ controllers, which may have very high order. In addition, the fixed-order $\mathcal{H}_\infty$ controllers are guaranteed to be marginally stable, which is not the case for the full-order $\mathcal{H}_\infty$ controllers. A method to obtain a gain-scheduled control law to reduce vibration throughout the flight envelope was also presented. In simulations, the gain-scheduled control law showed significant reduction in the RMS vibration level.

7.1 Summary of Contributions

Contributions in three areas of helicopter vibration control were made in this thesis. The three areas are the dynamics of the helicopter rotor for control design, the achievable performance in harmonic disturbance rejection, and the control design methods for helicopter vibration reduction.

In the area of the helicopter rotor dynamics relevant to control design, we have the following conclusions:

1. Experimental data in the literature and in this research suggest that the helicopter dynamics associated with higher harmonic control can be well modeled as linear and time-invariant (LTI), allowing LTI control theory concepts to be applied to the higher harmonic control problem.

2. Analysis of the simulation data shows that the helicopter rotor dynamics is strongly dependent on the advance ratio μ, and only weakly dependent on the rotor shaft angle α and blade loading coefficient C_T/σ. The implication is that high performance full flight envelope control law must account for the changes in μ during flight.

3. In constant forward flight conditions, wind tunnel data showed that significant disturbances exist at nearly all harmonics of the main rotor frequency. To effectively reduce vibration in a helicopter, the controller should be designed to attenuate multiple harmonics.

In the analysis of harmonic disturbance rejection performance, the contributions are:

1. We defined two useful measures of higher harmonic control performance, the bandwidth and peak sensitivity of the HHC control system. The bandwidth is a measure of the speed of response of the control system to changes in vibration level; the peak sensitivity is a measure of the robustness of the closed-loop system stability to changes in the plant. The bandwidth and peak sensitivity can be expressed in a single function of frequency in the form of a notch filter.

2. Using analysis techniques from the $\mathcal{H}_\infty$ control theory, the notch filter can be used to verify whether a given controller meets a specified bandwidth and peak sensitivity requirement. Synthesis techniques from the $\mathcal{H}_\infty$ control theory can be used to design full-order controllers that meet a specified performance level, if such a controller exists. Furthermore, for a given plant, the limits of performance in harmonic disturbance rejection can be established with the $\mathcal{H}_\infty$ methodology.

In the design of harmonic disturbance rejection controller, we have developed two controller design methodologies leading to the following conclusions :

1. The full-order $\mathcal{H}_\infty$ methodology can be used to produce controllers that achieve the maximum performance possible for the given plant dynamics, if bandwidth and peak sensitivity are used as measures of performance. Hence the harmonic disturbance performance limits can be established with the full-order $\mathcal{H}_\infty$ methodology.

2. Because of the high order of the weighting filters, the full-order $\mathcal{H}_\infty$ controller is generally of high order. Another disadvantage of the $\mathcal{H}_\infty$ controller is that it is not guaranteed to be stable, which is problematic in the event of actuator saturation.

3. The fixed-order $\mathcal{H}_\infty$ methodology optimizes the same performance measures as the full-order $\mathcal{H}_\infty$ methodology. The imposed structure in the optimization setup results in marginally stable controllers with lower orders. The fixed-order $\mathcal{H}_\infty$ controllers contain poles on the $j\omega$-axis as required for complete harmonic disturbance rejection, and all other poles are in the open left half-plane.

4. Both the full-order and fixed-order $\mathcal{H}_\infty$ controllers can be implemented using a demodulation/modulation scheme developed for the baseline HHC controllers, which allows a previously developed anti-windup algorithm to be used.

5. For a representative rotor system (the SMART rotor), the full-order $\mathcal{H}_\infty$ controllers designed to reject the first five harmonics have significantly higher bandwidth (3–4 times) for a given peak sensitivity than the baseline HHC controllers.

6. For a representative rotor system (the SMART rotor), the fixed-order $\mathcal{H}_\infty$ controllers designed to reject the first five harmonics have significantly higher bandwidth (1.5–2.5 times) for a given peak sensitivity than the baseline HHC controllers, sometimes with only a small increase in controller order over that of baseline HHC controllers.

7. The fixed-order $\mathcal{H}_\infty$ methodology can be used to design a controller for the helicopter rotor at different flight conditions. The performance of a single fixed-order $\mathcal{H}_\infty$ controller designed for plant models representing the helicopter rotor at very different values of μ is poor, but the single controller approach appears to be effective when the plant models are at the same value of μ, but different values of the shaft angle α and blade loading coefficient C_T/σ.

8. The fixed-order $\mathcal{H}_\infty$ controllers are used in a gain-scheduled control law for full flight envelope disturbance rejection. The control law is scheduled on μ, with the control signal from the fixed-order $\mathcal{H}_\infty$ controllers blended to achieve bumpless transfer. CAMRAD simulations of accelerating forward flights show that the gain-scheduled controller reduces the 5 per rev normal vibration by over 97%.

7.2 Future Work

Helicopter vibration reduction remains an important area of research. Reducing the vibration levels would increase the utility of the helicopter and reduce the operating cost. Several areas related to the work presented in this thesis warrant further research:

1. The control methodologies introduced in this thesis need experimental verification. In particular, the simplicity and stability of the fixed-order $\mathcal{H}_\infty$ controller make it a good candidate to be further examined in wind tunnel testing. The fixed-order $\mathcal{H}_\infty$ controller synthesis procedure sets up the controller as two parallel filters, one responsible for the harmonic disturbance rejection, the other used to improve the controller performance. It is possible to implement the fixed-order $\mathcal{H}_\infty$ controller as two filters in series, which would allow the anti-windup algorithm developed by Shin, Cesnik and Hall [88] to be deployed. The anti-windup scheme minimizes the degradation in performance when the actuators are saturated. Furthermore, the harmonic disturbance rejection filter can be implemented using the demodulation/modulation scheme developed by Hall and Wereley [44]. By using the actual rotor speed in the demodulation/modulation scheme, the controller can account for variations in the rotor angular speed.

2. In this thesis, the harmonic disturbance controllers were designed to reduce the vibration in the direction normal to the rotor using only the collective control mode of the active flaps. We did not consider the effects of the controller on the vibrational forces and moments in the other directions. In addition to examining the amplitude of the vibrational forces and moments in the other directions, it would be useful to generalize the fixed-order $\mathcal{H}_\infty$ control methodology to the multi-input/multi-output (MIMO) case. In the MIMO case, longitudinal and lateral cyclic controls could be used in addition to the collective, and multiple vibrational forces and/or moments could be attenuated.

3. The individual controllers we used for gain-scheduling were all of the same order, but in fact the control blending method will allow controllers of different orders to be used, and that may lead to improved performance. Furthermore, we did not quantify the effects of the bandwidth and peak sensitivity of the fixed-order controllers on the performance of the gain-scheduled controller. It would be useful to define metrics to measure the performance of the gain-scheduled controller, and know how the specification of the individual fixed-order controllers affect the performance of

the gain-scheduled controller.

4. We used plant models at four values of $\mu = \mu_j$, $j = 1, 2, 3, 4$, as shown in Table 6.1, to span the entire flight envelope. But we found that additional models at different values of μ are needed to generate good interpolated models at intermediate values of μ between μ_j's. For the plant models at each of the four values of $\mu = \mu_j$, we obtained the fixed-order controller by optimizing the performance in terms of the bandwidth and peak sensitivity. However, the performance of the interpolated controllers at intermediate values of μ were not as good as expected. Further development can consider increasing the number of plant models spanning the flight envelope, such that good interpolated models can be obtained. Then the design process can be modified to optimize the fixed-order controller for the plant model at $\mu = \mu_j$ and the nearby interpolated models. Doing so would give up some of the performance at $\mu = \mu_j$, but may improve the performance on the average during maneuvering flight.

5. The gain-scheduled controller design method could be further developed. The *ad hoc* procedure used to create the gain-scheduled control law is mostly due to the lack of knowledge on how the helicopter rotor dynamics vary with changes in flight condition, especially with respect to the advance ratio. To illustrate the problem, consider the helicopter rotor modeled by a linear parameter-varying (LPV) system with the state-space description

$$\dot{x}_1(t) = A(\theta)x_1(t) + B(\theta)u(t) \tag{7.1}$$

where $\theta = \theta(t)$. The dynamics of the rotor resulting from a transition from one flight condition to another flight condition can be obtained by applying the parameter varying transformation

$$x_1(t) = T(\theta)x_2(t) \tag{7.2}$$

to Equation (7.1). The transformed system is

$$\dot{x}_2(t) = T^{-1}(\theta)\left[A(\theta)T(\theta) - \frac{\partial T(\theta)}{\partial \theta}\dot{\theta}\right]x_2(t) + T^{-1}(\theta)B(\theta)u(t) \qquad (7.3)$$

Our LTI models contains no information on the rate of change in the parameter θ that is present in the second term in the square bracket of Equation (7.3), and so the performance of our gain-scheduled control law could certainly be improved by incorporating information on the parameter θ. Knowledge of the dynamics due to parameter variations could be used to analyze the performance of the gain-scheduled control law, and to improve the performance of the gain-scheduled controller.

6. The CAMRAD simulation could be further fine-tuned to better match the wind tunnel test results. Once better agreement with the wind tunnel data is achieved, the CAMRAD simulation could be leveraged to provide the necessary insight for understanding the nonlinear behavior of the helicopter rotor and used for actual controller design.

Bibliography

[1] M. S. Allen. Floquet Experimental Modal Analysis for System Identification of Linear Time-Periodic Systems. In *ASME 2007 International Design Engineering Technical Conference*, pages 1–11, 2007.

[2] B. D. O. Anderson and J. B. Moore. *Optimal Control: Linear Quadratic Methods*. Prentice Hall, Englewood Cliffs, New Jersey, 1989.

[3] P. Arcara, S. Bittanti, and M. Lovera. Periodic Control of Helicopter Rotors for Attenuation of Vibrations in Forward Flight. *IEEE Transactions on Control Systems Technology*, 8(6):883–894, November 2000.

[4] D. E. H. Balmford. The Control of Vibration in Helicopters. *Aeronautical Journal*, 81(2):63–67, 1977.

[5] S. Bittanti and F. A. Cuzzola. Periodic Active Control of Vibrations in Helicopters: A Gain-Scheduled Multi-Objective Approach. *Control Engineering Practice*, 10(10):1043–1057, October 2002.

[6] S. Bittanti, A. J. Laub, and J. C. Willems, editors. *The Riccati Equation*. Springer-Verlag, New York, 1991.

[7] S. Bittanti, F. Lorito, and S. Strada. Active Control of Vibrations in Helicopters: From HHC to OBC. In *Proceedings of the 18th European Rotorcraft Forum*, pages G14–1 – G14–7, Como, Italy, 1992.

[8] S. Bittanti, F. Lorito, and S. Strada. An LQ Approach to Active Control of Vibrations in Helicopters. *Transactions of the ASME*, 118(September):482–488, 1996.

[9] S. Bittanti and L. Moiraghi. Active control of vibrations in helicopters via pole assignment techniques. *IEEE Transactions on Control Systems Technology*, 2(4):343–351, 1994.

[10] R. B. Blackman and J. W. Tukey. *The Measurement of Power Spectra*. Dover Publications, New York, 1959.

[11] V. Blondel. *Simultaneous Stabilization of Linear Systems*. Springer-Verlag, 1994.

[12] H. W. Bode. *Network Analysis and Feedback Amplifier Design*. Van Nostrand, New York, 1945.

[13] D. Braun. Ground and Flight Tests of a Passive Rotor Isolation System for Helicopter Vibration Reduction. *Vertica*, 8(1):1–14, 1984.

[14] D. R. Brillinger. *Time Series: Data Analysis and Theory*. Holden-Day, San Francisco, 1981.

[15] T. F. Brooks, E. R. Booth Jr., J. R. Jolly Jr., W. T. Yeager Jr., and M. L. Wilbur. Technical Notes: Reduction of Blade-Vortex Interaction Noise Through Higher Harmonic Pitch Control. *Journal of the American Helicopter Society*, 35(1):86–91, 1990.

[16] T. J. Brown and J. L. McCloud III. Multicyclic Control of a Helicopter Rotor Considering the Influence of Vibration, Loads, and Control Motion. In *Annual Forum of the American Helicopter Society*, Washington, DC, 1980.

[17] J. C. Burgess. Active Adaptive Sound Control in a Duct: A Computer Simulation. *Journal of the Acoustical Society of America*, 70(3):715–726, 1981.

[18] G. Corliss, C. Faure, A. Griewank, L. Hascoët, and U. Naumann, editors. *Automatic Differentiation of Algorithms*. Springer-Verlag, New York, 2002.

[19] R. C. Cribbs, P. P. Friedmann, and T. Chiu. Coupled Helicopter Rotor/Flexible Fuselage Aeroelastic Model for Control of Structural Response. *AIAA Journal*, 38(10):1777–1788, 2000.

[20] G. Depailler. *Alleviation of Dynamic Stall Induced Vibrations on Helicopter Rotor Using Actively Controlled Flaps*. PhD thesis, University of Michigan, 2002.

[21] J. C. Doyle. Guaranteed Margins for LQG Regulators. *IEEE Transactions on Automatic Control*, 23(4):756–757, 1978.

[22] J. C. Doyle. Analysis of Feedback Systems with Structured Uncertainties. *IEE Proceedings D Control Theory and Applications*, 129(6):242–250, 1982.

[23] J. C. Doyle. Structured Uncertainty in Control System Design. In *Proceedings of the 24th IEEE Conference on Decision and Control*, pages 260–265, 1985.

[24] J. C. Doyle, B. A. Francis, and A. R. Tannenbaum. *Feedback Control Theory*. Macmillan, 1990.

[25] J. C. Doyle, K. Glover, P. P. Khargonekar, and B. A. Francis. State-space solutions to standard $\mathcal{H}_2$ and $\mathcal{H}_\infty$ control problems. *IEEE Transactions on Automatic Control*, 34(8):831–847, August 1989.

[26] J. C. Doyle, A. Packard, and K. Zhou. Review of LFTs, LMIs, and μ. In *Proceedings of the 30th IEEE Conference on Decision and Control*, pages 1227–1232, Brighton, England, 1991.

[27] R. W. Du Val. Design and Evaluation of a State-Feedback Vibration Controller. In *American Helicopter Society National Specialists' Meeting on Helicopter Vibration*, pages 30–37, Hartford, CT, 1981.

[28] R. W. Du Val, C. Z. Gregory Jr., and N. K. Gupta. Design and Evaluation of a State-Feedback Vibration Controller. *Journal of the American Helicopter Society*, 29(3):30–37, 1984.

[29] G. E. Dullerud and F. Paganini. *A Course in Robust Control Theory: A Convex Approach*, volume 12. Springer, New York, June 2000.

[30] L. P. Fowler. *Application of the Filtered-X LMS Algorithm for Disturbance Rejection in Time-Periodic Systems*. PhD thesis, Virginia Polytechnic Institute and State University, 1996.

[31] B. A. Francis and W. M. Wonham. The Internal Model Principle of Control Theory. *Automatica*, 12(5):457–465, September 1976.

[32] J. Freudenberg and D. Looze. Right Half Plane Poles and Zeros and Design Tradeoffs in Feedback Systems. *IEEE Transactions on Automatic Control*, 30(6):555–565, June 1985.

[33] P. P. Friedmann. Rotary-Wing Aeroelasticity: Current Status and Future Trends. *AIAA Journal*, 42(10):1953–1972, October 2004.

[34] P. P. Friedmann and T. A. Millott. Vibration Reduction in Rotorcraft Using Active Control: A Comparison of Various Approaches. *Journal of Guidance, Control, and Dynamics*, 18(4):664–673, July 1995.

[35] P. Gahinet and P. Apkarian. A Linear Matrix Inequality Approach to $\mathcal{H}_\infty$ Control. *International Journal of Robust and Nonlinear Control*, 4:421–448, January 1994.

[36] C. Ganesh and J. B. Pearson. Design of Optimal Control Systems with Stable Feedback. In *Proceedings of the American Control Conference*, pages 1969–1973, 1986.

[37] A. Garulli, A. Tesi, and A. Vicino, editors. *Robustness in Identification and Control*. Springer-Verlag, 1999.

[38] K. Glover. All Optimal Hankel-Norm Approximations of Linear Multivariable Systems and Their $\mathcal{L}_\infty$-Error Bounds. *International Journal of Control*, 39(6):1115–1193, June 1984.

[39] M. Green and D. J. N. Limebeer. *Linear Robust Control*. Prentice Hall, 1994.

[40] N. K. Gupta. Frequency-Shaped Cost Functionals: Extension of Linear-Quadratic-Gaussian Design Methods. *Journal of Guidance, Control, and Dynamics*, 3(6):529–535, November 1980.

[41] N. K. Gupta and R. W. Du Val. A New Approach for Active Control of Rotorcraft Vibration. *Journal of Guidance, Control, and Dynamics*, 5(2):143–150, March 1982.

[42] S. R. Hall, V. R. Anand, F. K. Straub, and B. H. Lau. Active Flap Control of the SMART Rotor for Vibration Reduction. In *Proceedings of the American Helicopter Society 65th Annual Forum*, Grapevine, TX, May 2009.

[43] S. R. Hall, T. Tzianetopoulou, F. K. Straub, and H. T. Ngo. Design and Testing of a Double X-Frame Piezoelectric Actuator. In *Proceedings of SPIE Smart Structures and Materials*, pages 26–37, Newport Beach, CA, March 2000.

[44] S. R. Hall and N. M. Wereley. Linear Control Issues in the Higher Harmonic Control of Helicopter Vibrations. In *Proceedings of the American Helicopter Society 45th Annual Forum*, Boston, MA, May 1989.

[45] S. R. Hall and N. M. Wereley. Performance of Higher Harmonic Control Algorithms for Helicopter Vibration Reduction. *Journal of Guidance, Control, and Dynamics*, 16(4):793–797, July 1993.

[46] N. D. Ham. Helicopter Individual-Blade-Control and Its Applications. In *Proceedings of the American Helicopter Society 39th Annual Forum*, pages 613–623, St. Louis, MO, 1983.

[47] N. D. Ham. Helicopter Individual-Blade-Control Research at MIT 1977-1985. *Vertica*, 11(1/2):109–122, 1987.

[48] C. E. Hammond. Wind Tunnel Results Showing Rotor Vibratory Loads Reduction Using Higher Harmonic Blade Pitch. *Journal of the American Helicopter Society*, 28(1):10–15, January 1983.

[49] M. N. Hamouda and G. Pierce. Helicopter Vibration Suppression Using Simple Pendulum Absorbers on the Rotor Blade. *Journal of the American Helicopter Society*, 29(3):19–29, July 1984.

[50] S. Hara, Y. Yamamoto, T. Omata, and M. Nakano. Repetitive Control System: A New Type Servo System for Periodic Exogenous Signals. *IEEE Transactions on Automatic Control*, 33(7):659–668, 1988.

[51] S. Haykin. *Adaptive Filter Theory*. Prentice Hall, Upper Saddle River, NJ, 4th edition, 2001.

[52] I. M. Horowitz. *Synthesis of Feedback Systems*. Academic Press, London, 1963.

[53] H. Ito, H. Ohmori, and A. Sano. Design of Stable Controllers Attaining Low $\mathcal{H}_\infty$ Weighted Sensitivity. *IEEE Transactions on Automatic Control*, 38(3):485–488, 1993.

[54] S. A. Jacklin, K. Nguyen, A. Blaas, and P. Richter. Full-Scale Wind Tunnel Test of a Helicopter Individual Blade Control System. In *Proceedings of the American Helicopter Society 50th Annual Forum*, pages 579–596, Washington, DC, 1994.

[55] M. Jacobus, M. Jamshidi, C. Abdallah, P. Dorato, and D. S. Bernstein. Suboptimal Strong Stabilization Using Fixed-Order Dynamic Compensation. In *Proceedings of the American Control Conference*, pages 2659–2660, San Diego, CA, 1990.

[56] W. Johnson. *Helicopter Theory*. Dover Publications, New York, 1980.

[57] W. Johnson. Self-Tuning Regulators for Multicyclic Control of Helicopter Vibration. *NASA Technical Paper 1996*, March 1982.

[58] W. Johnson. Rotorcraft Dynamics Models for a Comprehensive Analysis. In *American Helicopter Society 54th Anuual Forum*, Washington, DC, 1998.

[59] C. Kessler. Active Rotor Control for Helicopters: Individual Blade Control and Swashplateless Rotor Designs. *CEAS Aeronautical Journal*, 1(1-4):23–54, May 2011.

[60] C. Kessler. Active Rotor Control for Helicopters: Motivation and Survey on Higher Harmonic Control. *CEAS Aeronautical Journal*, 1(1-4):3–22, July 2011.

[61] C. E. Kinney, A. Villalta, and R. A. de Callafon. Active Noise Control of a Cooling Fan in a Short Duct. In *Proceedings of NCAD2008*, pages 1–11, Dearborn, MI, 2008.

[62] C. Knospe. Experiments in the Control of Unbalance Response Using Magnetic Bearings. *Mechatronics*, 5(4):385–400, June 1995.

[63] M. Kretz and M. Larché. Future of Helicopter Rotor Control. *Vertica*, 4(1):13–22, 1980.

[64] V. V. Kulkarni, L. Y. Pao, and H. Zhong. Robust Rejection of Periodic and Almost Periodic Disturbances. In *Proceedings of the 16th IFAC Triennial World Congress*, Prague, Czech Republic, 2005.

[65] S. M. Kuo and D. R. Morgan. *Active Noise Control Systems*. Wiley & Sons, 1996.

[66] H. Kwakernaak. Robust Control and $\mathcal{H}_\infty$-Optimization - Tutorial Paper. *Automatica*, 29(2):255–273, 1993.

[67] H. Kwakernaak and R. Sivan. *Linear Optimal Control Systems*. Wiley Interscience, New York, 1972.

[68] L. Liu, P. P. Friedmann, I. Kim, and D. S. Bernstein. Rotor Performance Enhancement and Vibration Reduction in Presence of Dynamic Stall Using Actively Controlled Flaps. *Journal of the American Helicopter Society*, 53(4):338–350, 2008.

[69] L. Ljung. *System Identification*. Prentice Hall, Upper Saddle River, NJ, 1999.

[70] R. G. Loewy. Helicopter Vibrations: A Technological Perspective. *Journal of the American Helicopter Society*, 29(4):4–30, October 1984.

[71] P. Lueg. Process of Silencing Sound Oscillations, 1936. US Patent 2,043,416.

[72] J. L. McCloud III. An Analytical Study of a Multicyclic Controllable Twist Rotor. In *Proceedings of the American Helicopter Society 31st Annual Forum*, pages 932–1 – 932–10, Washington, DC, 1975.

[73] F. McHugh and J. Shaw. Helicopter Vibration Reduction with Higher Harmonic Blade Pitch. *Journal of the American Helicopter Society*, 26(4):26–35, October 1978.

[74] J. A. Molusis, C. E. Hammond, and J. H. Cline. A Unified Approach to the Optimal Design of Adaptive and Gain Scheduled Controllers to Achieve Minimum Helicopter Rotor Vibration. *Journal of the American Helicopter Society*, 28(2):9–18, 1983.

[75] D. Mustafa. Relations between maximum-entropy/$\mathcal{H}_\infty$ control and combined $\mathcal{H}_\infty$/LQG control. *Systems & Control Letters*, 12(3):193–203, April 1989.

[76] H. F. Olson and E. G. May. Electronic Sound Absorber. *Journal of the Acoustical Society of America*, 25(4):1130–1136, 1953.

[77] D. Patt, D. S. Bernstein, J. Chandrasekar, P. Friedmann, and L. Liu. Higher-Harmonic-Control Algorithm for Helicopter Vibration Reduction Revisited. *Journal of Guidance, Control, and Dynamics*, 28(5):918–930, September 2005.

[78] J. T. Pearson and R. M. Goodall. Adaptive Schemes for the Active Control of Helicopter Structural Response. *IEEE Transactions on Control Systems Technology*, 2(2):61–72, June 1994.

[79] E. F. Prechtl and S. R. Hall. Design of a High Efficiency, Large Stroke, Electromechanical Actuator. *Smart Materials and Structures*, 8(1):13–30, 1999.

[80] G. Reichert. Helicopter Vibration Control: A Survey. *Vertica*, 5(1):1–20, 1981.

[81] W. Reinelt. Comparing Different Approaches to Model Error Modeling in Robust Identification. *Automatica*, 38(5):787–803, May 2002.

[82] B. Roget and I. Chopra. Individual Blade Control Methodology for a Rotor with Dissimilar Blades. *Journal of the American Helicopter Society*, 48(3):176–185, 2003.

[83] B. Roget and I. Chopra. Closed-Loop Test of a Rotor with Individually Controlled Trailing-Edge Flaps for Vibration Reduction. *Journal of the American Helicopter Society*, 55(1):012009–1 – 012009–12, 2010.

[84] M. G. Safonov. Stability Margins of Diagonally Perturbed Multivariable Feedback Systems. *IEE Proceedings D Control Theory and Applications*, 129(6):251–256, 1982.

[85] J. Shaw. *Higher Harmonic Blade Pitch Control: A System for Helicopter Vibration Reduction*. PhD thesis, Massachusetts Institute of Technology, 1980.

[86] J. Shaw and N. Albion. Active Control of the Helicopter Rotor for Vibration Reduction. *Journal of the American Helicopter Society*, 26(3):32–39, July 1981.

[87] J. Shaw, N. Albion, E. J. Hanker, and R. S. Teal. Higher Harmonic Control: Wind Tunnel Demonstration of Fully Effective Vibratory Hub Force Suppression. *Journal of the American Helicopter Society*, 34(1):14–25, 1989.

[88] S. Shin, C. E. S. Cesnik, and S. R. Hall. Closed-Loop Control Test of the NASA/Army/MIT Active Twist Rotor for Vibration Reduction. *Journal of the American Helicopter Society*, 50(2):178–194, April 2005.

[89] A. Siddiqi. Identification of the Harmonic Transfer Functions of a Helicopter Rotor. Master's thesis, Massachusetts Institute of Technology, 2001.

[90] L. A. Sievers and A. H. von Flotow. Comparison and Extensions of Control Methods for Narrow-Band Disturbance Rejection. *IEEE Transactions on Signal Processing*, 40(10):2377–2391, 1992.

[91] S. Skogestad and I. Postlethwaite. *Multivariable Feedback Control*. John Wiley & Sons, New York, 1996.

[92] M. C. Smith and K. P. Sondergeld. On the Order of Stable Compensators. *Automatica*, 22(1):127–129, January 1986.

[93] W. R. Splettstoesser, R. Kube, W. Wagner, U. Seelhorst, A. Boutier, F. Micheli, E. Mercker, and K. Pengel. Key Results From a Higher Harmonic Control Aeroacoustic Rotor Test (HART). *Journal of the American Helicopter Society*, 42(1):58–78, 1997.

[94] A. E. Staple. An Evaluation of Active Control of Structural Response as a Means of Reducing Helicopter Vibraion. In *Proceedings of the American Helicopter Society 46th Annual Forum*, pages 3–17, Washington, DC, May 1990.

[95] M. Steinbuch. Repetitive Control for Systems with Uncertain Period-Time. *Automatica*, 38(12):2103–2109, December 2002.

[96] W. Z. Stepniewski and C. N. Keys. *Rotary-Wing Aerodynamics*. Dover Publications, New York, 1984.

[97] F. K. Straub, D. K. Kennedy, A. D. Stemple, V. R. Anand, and T. S. Birchette. Development and Whirl Tower Test of the SMART Active Flap Rotor. In *Proceedings of the SPIE International Symposium on Smart Structures and Materials*, San Diego, CA, March 2004.

[98] M. O. Tokhi and R. R. Leitch. *Active Noise Control*. Oxford University Press, Oxford, 1992.

[99] M. Vidyasagar. *Control System Synthesis*. MIT Press, 1985.

[100] Y. W. Wang and D. S. Bernstein. $\mathcal{H}_2$-Suboptimal Stable Stabilization. *Automatica*, 30(11):1797–1800, November 1994.

[101] Y. W. Wang, W. M. Haddad, and D. S. Bernstein. Stable Stabilization with $\mathcal{H}_2$ and $\mathcal{H}_\infty$ Performance Constraints. *Journal of Mathematical Systems, Estimation, and Control*, 6(2):181–194, 1996.

[102] N. M. Wereley and S. R. Hall. Frequency Response of Linear Time Periodic Systems. In *Proceedings of the 29th IEEE Conference on Decision and Control*, pages 3650–3655, Honolulu, HI, December 1990.

[103] B. Widrow, D. Shur, and S. Shaffer. On Adaptive Inverse Control. In *Proceedings of the 15th Asilomar Conference*, pages 185–189, 1981.

[104] J. B. Wilkerson, K. R. Reader, and D. W. Linck. The Application of Circulation Control Aerodynamics to a Helicopter Rotor Model. *Journal of the American Helicopter Society*, 19(2):2–16, 1974.

[105] E. R. Wood, R. W. Powers, J. H. Cline, and C. E. Hammond. On Developing and Flight Testing a Higher Harmonic Control System. *Journal of the American Helicopter Society*, 30(1):3–20, 1985.

[106] D. C. Youla, J. J. Bongiorno Jr., and H. A. Jabr. Modern Wiener-Hopf Design of Optimal Controllers Part I: The Single-Input-Output Case. *IEEE Transactions on Automatic Control*, AC-21(1):3–13, 1976.

[107] D. C. Youla, J. J. Bongiorno Jr., and C. N. Lu. Single-Loop Feedback-Stabilization of Linear Multivariable Dynamical Plants. *Automatica*, 10(2):159–173, March 1974.

[108] D. C. Youla, H. A. Jabr, and J. J. Bongiorno Jr. Modern Wiener-Hopf Design of Optimal Controllers - Part II: The Multivariable Case. *IEEE Transactions on Automatic Control*, AC-21(3):319–338, 1976.

[109] K. C. Zangi. *Optimal Feedback Control Formulation of the Active Noise Cancellation Problem: Pointwise and Distributed.* PhD thesis, Massachusetts Institute of Technology, 1994.

[110] M. Zeren and H. Özbay. On the Synthesis of Stable $\mathcal{H}_\infty$ Controllers. 44(2):431–435, 1999.

[111] M. Zeren and H. Özbay. On the Strong Stabilization and Stable $\mathcal{H}_\infty$ Controller Design Problems for MIMO Systems. *Automatica*, 36:1675–1684, 2000.

[112] K. Zhou and J. C. Doyle. *Essentials of Robust Control.* Prentice Hall, Upper Saddle River, NJ, 1998.